

# Nanoscale Friction Measurements on Manganite Thin Films: Which Material Properties are Important?

---

Dissertation

for the award of the degree

**"Doctor rerum naturalium"**

of the Georg-August-Universität Göttingen

within the doctoral program

Physics

of the Georg-August University School of Science (GAUSS)

submitted by

**Niklas Alfred Weber**

from Bremen, Germany

Göttingen, 2022

### **Thesis Committee:**

Prof. Cynthia A. Volkert, PhD  
Institut für Materialphysik  
Georg-August-Universität Göttingen

Prof. Dr. Martin Wenderoth  
IV. Physikalisches Institut  
Georg-August-Universität Göttingen

Dr. Friedrich Güthoff  
Institut für Physikalische Chemie  
Georg-August-Universität Göttingen

### **Members of the Examination Board:**

Prof. Cynthia A. Volkert, PhD  
Institut für Materialphysik  
Georg-August-Universität Göttingen

Prof. Dr. Matthias Krüger  
Institut für Theoretische Physik  
Georg-August-Universität Göttingen

### **Further members of the Examination Board:**

Prof. Dr. Hans Hofsäss, II. Physikalisches Institut, Georg-August-Universität Göttingen  
Prof. Dr. Christian Jooß, Institut für Materialphysik, Georg-August-Universität Göttingen  
Prof. Dr. Vasily Moshnyaga, I. Physikalisches Institut, Georg-August-Universität Göttingen  
Prof. Dr. Thomas Weitz, I. Physikalisches Institut, Georg-August-Universität Göttingen

**Date of the oral examination: 20.12.2022**





---

## List of Publications

Parts of the results and discussion section, presented in this thesis, have been included in peer-reviewed journal articles or have been recently submitted. The respective manuscripts are the following:

- [1] H. Schmidt, J. O. Krisponeit, N. Weber, K. Samwer, and C. A. Volkert, *Switching friction at a manganite surface using electric fields*, [Physical Review Materials](#) **4**, 113610 (2020).
- [2] N. A. Weber, H. Schmidt, T. Sievert, C. Jooss, F. Güthoff, V. Moshneaga, K. Samwer, M. Krüger, and C. A. Volkert, *Polaronic Contributions to Friction in a Manganite Thin Film*, [Advanced Science](#) 2003524 (2020), [10.1002/adv.202003524](#).
- [3] M. Lee, N. Weber, C. A. Volkert, and M. Krüger, *Friction on layered media: How deep do phonons reach?*, (2022) [arXiv:2205.01151](#) – submitted to a peer-reviewed journal in May 2022.
- [4] N. A. Weber, M. Lee, F. Schönewald, L. Schüler, V. Moshnyaga, M. Krüger, and C. A. Volkert, *Nanoscale friction controlled by top layer thickness in  $[\text{LaMnO}_3]_m/[\text{SrMnO}_3]_n$  superlattices*, (2022) [arXiv:2210.09677](#) – submitted to a peer-reviewed journal in October 2022.



---

## Abbreviations

<u>Abbreviation</u>	<u>Defenition</u>	<u>Page</u>
<b>AFM</b>	atomic force microscope . . . . .	12
<b>C-AFM</b>	conductive AFM . . . . .	35
<b>DMT</b>	Derjaguin, Muller and Toporo . . . . .	8
<b>FM</b>	ferromagnetic . . . . .	38
<b>FD-curve</b>	force-distance-curve . . . . .	31
<b>FK</b>	Frenken-Kontorova . . . . .	15
<b>FKT</b>	Frenken-Kontorova-Tomlinson . . . . .	15
<b>JT-effect</b>	Jahn-Teller-effect . . . . .	22
<b>JT-polaron</b>	Jahn-Teller-polaron . . . . .	25
<b>JKR</b>	Johnson, Kendall and Roberts . . . . .	7
<b>LFM</b>	lateral force microscopy . . . . .	29
<b>La<sub>(1-x)</sub>Sr<sub>x</sub>MnO<sub>3</sub></b>	lanthanum strontium manganite . . . . .	21
<b>LaMnO<sub>3</sub></b>	lanthanum manganite . . . . .	25
<b>MAD</b>	metalorganic aerosol deposition . . . . .	27
<b>PM</b>	paramagnetic . . . . .	38
<b>PSD</b>	position sensitive detector . . . . .	30
<b>PT</b>	Prandtl-Tomlinson . . . . .	13
<b>SEM</b>	scanning electron microscope . . . . .	32
<b>SPM</b>	scanning probe microscopy . . . . .	29
<b>STM</b>	scanning tunneling microscope . . . . .	29
<b>SrMnO<sub>3</sub></b>	strontium manganite . . . . .	26
<b>SI</b>	supporting information . . . . .	37
<b>TTR</b>	thermal transient reflectometry . . . . .	28
<b>UHV</b>	ultra-high vacuum . . . . .	12
<b>XRD</b>	$\theta$ -2 $\theta$ x-ray diffraction . . . . .	57

---

<b>XPS</b>	x-ray photoelectron spectroscopy . . . . .	60
<b>XRR</b>	x-ray reflectivity . . . . .	57

# Contents

List of Publications . . . . .	I
Abbreviations . . . . .	III
<b>1. Introduction</b>	<b>1</b>
<b>2. Tribology</b>	<b>5</b>
2.1. Friction on the Microscopic Scales . . . . .	5
2.1.1. Single Asperity Contacts . . . . .	6
2.1.2. Stress Fields . . . . .	9
2.1.3. Interaction Forces . . . . .	11
2.2. Friction on the Nanoscale . . . . .	13
2.2.1. Prandtl-Tomlinson Model . . . . .	13
2.2.2. Velocity Dependence and Thermal Effects . . . . .	16
2.3. Dissipation Mechanisms . . . . .	17
2.3.1. Phononic contributions . . . . .	17
2.3.2. Electronic contributions . . . . .	19
<b>3. Manganites</b>	<b>21</b>
3.1. Crystal Structure . . . . .	21
3.2. Electric and Magnetic Properties . . . . .	22
3.2.1. Jahn-Teller-Effect . . . . .	22
3.2.2. Double-Exchange . . . . .	23
3.2.3. Super-Exchange . . . . .	24
3.2.4. Polarons . . . . .	25
3.3. Phase Diagram of Lanthanum Strontium Manganite . . . . .	26
3.4. Superlattices . . . . .	27

<b>4. Atomic Force Microscopy</b>	<b>29</b>
4.1. Basic Principle . . . . .	29
4.1.1. Force-Distance-Curves . . . . .	31
4.1.2. Force Calibration . . . . .	32
4.2. Lateral Force Microscopy . . . . .	34
4.3. Conductive-AFM . . . . .	35
<b>5. Friction Measurements</b>	<b>37</b>
5.1. Polaronic Contributions to Friction in a Manganite Thin Film . . . . .	37
5.1.1. Abstract . . . . .	38
5.1.2. Introduction . . . . .	38
5.1.3. Results and Discussion . . . . .	43
5.1.4. Conclusion . . . . .	56
5.1.5. Experimental Section . . . . .	56
5.1.6. Acknowledgements . . . . .	59
5.2. Nanoscale Friction Controlled by Top Layer Thickness in Superlattices . . . . .	60
5.2.1. Abstract . . . . .	61
5.2.2. Introduction . . . . .	61
5.2.3. Materials and Methods . . . . .	62
5.2.4. Results and Discussion . . . . .	65
5.2.5. Conclusions . . . . .	73
5.2.6. Acknowledgements . . . . .	74
<b>6. Conclusion</b>	<b>75</b>
<b>A. Appendix</b>	<b>83</b>
A.1. SI - Sample Characterization . . . . .	83
A.1.1. Ellipsometry Measurements . . . . .	83
A.1.2. XRD Measurements . . . . .	84
A.1.3. XRR Measurements . . . . .	85
A.1.4. XPS Measurements . . . . .	86
A.1.5. Thermal Resistivity Values . . . . .	88
A.1.6. Magnetic Measurements . . . . .	88
A.2. SI - Topography and Friction Maps . . . . .	91
A.3. SI - Friction versus Normal Force Measurements . . . . .	92
A.3.1. Friction Force as a Function of Applied Normal Force . . . . .	92

A.3.2. Correlation between $F_{F0}/\mu$ and Adhesion . . . . .	95
A.3.3. Friction Force as a Function of $(F_N+F_{F0})/\mu$ . . . . .	96
A.3.4. Master Equation Top Layer Thickness Dependency . . . . .	98
A.4. SI - Elastically Strained Volume . . . . .	99
<b>Bibliography</b>	<b>103</b>
<b>Acknowledgements</b>	<b>117</b>



# 1. Introduction

During the relative motion of two bodies in contact, parts of the required mechanical energy is converted into heat. This energy dissipative process is commonly known as friction, and getting to the bottom of frictional losses has bothered mankind for thousands of years.

The first evidence of the utilization of this energy-dissipative process can be found in the use of fire drills, which were used in the Neolithic period about eight thousand years ago.<sup>[5]</sup> The first documented attempt to control friction dates back to Ancient Egypt; a mural from the tomb of Tehuti-Hetep at El Bersheh, created around 1800 B.C.,<sup>[6,7]</sup> depicts 172 workers pulling a stone figure mounted on a sledge (see fig. 1.1). In the center of the mural, one of the workers is depicted pouring a liquid in front of the sledge runners. In an experimental study by Fall et al.,<sup>[8]</sup> it was later shown that under the right conditions, a mixture of sand and water can reduce the force required to set the sledge in motion by 70% and the force required to keep it moving by up to 40%, compared to when it is moved on just sand.

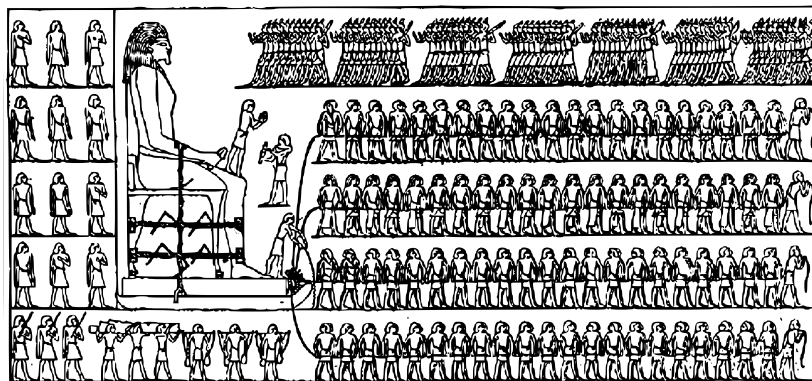


**Figure 1.1:** Mural from the tomb of Tehuti-Hetep at El Bersheh, dated around 1800 B.C. The mural depicts 172 workers pulling a stone figure. One of the workers, in the center of the illustration, is pouring a liquid in front of the sledge, presumably to minimize friction.<sup>[6,7]</sup>

The first attempts to scientifically describe the friction between two macroscopic objects dates to the empirical studies by the French physicists Guillaume Amontons (1699) and Charles-Augustin de Coulomb (1773). Based on their studies, they established the well-known law of

friction between two macroscopic objects, better known as Amontons' law:<sup>[9]</sup>

$$F_F = \mu \cdot F_N.$$

The Amontons' law relates the friction force  $F_F$  required to move an object to the applied normal force  $F_N$ . The proportionality constant between the two quantities is known as the friction coefficient  $\mu$ .

Considering the long history of tribology studies, it is all the more surprising that even today, almost 23% ( $119 \times 10^{18}$  J) of the world's total energy consumption originates from tribological contacts.<sup>[10]</sup> The question of how to control energy losses specifically, especially in the case of non-lubricated contacts, has thus not lost its relevance despite its long history.

This thesis aims to contribute to the unraveling of the mechanisms underlying dry nanoscale friction, and is part of the second funding period of the [Collaborative Research Center SFB 1073 Project A01](#). The goal of Project A01 within the CRC is to investigate how nanoscale friction can be controlled by the degrees of freedom of the surrounding material, using simulations, as well as theoretical and experimental approaches, the latter of which will be the focus of this thesis.

Results from the first funding period of the CRC 1073<sup>[1,11-13]</sup> and from other research groups<sup>[14-24]</sup> indicate that dry friction can be attributed to either the phononic and electronic degrees of freedom of the surrounding material, the former of which seem to be especially relevant in the case of manganite thin films. These contributions are therefore examined more thoroughly in the context of this thesis by means of atomic force microscope (AFM)-based experiments. In the friction experiments presented, material properties of the manganite thin films studied are actively altered. This is achieved by the means of phase transitions, resistive switching, or the introduction of interfaces (superlattices). The fundamental idea is that if a change in the friction occurs in connection with a change in the material properties, conclusions can be drawn concerning the underlying mechanisms.

In order to investigate the origins of nanoscale friction, temperature-dependent friction measurements on a  $\text{La}_{0.8}\text{Sr}_{0.2}\text{MnO}_3$  thin film were carried out in the first part of the thesis. In connection with the second order phase transformation, a noticeable change in friction force was observed. These investigations not only validated the findings from previous temperature-dependent friction measurements on a  $\text{La}_{0.6}\text{Sr}_{0.4}\text{MnO}_3$  thin film<sup>[11]</sup>, but also extended the understanding of the dissipation mechanisms governing friction. It was concluded that the electronic and electrostatic contributions are orders of magnitude too small to be solely re-

sponsible for the large change in friction. Instead, phononic contributions that change with the phase transformation were identified as the dominant dissipation channel (see section 5.1).

Based on the findings from the temperature-dependent friction experiments, friction was measured on seven superlattice systems ( $[\text{LaMnO}_3]_m/[\text{SrMnO}_3]_n$ ), the results of which are addressed in the second part of the thesis. The goal of these measurements was to identify the dominant phonon modes, a question that remained unanswered in previous experiments. These studies furthermore revealed, in an unprecedented clarity, that not only surface dynamics, but also intrinsic material properties contribute to sliding friction, and allowed to gauge to what depth material properties contribute (see section 5.2).



## 2. Tribology

In the following chapter, a literature overview is provided which forms the theoretical basis for the friction measurements and the evaluation presented in this work. Furthermore, it contains the necessary literature background to motivate and classify the experimental studies conducted in this thesis. For this purpose, the phenomenon of friction is discussed on different length scales and different contributions to this energy dissipative process are described.

The first attempts to scientifically describe friction between two macroscopic objects dates back to Guillaume Amontons (1699) and Charles-Augustin de Coulomb (1773). Based on empirical studies, they established the known law of friction between two macroscopic objects:<sup>[9]</sup>

$$F_F = \mu \cdot F_N \quad (2.1)$$

where  $F_N$  is the normal force and  $\mu$  is the coefficient of friction. Coulomb initially believed that cohesion was the origin of friction, but later abandoned the idea because under this consideration friction would be proportional to the contact area, which contradicted his measurements. He imagined that friction originates from an interlocking of the surfaces that increased with load. However, Coulomb could not yet prove this idea, as the technology to create topographic images of surfaces on a small scale were not yet accessible.<sup>[9]</sup>

### 2.1. Friction on the Microscopic Scales

200 years after Amontons and Coulomb postulated the first law's to describe friction between macroscopic objects,<sup>[9]</sup> the apparent contradiction that friction is not related to the surface area in contact were resolved in a treatise by Bowden and Tabor.<sup>[25]</sup> In their work, they postulated the first model for the description of friction on the microscale, which is in accordance with Amontons and Coulomb's macroscopic laws. They discovered that macroscopically smooth surfaces (see fig. 2.1a) exhibit numerous bumps, so-called asperities (see fig. 2.1b), and therefore the real contact area between two bodies deviates from the apparent contact area on the macro scale. In their model, the real contact area  $A_R = \sum A_i$  is the sum of

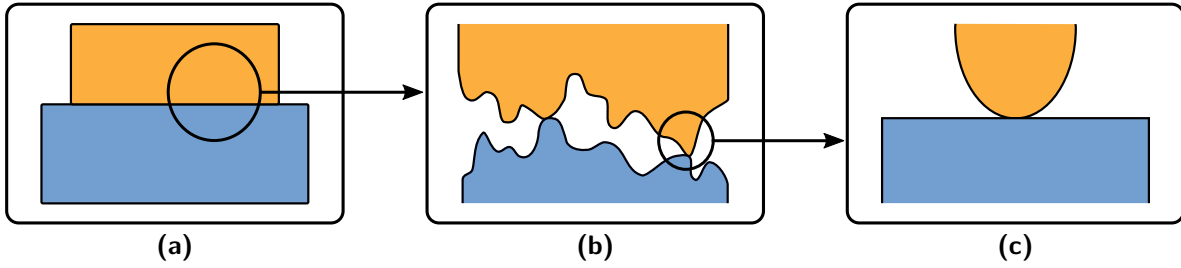


**Figure 2.1:** Contact areas between two surfaces in different magnifications: (a) macroscopic contact, (b) microscopic contact, and (c) single asperity contact.

all asperities in contact (see fig. 2.1c), which can be a few orders of magnitude smaller than the apparent contact area. Based on their observations Bowden and Tabor concluded that the lateral force is proportional to the real contact area  $A_R$  and to the shear strength  $\tau$ , an average lateral force per unit area required to shear the asperities in contact:<sup>[26,27]</sup>

$$F_F = A_R \cdot \tau. \quad (2.2)$$

When applying a sufficient normal load  $F_N$  the asperities in the contact area are compressed until a certain yield pressure  $p^*$  is reached. Under this assumption, the contact area  $A_R = F_N/p^*$  and thus eq. 2.2 would be equal to Amontons/Coulombs phenomenological laws of friction, with  $\mu = \tau/p^*$ .

However, the model cannot account for the observed friction in cases where the plastic deformation of asperities (at small normal forces) can be neglected, which has been observed experimentally in the 1970s by Israelachvili and Tabor.<sup>[28,29]</sup>

Therefore, the questions remain: What is the physical origin of energy transfer in the friction process when there is no plastic material deformation? What is the contact area  $A_i$  of an elastic contact? To address these questions, different contact models for elastic contacts and further models describing friction at a single asperity contact will be discussed subsequently.

### 2.1.1. Single Asperity Contacts

By assuming that the interaction between an asperity and the underlying surface is mainly elastic<sup>[26,27]</sup> and the effective contact area  $A_i$  can be estimated in simplified terms by the Hertzian contact model. In the model, the effective contact area  $A_{Hertz}$  and indentation depth  $d$  of two spheres with radii  $r_1$  and  $r_2$ , are described under the assumption that the radius of one of the two spheres is infinitely large  $r_2 \rightarrow \infty$ , while the other sphere has a finite radius  $r_1 \rightarrow R$  (see fig. 2.2). Applying a normal force  $F_N$  on to the smaller sphere leads to a

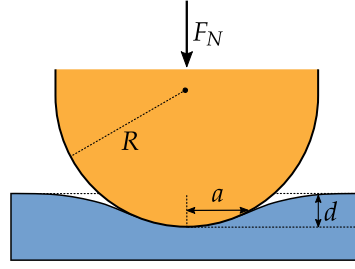


**Figure 2.2:** Contact of an elastic sphere with an elastic plane, under an applied load  $F_N$ . Due to the applied load, the sphere indents the surface up to a depth of  $d$ . The contact radius  $a$  can be derived from the indentation depth and the radius of the sphere  $R$ .

deformation of the infinite sphere. The resulting deformation depth  $d$  is related to the normal force  $F_N$  by:<sup>[30]</sup>

$$d = \frac{a^2}{R} = \left( \frac{9F_N^2}{16E^{*2}R} \right)^{1/3}, \quad (2.3)$$

from which the contact area

$$A_{Hertz} = \pi \left( \frac{3RF_N}{4E^*} \right)^{2/3} \quad (2.4)$$

can be derived. Here  $a$  corresponds to the contact radius, and  $E^*$  represents the effective Young's modulus.<sup>[30]</sup> Inserting the result into eq. 2.2 yields:

$$F_F = \tau \pi \left( \frac{3RF_N}{4E^*} \right)^{2/3}. \quad (2.5)$$

Despite the experimental agreement, the Hertzian contact is a rather simple description of the true contact area, since interaction forces are neglected. The model thus cannot account for observations of a finite friction force  $F_{F0}$ , even if the normal force is set to  $F_N = 0$  N. A model that accounts for these non-vanishing friction forces, by also considering short-range interaction forces, was postulated by Johnson, Kendall and Roberts (JKR).<sup>[31]</sup> In their model, forces within the contact area are described by a surface energy  $\gamma^*$ , which is the sum of the surface energies of the materials in contact and the interface  $\gamma^* = \gamma_1 + \gamma_2 - \gamma_{12}$ . This additional force is often referred to as an adhesion force (see section 2.1.3), that accounts for the observation that two materials in contact cannot be removed continuously. Instead, the contact breaks abruptly due to a mechanical instability at a critical pull-off force:<sup>[24,32]</sup>

$$F_0 = \frac{3}{2} \pi R \gamma^*. \quad (2.6)$$

This increases the contact area, compared to the Hertzian model:<sup>[31]</sup>

$$A_{JKR} = \pi \left[ \frac{3R}{4E^*} (F_N + 2F_0 + \sqrt{4F_0F_N + (2F_0)^2}) \right]^{2/3}. \quad (2.7)$$

The equation implies that a contact surface remains even for negative normal forces, until the pull-off force  $F_0$  is reached.

The JKR-model can be used particularly well for high adhesion forces and soft materials.<sup>[24]</sup> However, the model is not applicable for asperities with small radii since attractive forces outside the contact surface are neglected, resulting in an infinitely high stress at the edge of the contact. This shortcoming was resolved by Derjaguin, Muller and Toporo (DMT)<sup>[33]</sup> by including long-range adhesion forces outside the contact. In this model, the contact area is expressed as:<sup>[24]</sup>

$$A_{DMT} = \pi \left[ \frac{3R}{4E^*} (F_N + \frac{4}{3}F_0) \right]^{2/3}. \quad (2.8)$$

In contrast to the JKR-model, the DMT-model is more suitable for hard materials on whose surface only weak adhesion forces act. Accordingly, both models represent two extreme cases between which real systems can be classified.<sup>[24]</sup> A comparison of the three models presented, and for an intermediate case, characterized by Maugis-Dugdale and generalized by Carpick et al. and Schwarz, is depicted in fig. 2.3.<sup>[34–36]</sup>

In macroscopic systems, multiple asperities are interacting simultaneously and contributing to the overall friction. Greenwood et al.<sup>[37]</sup> showed that for a statistical distribution of asperity heights and radii, the sum of their contact areas follows a linear dependence with normal force,<sup>[37–39]</sup> which leads to a correspondence of the models presented here with the macroscopic empirical description of friction proposed by Amontons and Coulomb.

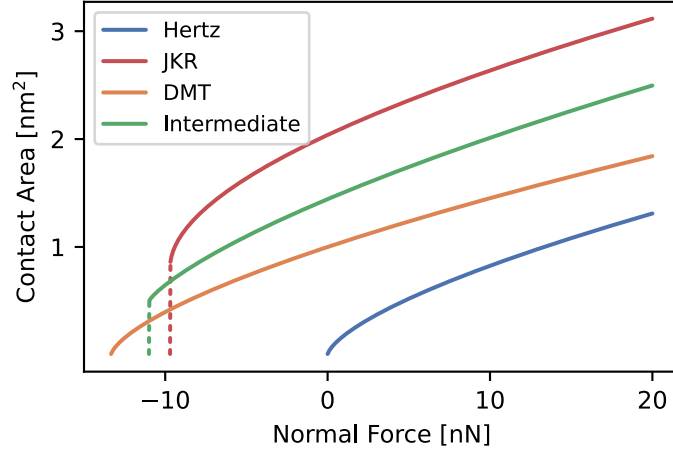


**Figure 2.3:** Contact area of an ideal spherical asperity as a function of applied load for JKR-, DMT-, intermediate and Hertz contact model.<sup>[30,31,33,36]</sup> To calculate the contact areas shown here, experimentally reasonable values were selected:  $R = 10$  nm,  $E^* = 100$  GPa and  $F_0 = 10$  nN.

### 2.1.2. Stress Fields

In the previous section, it is illustrated how a spherical single asperity elastically deforms a plane surface according to the Herzian contact model, when a normal force  $F_N$  is applied. The resulting indentation has a depth (see eq. 2.3)<sup>[30]</sup>

$$d = \frac{a^2}{R} = \left( \frac{9F_N^2}{16E^*{}^2R} \right)^{1/3}.$$

Due to the indentation of the surface, a heterogeneous stress field is generated in the underlying material. The exact shape and dimensions depend on the shape of the indenter, the applied normal force, and the elastic properties of the materials. These stress fields are known to slowly decay over a length scales proportional to the interaction area of the indenter and where it can cause non-negligible perturbations of the material.<sup>[40]</sup>

If it is assumed that, as postulated by Bowden and Tabor,<sup>[25]</sup> an asperity exhibits a spherical apex the generated stress field can be expressed as:<sup>[40]</sup>

$$\sigma_{zr} = -3p_m(1 + \nu) \frac{z}{\sqrt{u}} \left[ \frac{\sqrt{u}}{a} \arctan \left( \frac{a}{\sqrt{u}} \right) - 1 \right] \quad (2.9)$$

where  $u = 1/2 \cdot [(r^2 + z^2 - a^2) + \sqrt{(r^2 + z^2 - a^2)^2 + 4a^2z^2}]$ ,  $p_m = F_N/\pi a^2$  the contact pressure and  $\nu$  the Poisson's ratio (see fig. 2.4).<sup>1</sup>

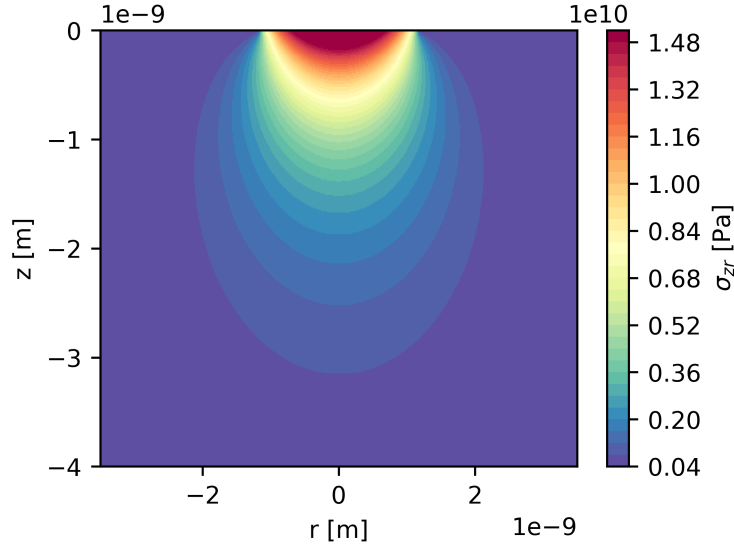


**Figure 2.4:** Stress field caused by the indentation of a spherical tip into the underlying material, according to eq. 2.9. For the illustration, experimentally reasonable values of  $F_N = 20$  nN,  $R = 10$  nm,  $E^* = 95$  GPa and  $\nu = 0.35$  were used.

If the indenter is now dragged over the sample surface with a constant velocity  $v_s$ , the stress field below the indenter moves correspondingly, resulting in a constant loading and unloading of the underlying material. Under adiabatic conditions, the changing stress  $\Delta\sigma$  leads to a local change in temperature proportional to<sup>[41]</sup>

$$\Delta T = -\frac{\alpha}{\rho c_p} T_0 \Delta\sigma_{zr}, \quad (2.10)$$

where  $T_0$  is the ambient temperature,  $c_p$  the specific heat at constant pressure,  $\rho$  the density, and  $\alpha$  the linear thermal expansion coefficient. Due to the local change in temperature, a heat flow occurs in the material, that can be as large as

$$Q = -\varepsilon_{th} V \Delta\sigma. \quad (2.11)$$

In the equation  $V$  corresponds to the size of the stressed volume, and  $\varepsilon_{th} = T_0\alpha$  the thermal strain.<sup>[41]</sup> Under the assumption that the frequency  $f$ , which is proportional to the scan speed,

<sup>1</sup>Various contact geometries are discussed in the textbook *Introduction to Contact Mechanics* by A. Fischer-Cripps.<sup>[40]</sup>

of loading and unloading under the tip is known, this heat flow can be converted into dissipated energy  $P$ :

$$P = 2f\varepsilon_{th}V\Delta\sigma. \quad (2.12)$$

A detailed discussion of the magnitude of this thermodynamic contribution to energy dissipation, and thus sliding friction can be found in section 5.2.4 (page 70ff.).

### 2.1.3. Interaction Forces

When two solids are brought close together, they begin to interact. These interactions can be attractive or repulsive, and their strength and relative contribution depends on the distance between the surfaces, their surface morphology and chemistry.

If the two objects are relatively far apart,<sup>[42]</sup> the interaction is dominated mainly by long-range electrostatic forces, which in the simplest case can be estimated using Coulomb's law

$$F_C = \frac{Q_1Q_2}{4\pi\varepsilon_0d^2} \quad (2.13)$$

and are proportional to the charge  $Q_1$  and  $Q_2$ , and inverse proportional to dielectric properties and the distance squared  $d^2$ . If a potential  $U$  is applied between two surfaces, the surfaces form a capacitor of complex geometry. Hudlet et al.<sup>[43]</sup> derived an analytical expression to describe distance-dependent capacitive interactions for an AFM tip and a flat surface, which is used in the following as a model for a single-asperity contact:

$$F_{cap}(d) = \pi\varepsilon_0(U - U_0)^2f(d), \quad (2.14)$$

where  $U_0$  accounts for residual surface potentials and  $f(d) \propto \partial C/\partial d$  for the distance-dependent change of the capacitance, whose characteristics are strongly influenced by the tip geometry.<sup>[42,43]</sup>

If the distance between the two surfaces is reduced continuously and significantly below  $d = 30$  nm,<sup>[44,45]</sup> the influence of van der Waals forces increases continuously. These forces originate from the fluctuations of dipole moments, as well as the polarization of the interacting atoms. For a spherical tip at a distance  $d$  from a plane surface, the van der Waals interaction leads to an attractive force of

$$F_{vdW}(d) = \mathcal{H}\frac{R}{6d^2}, \quad (2.15)$$

where  $\mathcal{H}$  is the Hamaker constant<sup>[46]</sup>, whose magnitude depends on the polarizability of the atoms and the density of the interacting solids.<sup>[47]</sup>

For even smaller distances  $d < 4$  nm,<sup>[44]</sup> the surfaces are considered to be in contact. In this regime, the attractive force increases further, by the formation of menisci, especially in the presence of condensates.<sup>[44]</sup> A spherical tip in contact with a smooth surface, and with a concave meniscus formed at the interface, experiences an attractive force of

$$F_m = 2\pi R\gamma(\cos(\theta_1) + \cos(\theta_2)) \quad (2.16)$$

which is equal to the additional attractive forces described in the previous section (see fig. 2.5). The surface tension  $\gamma$  is the result of the incomplete bonding of the surface atoms, and ranges from  $0.1 \text{ J m}^{-2}$  to  $3 \text{ J m}^{-2}$  for most solids.<sup>[48,49]</sup>

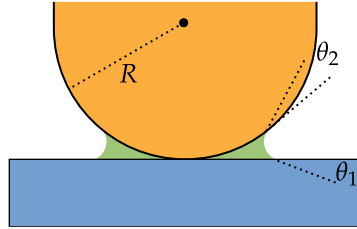


**Figure 2.5:** Capillary forces can lead to the formation of menisci between a single asperity contact and a smooth surface, thereby increasing the adhesive forces between the two objects. The resulting adhesive forces are particularly facilitated by liquid condensate at the interface.

The relative contribution of the interaction forces depends on numerous factors including surface charges and chemistry, humidity, hydrophobicity, separation, and roughness. An overview of how different environmental conditions affect the interactions between an atomic force microscope (AFM)-tip and a smooth sample, can be found in the publication by Stifter et al.<sup>[50]</sup> According to Stifter et al. the interaction under ultra-high vacuum (UHV) conditions can be sufficiently well modeled by a Lennard-Jones potential:

$$V(d) = \frac{c}{12} \left( \frac{\mathcal{H}}{d} + \frac{B}{210 \cdot d^7} \right), \quad (2.17)$$

where  $c$  is the width of the parabolic tip, and  $\mathcal{H}$ ,  $B$  represent two parameters accounting for the magnitude of the interaction potential.

Gauging these interaction forces can be achieved experimentally by measuring so-called force distance curves (see section 4.1.1).

## 2.2. Friction on the Nanoscale

While various contact models presented (see section 2.1.1) bridge the gap between the mechanics of individual asperities and that of macroscopic contacts, they do not disentangle the fundamental parameters determining the strength of the energy dissipation due to friction.<sup>[24]</sup> In order to approach this question, an atomistic description of friction, the so-called Prandtl-Tomlinson (PT)-model, is presented in the following. This model forms the basis for explaining and understanding the dependence of friction on scanning velocity and temperature.

### 2.2.1. Prandtl-Tomlinson Model

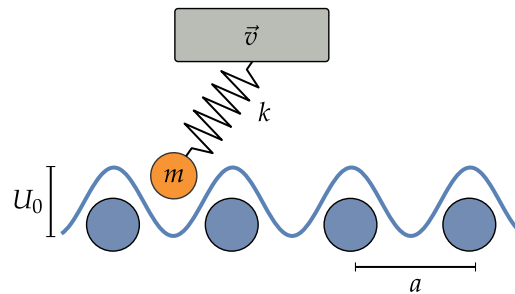


**Figure 2.6:** Schematic representation of the Prandtl-Tomlinson-model. A point mass  $m$  attached to a rigid support via a spring  $k$  is dragged along a sinusoidal potential with a velocity  $\vec{v}$ .

In the 1D PT-model<sup>[51,52]</sup> the frictional interaction between a single asperity contact and a crystalline substrate is described by defining the asperity as a point mass  $m$  connected via a harmonic spring  $k$  to a rigid support (see fig. 2.6). Moving the support at a constant velocity  $v$  over a periodic surface potential  $U_S$ , increases the restoring force. If the restoring force is large enough, the mass can overcome the potential barrier, and reach the next potential minimum.

If inertia, and thermal effects are neglected, the total energy  $U_{tot}$  of the system, at a given time  $t$ , can be expressed by:<sup>[53,54]</sup>

$$U_{tot} = U_S + U_{el} \\ \stackrel{1D}{=} U_0 \cos\left(\frac{2\pi x}{a}\right) + \frac{1}{2}k(x - vt)^2 \quad (2.18)$$

where  $a$  is the spacing of the lattice and  $U_0$  the amplitude of the surface potential. The leading term of eq. 2.18 accounts for the corrugation of the surface potential, while the second term describes the elastic potential resulting from the interactions between mass and support. In

Figure 2.7 the energy profile at two different times  $t = 0$  and  $t = t^*$  is depicted. At  $t = 0$  the mass is pinned at a minimum of the potential. With time, the minimum becomes less pronounced until the position of the mass becomes unstable at  $t = t^*$  and it suddenly slips into the next minimum.

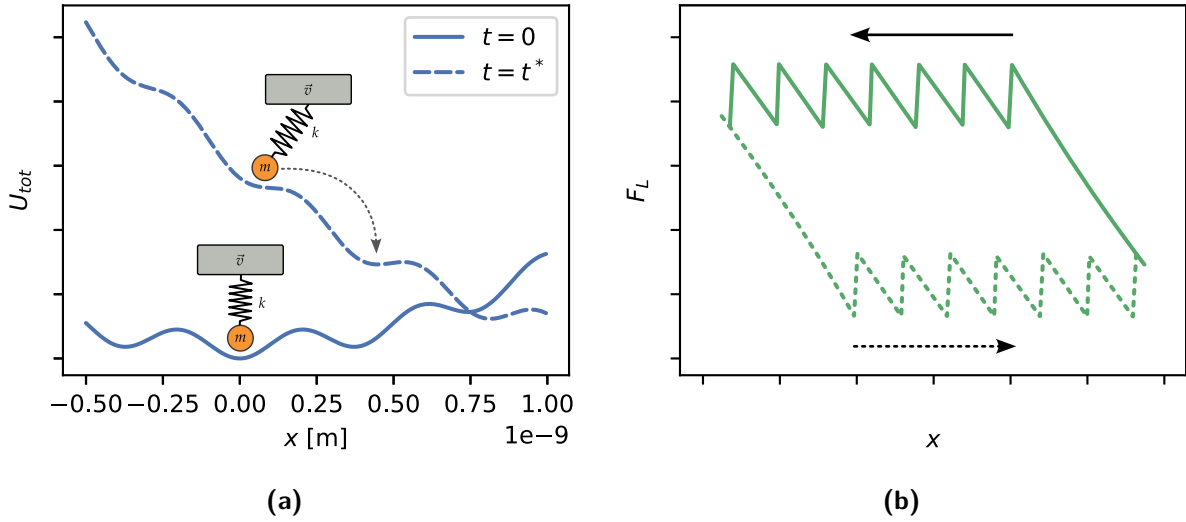


**Figure 2.7:** (a) Energy profile  $U_{tot}$  at a time  $t = 0$  and at the "critical" time  $t = t^*$ . (b) Friction loop by scanning the potential back and forth. The spring constant  $k$  is given by the slope of the sticking part.

The dynamics of the mass can be described by a Langevin equation:<sup>[55]</sup>

$$m\ddot{x} + \eta m\dot{x} = \frac{\partial U_{tot}}{\partial x} + F_{th}, \quad (2.19)$$

where  $\eta$  is a viscous friction or damping coefficient and  $F_{th}$  a thermal activation force (see section 2.2.2). This equation can be solved for  $x$  resulting in a lateral/friction force of:<sup>[53,54]</sup>

$$F_L = k(x - vt) = -\frac{2\pi U_0}{a} \sin\left(\frac{2\pi x}{a}\right). \quad (2.20)$$

Depending on the ratio between the magnitude of the surface potential  $U_0$  and the spring constant  $k$  the PT-model predicts two different modes of tip motion that can be differentiated by the dimensionless parameter  $\gamma$ :<sup>[53,54]</sup>

$$\gamma = \frac{4\pi^2 U_0}{ka^2}. \quad (2.21)$$

If  $\gamma > 1$ , the overall potential exhibits multiple minima, resulting in a non-continuous stick-

slip motion; the point mass jumps between successive minima of  $U_{tot}$ . This non-continuous motion of a sliding contact has been observed both in experiment<sup>[54,56–59]</sup> and in theoretical studies,<sup>[60,61]</sup> on different length scales.<sup>[56,62]</sup> Examples of this phenomenon from everyday life are the squeaking of door hinges, or chirping grasshoppers.

If  $\gamma < 1$ , and  $U_{tot}$  exhibits only one stable minimum for every supported position, the probe still follows the sinusoidal potential, but the motion is smooth and no longer discontinuous, as observed in various experiments.<sup>[56,59,63]</sup>

Several modifications exist of the model to account for various experimental conditions and constraints. One of the most important extensions is the incorporation of thermal fluctuations, which are used to explain the velocity dependence of friction on the nanometer scale as well as to predict the outcome of temperature dependent friction measurements.<sup>[1,2,64–71]</sup>

Other models based on the PT-model, such as the Frenken-Kontorova (FK), or the Frenken-Kontorova-Tomlinson (FKT) model extend the contact to numerous point masses, which are in themselves interconnected with springs (see fig. 2.8).<sup>[72]</sup> As a result of the coupling between masses, a collective slip of the point masses from one minimum to the next can occur in the FK- and FKT-model. This phenomenon of collective slip can be described, in analogy to the dislocation movement in crystals, as a “slip-pulse” moving through the interface. Models in which this phenomenon is dealt with further<sup>[73]</sup> contain attempts to relate the energy dissipation in the PT-model to the crystal structure of the materials in contact and interface defects.

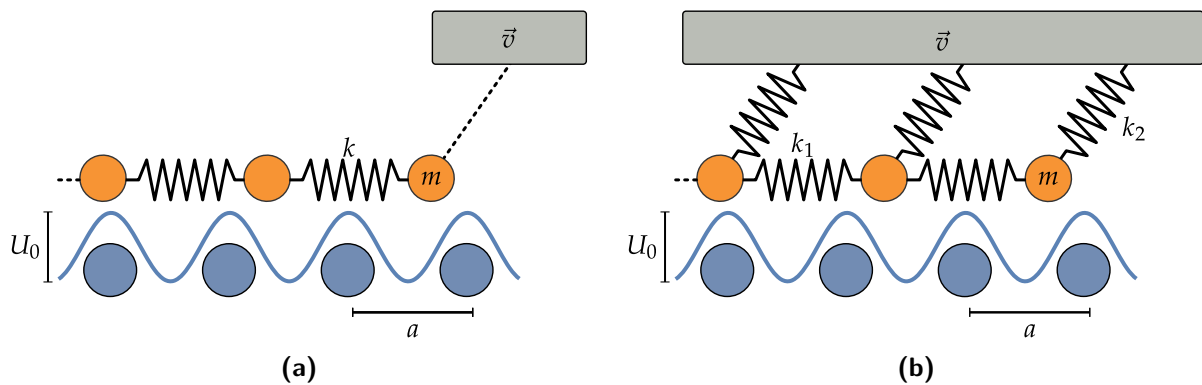


**Figure 2.8:** **(a)** FK-model: a chain of masses  $m$  coupled via springs  $k$  is dragged over a periodic potential with a velocity  $\vec{v}$ . **(b)** FKT-model: a chain of point masses  $m$  coupled to the nearest neighbors via springs  $k_1$  and to the rigid support with springs  $k_2$  is dragged over a periodic potential. Due to the coupling of the masses, the collective slip of the point masses into the next potential minimum can be observed.

Due to the additional degrees of freedom, such as the commensurability between sliding and

stationary atoms, these models are closer to real systems, however because of the simplicity, the PT-model is used as a basis for further considerations in most cases.<sup>[54,74]</sup>

### 2.2.2. Velocity Dependence and Thermal Effects

In the previous consideration of the PT-model the energy of the system is abruptly and completely dissipated after each jump. Furthermore, the amount of dissipated energy is independent of temperature, velocity, or other physical dissipation processes. To account for this inadequacy, a damping term  $\eta$  was introduced in eq. 2.19 without addressing its actual physical origin.

In the PT-model thermal effects can be understood as a randomly occurring lateral force  $F_{th}(t)$ , where  $F_{th}$  exhibits stochastic behavior without correlation over time, such that  $\langle F_{th} \rangle = 0$ .<sup>[75-77]</sup> Due to the additional thermal energy, the tip can overcome the energy barrier between potential minima even if the required energy is greater than zero ( $\Delta E > 0$ ). The probability  $p(t)$  that the tip remains pinned in a potential minimum after a time  $t$  is given by the differential equation:<sup>[64]</sup>

$$\frac{dp(t)}{dt} = -f_0 \exp\left(-\frac{\Delta E}{k_B T}\right) p(t), \quad (2.22)$$

where  $f_0$  denotes the resonance frequency of the tip. Based on this concept, assuming a linear relation between friction force  $F_F$  and  $\Delta E$ , Gnecco et al.<sup>[64]</sup> developed a theoretical model that accounts for the observed velocity dependencies, at finite temperatures

$$F_F(v, T) = F_0 - \frac{k_B T}{a} \log \frac{v}{v_0}, \quad (2.23)$$

with the scaling constant  $F_0$ , the lattice spacing  $a$ , the velocities  $v$  and  $v_0$ , and temperature  $T$ . According to eq. 2.23, the slower the tip moves, the higher the probability that the tip will jump to the next equilibrium position due to thermal activation. Sang et al.<sup>[65]</sup> further refined the model leading to the master equation:

$$F_F(v, T) = F_0 - \left(\frac{k_B T}{a} \log \frac{v_c}{v}\right)^{2/3} \quad (2.24)$$

for velocities below the critical velocity

$$v_c = \frac{\pi\sqrt{2}}{2} \log \frac{f_0 k_B T}{ka}. \quad (2.25)$$

The model predicts that at high velocities thermal vibrations do not contribute and a transition from a logarithmic to no dependency on velocity occurs, which has been observed experimentally.<sup>[14,64,67]</sup>

While the presented model can be used to describe the experimental observation that friction decreases steadily with increasing temperature<sup>[1,2,14,70,78]</sup> it does not capture the experimentally observed strong increase in friction at cryogenic temperatures.<sup>[71,78,79]</sup> An approach to incorporate these observations was postulated by Barel et al.<sup>[80,81]</sup> In this multi contact model, the measured friction is not only attributed to the thermally activated crossing of the energy barriers, but also to the dynamic formation and breaking of adhesive contacts in the interface.

## 2.3. Dissipation Mechanisms

Even though models presented in the previous sections can be used to account for changes in friction due to changes in ambient temperature and the velocity, they are still insufficient to decipher the mechanisms underlying the energy dissipation due to friction. To further decipher the different contributions, the following section will contain a summary of models used to describe frictional losses due to excitation of phonons and interactions linked to the interactions with the electron system, which are generally assumed to be the dominant dissipation channels.<sup>[1,2,14–24]</sup>

$$F_F = F_{ph} + F_{el} \quad (2.26)$$

However, which dissipation channels dominate varies greatly depending on the system, and the interpretations provided are not necessarily consistent.<sup>[20–23]</sup>

### 2.3.1. Phononic contributions

The theoretical description of the phononic contributions to friction is based on experimental studies by Krim et al. where the sliding friction of adsorbed krypton (Kr) on gold (Au) was investigated under UHV conditions.<sup>[82]</sup>

When Kr is adsorbed onto Au, liquid phase islands are formed in that grow with increasing adsorbed Kr and ultimately form a full liquid monolayer. If more and more Kr is adsorbed, the liquid becomes denser and eventually undergoes a phase transition into a crystalline state that is incommensurate with the underlying Au substrate.<sup>[82]</sup>

The authors observed that in contrast to macroscopic measurements, the solid monolayer did

not show a static friction component. In contrast, both the liquid and solid phase followed a viscous friction law, that can be expressed by: [82,83]

$$F_F = \eta_{ph} v A_R = \frac{m}{\tau_s} v \quad (2.27)$$

where  $A_R$  is the contact area,  $\eta$  a shear stress per unit velocity,  $m$  the mass of the sliding object and  $\tau_s$  a characteristic slip-time. The slip-time describes the rate of momentum transfer between substrate and adsorbate.

Building on the viscous model, Smith et al. [83] developed an analytical model which links the dissipation rate  $\tau_s$  to the anharmonic coupling of phonons in the adsorbate monolayer:

$$\frac{1}{\tau_s} = \frac{2S(G)}{N} \frac{1}{\tau_{ph}}. \quad (2.28)$$

The normalized structure factor  $S(G)/N$  describes how much the adsorbate deforms to match the periodic substrate potential. The inverse phonon-lifetime  $1/\tau_{ph}$  is a measure of the rate at which energy is transferred to other phonons. The model thus directly links the dissipation observed in an experiment to the phononic degrees of freedom of the materials in contact

$$F_F \propto \frac{1}{\tau_s} \propto \frac{1}{\tau_{ph}}. \quad (2.29)$$

A similar model was proposed by Bo Persson, [84] but with the key difference that the model relates the dissipation rate of mechanical energy to inelastic collisions between adsorbate atoms and the surface while sliding, using an elastic continuum model. In the model the friction force per adsorbed atom is expressed as

$$F_F = -\eta_{ph} m v, \quad (2.30)$$

where

$$\eta_{ph} \approx \frac{3m}{8\pi\rho} \left( \frac{\omega}{c_T} \right)^3 \omega. \quad (2.31)$$

Here  $\rho$  correspond to the mass density,  $c_T$  the transverse speed of sound and  $\omega$  is the phonon resonance frequency for both parallel and perpendicular vibrations. In this model  $\eta_{ph}$  can be recognized as a material-specific damping constant that are related to phonic contributions. [84]

### 2.3.2. Electronic contributions

For metals and semiconductors, the friction measured at the surface can be additionally influenced by interactions with the electronic degrees of freedom. Analogous to the absorbate model presented in the previous section, the component of the frictional force introduced by electronic interactions can be written as<sup>[84]</sup>

$$F_F = \eta_{el} m v, \quad (2.32)$$

where  $m$  represents the absorbate mass and  $v$  the sliding velocity. In the absorbate model of Persson the damping coefficient  $\eta_{el}$  is attributed to the excitation of electron-hole pairs in the metal and can be expressed as<sup>[84]</sup>

$$\eta_{el} = \frac{n^2 e^2 d}{n_a m} \Delta \rho. \quad (2.33)$$

The parameter  $n_a = N_1/A$  corresponds to the number of absorbates per unit area,  $\Delta \rho$  to the film resistivity,  $d$  to the film thickness and  $n$  the number of conducting electrons per unit volume.<sup>[84]</sup>

Theoretical estimates of the damping factor, based on the generating electronic excitations near the Fermi energy that get dragged behind the tip, are in good agreement with non-contact friction studies.<sup>[17,85]</sup> However, they are too small to account for the observed changes in friction forces measured in the contact friction experiments.<sup>[2,14,16]</sup> This suggests that other dissipation mechanisms presumably overshadow the viscous electronic contributions in contact friction experiments.

For insulating materials, additional capacitive effects can occur due to localized surface charges that are created by the sliding contact. This phenomenon is referred to as the triboelectric effect.<sup>[86]</sup> Experimental studies have shown that this effect can have a large influence on the friction measured, as well as possibly on the friction coefficient.<sup>[18,19]</sup> The effect is particularly pronounced for materials that are well separated, regarding their triboelectric properties.<sup>[87]</sup>



## 3. Manganites

Strongly correlated transition metals such as lanthanum strontium manganite ( $\text{La}_{(1-x)}\text{Sr}_x\text{MnO}_3$ ) and superlattice systems such as  $[\text{LaMnO}_3]_m/[\text{SrMnO}_3]_n$  are characterized by rich, well-characterized phase diagrams, known electronic, magnetic and phonic properties, as well as smooth (roughness  $RMS < 1$  nm) and surfaces. These systems are therefore an ideal candidate to test the correlation between frictional losses and the physical properties of the sample system, in an AFM experiment. The physical properties of the system are presented below, which form the basis for the appropriate interpretation of the friction experiments conducted in this work.

### 3.1. Crystal Structure

Manganites with the molecular formula  $\text{ABO}_3$  crystallize in different variants of the perovskite structure, depending on the atoms occupying the lattice sites and their ionic radii. The A lattice site (see fig. 3.1) in the systems studied in this work is occupied by either strontium (Sr) or lanthanum (La), and the B-site by a manganese-ion (Mn). The Mn-ion is surrounded by an oxygen (O) octahedron.

Depending on the ionic radii  $R_{A/B/O}$  the lattice structure can deviate from the ideal cubic perovskite structure, a measure for the deviation is the so-called Goldschmidt tolerance factor<sup>[88]</sup>

$$t = \frac{1}{\sqrt{2}} \frac{R_A + R_O}{(R_B + R_O)}. \quad (3.1)$$

In the case of  $t = 1$ , a cubic structure  $Pm\bar{3}m$  is present. A deviation from  $t = 1$  causes the oxygen octahedra to tilt, which in turn affects the electrical and magnetic properties, as discussed below. For  $0.96 < t < 1$ , a rhombohedral, structure  $R\bar{3}c$  is present and even smaller tolerance factors lead to an orthorhombic structure  $Pnma$ .<sup>[89]</sup>

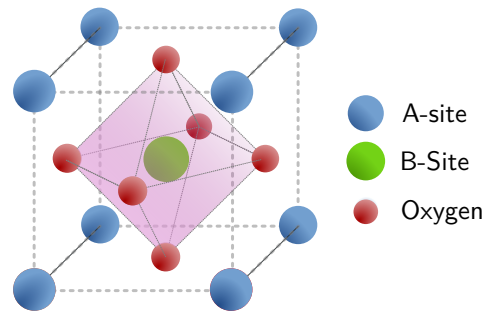


**Figure 3.1:** Unit cell of a perovskite structure of the type  $ABO_3$ . The corners of the unit cell are occupied by the A-site ions (La or Sr). In the center of the unit cell, surrounded by six oxygen atoms, resides the B-site ion (Mn).

## 3.2. Electric and Magnetic Properties

The electronic properties of the investigated perovskites depend fundamentally on the orbital structure of the manganese ions and their hybridization with the neighboring oxygen ions. In the following section, their interactions in the crystal field are first described. Subsequently, the relevant transport mechanisms are presented.

### 3.2.1. Jahn-Teller-Effect

In an undisturbed state, the 25 electrons of the manganese populate the two  $4s$ -orbitals and fill the five  $3d$ -orbitals, resulting in an electron configuration of  $[Ar]3d^54s^2$ . While in an undisturbed state the five  $3d$ -orbitals are degenerate, the interaction with the six adjacent oxygen atoms in a perovskite lattice leads to a splitting of the  $3d$ -orbital into three  $t_{2g}$ -orbitals (pointing between the anions) and two  $e_g$ -orbitals (pointing towards the anions). The energy difference between the  $t_{2g}$  and  $e_g$ -orbitals is approximately  $\Delta_{CF} \approx 1$  eV (see fig. 3.2), due to the Coulomb potential.<sup>[89,90]</sup> Furthermore, the valence of the manganites is determined by the valence of the ion occupying the A-site (La/Sr); thus, the manganese ions can be present in an +3 or +4 oxidation state, with an electron configuration of  $[Ar]3d^4$ , or  $[Ar]3d^3$  respectively.

Due to the degeneracy of the  $t_{2g}$ - and  $e_g$ -orbitals, the system is unstable and will reduce its symmetry to counteract the degeneracy. This can be achieved by elongating the bonds in the  $z$ -direction ( $d_{z^2}$ ) while shortening the bonds in the  $xy$  direction ( $d_{x^2-y^2}$ ) or vice versa. In both cases, the overall energy is reduced.<sup>[91]</sup> This so called Jahn-Teller-effect (JT-effect), which occurs predominately in systems with an odd number of electrons populating the  $e_g$ -orbital (e.g., in the case of  $Mn^{3+}$ ),<sup>[91]</sup> leads to a Jahn-Teller splitting of about  $\Delta_{JT} \approx 0.7$  eV.<sup>[92]</sup> The elongation of the bonds continues until the resulting energy gain due to Jahn-Teller distortion

is balanced by the elastic energy due to lattice distortion.

In the systems like  $\text{Mn}^{4+}$ , with an even number of electrons populating  $e_g$ -orbital, the  $t_{2g}$ -orbitals are occupied by one electron each. Under Jahn-Teller distortion, there would be no energetic gain because the changes compensate each other –  $\text{Mn}^{4+}$  is not *Jahn-Teller active* and consequently stabilizes the octahedral symmetry.<sup>[91]</sup>

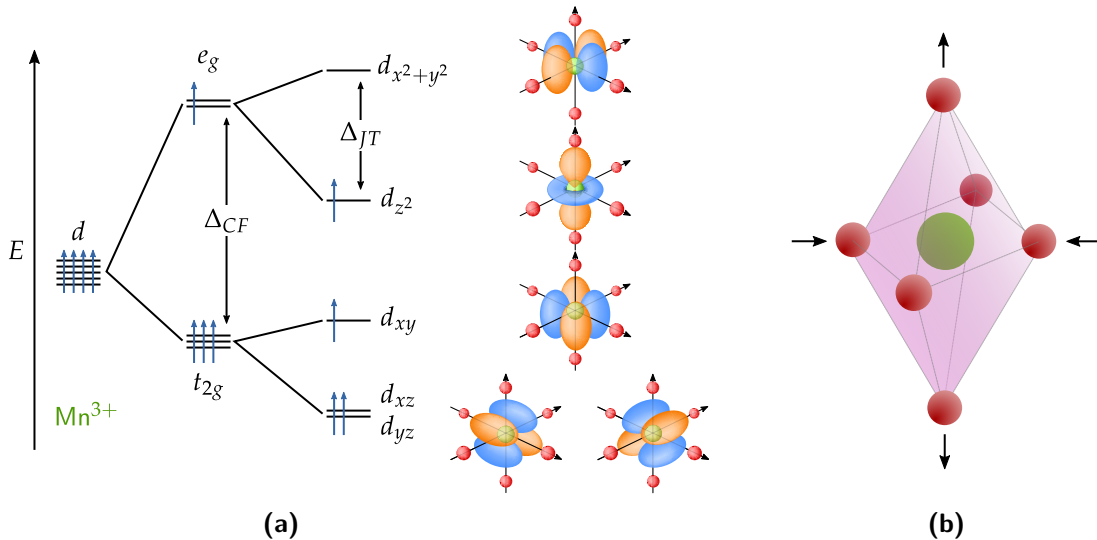


**Figure 3.2:** (a) Elimination of the energy degeneracy by crystal field splitting and Jahn-Teller distortion using the example of a  $\text{Mn}^{3+}$  ion. The crystal field energy  $\Delta_{CF}$  splits the  $3d$ -orbitals into  $t_{2g}$ - and  $e_g$ -levels. These levels split further by a Jahn-Teller distortion. (b) The Jahn-Teller distortion leads to the further energy gain  $\Delta_{JT}$  by reducing the overlap between the  $d_{z^2}$ -orbital of manganese and the  $2p$ -orbital of oxygen-ions via elongation in the  $z$ -direction.<sup>[93]</sup>

### 3.2.2. Double-Exchange

In transition metals such as  $\text{La}_{(1-x)}\text{Sr}_x\text{MnO}_3$ , doping with strontium results in a mixed valence of  $\text{Mn}^{3+}$  and  $\text{Mn}^{4+}$ . In these systems, the so-called double exchange mechanism plays an important role, providing a qualitative description of the ferromagnetism in manganites as well the underlying mechanisms of charge transport.<sup>[94–96]</sup>

In the double exchange model, electron transfer through the crystal lattice takes place by simultaneous hopping of an  $e_g$ -electron from a  $\text{Mn}^{3+}$  into an oxygen  $2p$ -orbital with the same spin orientation, and from there to an adjacent  $\text{Mn}^{4+}$ . At the end of this process, an electron has hopped between the adjacent ions, while retaining its spin (see fig. 3.3).

In the double exchange model it is predicted that the mobility of electrons is higher if the

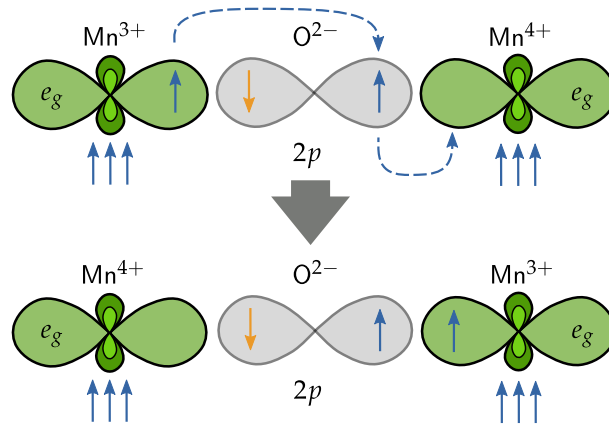


**Figure 3.3:** Double exchange between  $Mn^{3+}$  and  $Mn^{4+}$  via an oxygen-ion. An  $e_g$ -electron hops from a  $Mn^{3+}$  site to a neighboring  $O^{2-}$   $2p$ -orbital, from which an electron of the same spin is transferred to an adjacent  $Mn^{4+}$ -ion. The strong Hund's coupling allows this exchange only for parallel aligned spins; thus a ferromagnetic ordering is present. In this scenario, charge transfer takes place.

hopping electron does not need to change its spin, i.e., under ferromagnetic order. Thermal deviation of the spin orientation  $\theta$  from the ideal, parallel alignment thus increase the electrical resistance. The dependence of tilt angle and electrical conductivity is given by the transfer integral<sup>[95]</sup>

$$S_{eff} = t \cdot \cos\left(\frac{\theta}{2}\right), \quad (3.2)$$

The magnitude of the integral depends on the spatial overlap of the manganese and oxygen-ions. This in turn is determined by the tilting of the neighboring oxygen octahedra  $\varphi$ , and thus related to the tolerance factor  $t \propto \cos(\varphi)$ .<sup>[90]</sup> Therefore, a direct dependence of the electronic properties on the tolerance factor  $t$  arises, and thus the average radii of the A-site atom.

### 3.2.3. Super-Exchange

In addition to the double-exchange model, which can be used to describe the ferromagnetism of manganites, the super-exchange provides a quantitative description of the antiferromagnetic states in mixed-valent manganites.

The super-exchange is different from the double-exchange mechanism in that there is a coupling between neighboring cations without the participation of an intermediate anion, and as such, it is a virtual hopping process. In this model, one energy level is available to each electron on each lattice site. The number of electrons available for conduction is therefore equal to the

number of lattice sites.<sup>[93]</sup>

Consider two Mn-ions in proximity: If the spins of two adjacent  $e_g$ -electrons are parallel aligned, hopping of the electrons between orbitals is forbidden due to the Pauli principle (see fig. 3.4a), thus no energy is gained  $\Delta E = 0$ . If the spins are antiparallel aligned, electrons can virtually hop between lattice sites. The gain in energy is inverse proportional to the Coulomb energy  $U$ , and proportional to the hopping probability  $p$  (see fig. 3.4b).<sup>[93,97]</sup> Hence, an antiparallel orientation of the spins, resulting in an antiferromagnetic order, is favored. However, since there is no net electron transport, the manganite remains insulating. Such materials, e.g., lanthanum manganite ( $\text{LaMnO}_3$ ), are referred to as *Mott-Hubbard insulators*.<sup>[93,98,99]</sup>

In the super-exchange model, the degeneracy of the  $e_g$  states of the manganese ions has been neglected, which means that hopping processes due to the Pauli principle cannot be completely excluded. A more detailed description is provided by the *Goodenough-Kanamori-Anderson* rules.<sup>[93,98,100,101]</sup>

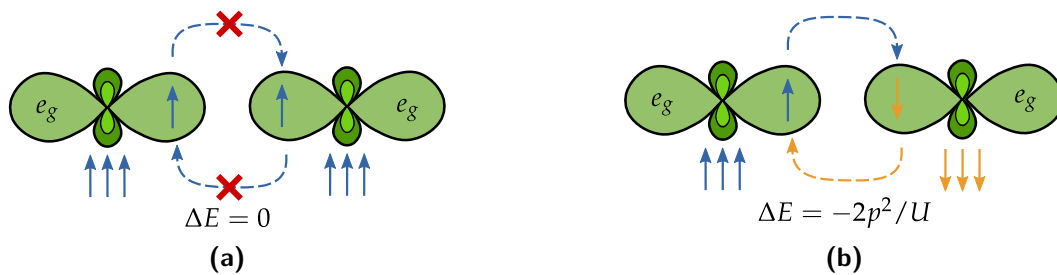


**Figure 3.4:** Super exchange between two  $d_{z^2}$ -orbitals: The antiparallel spin orientation **(b)** is energetically favored as virtual hopping processes are allowed between orbitals.

### 3.2.4. Polarons

The double- and super-exchange mechanism can be used to account for ferro- and antiferromagnetic properties of manganites under certain conditions; however, they are insufficient to explain the phenomenological versatility and phase richness of these systems.<sup>[102,103]</sup>

This shortcoming was resolved by the development of models that account for contributions due to electron-phonon interactions, i.e., polarons.<sup>[104]</sup> In its essence, the term polaron describes an electron along with its distortion field as a quasi-particle. In manganites, the combination of an  $e_g$ -electron and the local distortion of the  $\text{MnO}_6$  octahedron in which it dwells, resulting from the JT-effect, is called a Jahn-Teller-polaron (JT-polaron).<sup>[93]</sup> Due to the local lattice distortion, a JT-polaron influences surrounding lattice atoms and thus other JT-polarons. This

can give rise to so-called correlated JT-polarons, which are often measured in connection with the CMR-effect and near the Curie temperature  $T_C$ .<sup>[89]</sup> Correlated polarons are observed in systems with large electron-phonon coupling and have a coherence length significantly greater than the lattice constants.<sup>[93,105]</sup> These polarons are also referred to as large polarons and are detected in systems such as  $\text{La}_{(1-x)}\text{Sr}_x\text{MnO}_3$ , especially above  $T_C$ .<sup>[106,107]</sup>

Due to the double exchange, other types of polarons are conceivable, including orbital and dielectric polarons. An orbital polaron consists of a cluster of neighboring  $\text{Mn}^{3+}$  sites whose  $d$ -orbitals point toward a central  $\text{Mn}^{4+}$  vacancy.<sup>[108]</sup> A dielectric polaron decreases the distance between surrounding oxygen-ions closer due to the smaller ionic radius of the  $\text{Mn}^{4+}$ .<sup>[93]</sup>

### 3.3. Phase Diagram of Lanthanum Strontium Manganite

The phase diagram, of lanthanum strontium manganite ( $\text{La}_{(1-x)}\text{Sr}_x\text{MnO}_3$ ) exhibits a large phase variety, which makes it possible to obtain large changes in the transition temperatures  $T_C$ , and the formation of different phases by small changes in the doping with Sr (see fig. 3.5).<sup>[99]</sup>

In an undoped case ( $\text{LaMnO}_3$ ), where only super-exchange is possible, antiferromagnetic ordering is present, and the large Coulomb repulsion leads to the localization of  $e_g$ -electrons.<sup>[99]</sup>  $\text{LaMnO}_3$  exhibits orbital ordering below 780 K and an orthorhombic structure that is Jahn-Teller distorted.<sup>[109]</sup>

In the maximum doped case ( $x = 1$ ), for pure strontium manganite ( $\text{SrMnO}_3$ ), the  $e_g$ -orbitals are unoccupied, and a band insulator is present. Due to a Goldschmidt tolerance factor of  $t \approx 1.02$ , a hexagonal structure is present, but under certain conditions cubic modifications are possible.<sup>[110,111]</sup>

In the range of  $x \approx 0.17 - 0.50$ ,  $\text{La}_{(1-x)}\text{Sr}_x\text{MnO}_3$  exhibits a ferromagnetic-metallic phase caused by ferromagnetic double exchange below the transition temperature  $T_C$ . In the transition region, no simple explanations for the magnetic ordering of the manganites can be given. The competition between double and super-exchange leads to a complicated behavior, which, especially in the case of  $\text{LaSrMnO}$ . It is characterized by the coexistence of ferromagnetic and antiferromagnetic phases. Detailed descriptions of these phases can be found, for example, in the publication by Dagotto et al.<sup>[90]</sup>

In the present work, temperature-dependent friction measurements were carried out on a  $\text{La}_{(1-x)}\text{Sr}_x\text{MnO}_3$  sample with a doping of  $x = 0.2$ , in a temperature range between 100 and

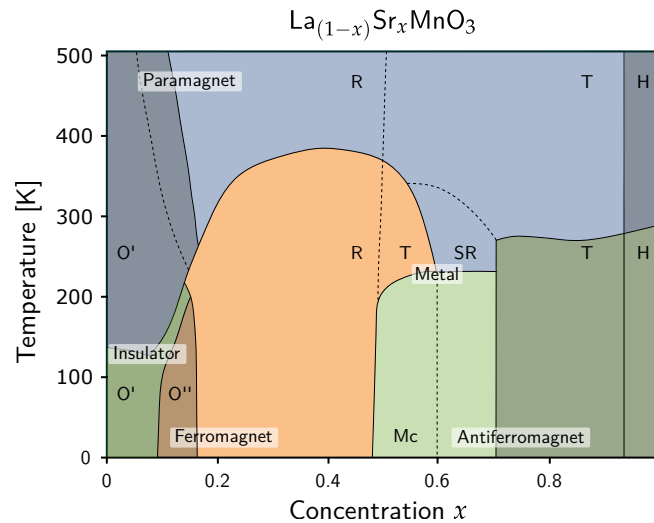


**Figure 3.5:** The  $\text{La}_{(1-x)}\text{Sr}_x\text{MnO}_3$  phase diagram contains ferromagnetic (orange), paramagnetic (blue), and antiferromagnetic (green) regions that are either metallic (light) or insulating (dark). Depending on the phase doping and temperature different symmetries are formed: Jahn-Teller distorted orthorhombic ( $O'$ ), orbital-ordered orthorhombic ( $O''$ ), rhombohedral ( $R$ ), tetragonal ( $T$ ), monoclinic ( $Mc$ ), and hexagonal ( $H$ ). Phase diagram reproduced based on a publication by Hemberger et al.<sup>[103]</sup>

300 K. The films used were prepared by sputter deposition and characterized in the context of the master thesis of Tim Sievert.<sup>1</sup> For this thesis, he optimized the sputter deposition technique to lower the Curie temperature of the films deposited by around 100 K.<sup>[112]</sup>

Furthermore, superlattice systems consisting of alternating  $\text{LaMnO}_3$  and  $\text{SrMnO}_3$  were investigated. These films were prepared by Leonard Schüler<sup>2</sup> using metalorganic aerosol deposition (MAD),<sup>[113]</sup> and their special properties are described in the following.

### 3.4. Superlattices

In addition to the phase transitions presented in the previous section, the targeted introduction of interfaces into materials can be used to vary the material properties while preserving the surface chemistry. One class of materials that has these properties are so-called superlattice samples, which enable the phonon mean free path to be varied by introducing interfaces.<sup>[114–117]</sup>

Seven films, consisting of alternating  $[\text{LaMnO}_3]_m$  and  $[\text{SrMnO}_3]_n$ -layers, where  $m$ ,  $n$  corre-

<sup>1</sup>Institute of Materials Physics, University of Göttingen, Friedrich-Hund-Platz 1, Göttingen 37077, Germany – AG C. Jooss

<sup>2</sup>1st Physics Institute, University of Göttingen, Friedrich-Hund-Platz 1, 37077 Göttingen, Germany – AG V. Moshnyaga

spond to the number of layers, were used in the present work to clarify open questions arising from the temperature dependent friction measurements,<sup>[2]</sup> as well as friction studies that used resistive switching at the surface, as a control technique.<sup>[1]</sup> The samples used were prior to this work characterized by thermal transient reflectometry (TTR) measurements (see fig. 3.6) and exhibit vastly different thermal and magnetic properties in respect to their  $m/n$ -ratio.<sup>[117]</sup>

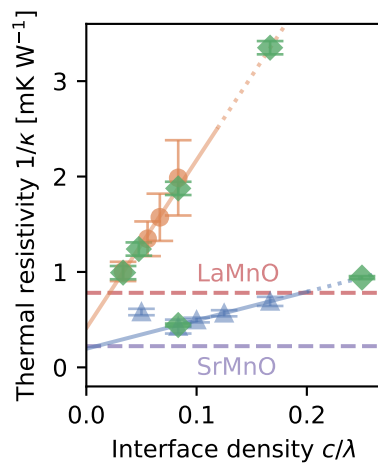


**Figure 3.6:** TTR measurements by D. Meyer et al.<sup>[117]</sup> revealed a scaling of the thermal properties with respect to the interface density  $c/\lambda = 1/(n+m)$ . The data, provided by the authors (circles and triangles) was used to estimate the thermal resistivity for the samples studied in this work (diamonds).

## 4. Atomic Force Microscopy

The invention of the scanning tunneling microscope (STM) in the 1980s facilitated the development of many other scanning probe microscopy (SPM) techniques, including the atomic force microscope (AFM) by Binnig et al. in 1985.<sup>[118]</sup> All these techniques utilize a range of physicochemical interactions between a tip and a surface to image surface properties on the sub-nanometer scale. The AFM excels in particular through its high resolution of topographies with a sub-nanometer accuracy. In addition, the AFM turned out to also be a useful tool to study the physical origins of friction on a single asperity level, as pioneered by Mate et al.<sup>[59]</sup>

Nowadays, the AFM is widely used, in various disciplines, because of its versatility: it can image all materials whether hard or soft, irrespective of opaqueness or conductivity. Besides the topography mapping, it can be used to characterize localized surface charges and elastic properties. Furthermore, various types of spectroscopy measurements can be performed.

In the following chapter, the operation of the AFM used in this work is explained. The setup was used to study the energy dissipation at a single asperity frictional contact into the surrounding sample material. Based on this method, the operating principle of the lateral force microscopy (LFM)<sup>[119]</sup> and the calibration of the forces are described.

### 4.1. Basic Principle

An AFM unit comprises a cantilever beam attached on one side to a piezoelectric actuator, and a  $xy$ -stage, on which the specimens to be examined are mounted. This setup enables investigations of samples in all spacial directions (see fig. 4.1). In the following, we will refer to the direction parallel to the long cantilever axis as the  $y$ , and the axis perpendicular to the  $y$ -axis and parallel to the surface  $x$ -axis. The spatial directions described are indicated in fig. 4.1. In typical AFM experiments there is a distinction made between static and dynamic operation modes, where the latter ones are based on the concept that the cantilever is excited to oscillation near its resonance frequency, the interaction forces between cantilever and sample are then detected by shifts in the oscillation frequency of the cantilever. The mode used

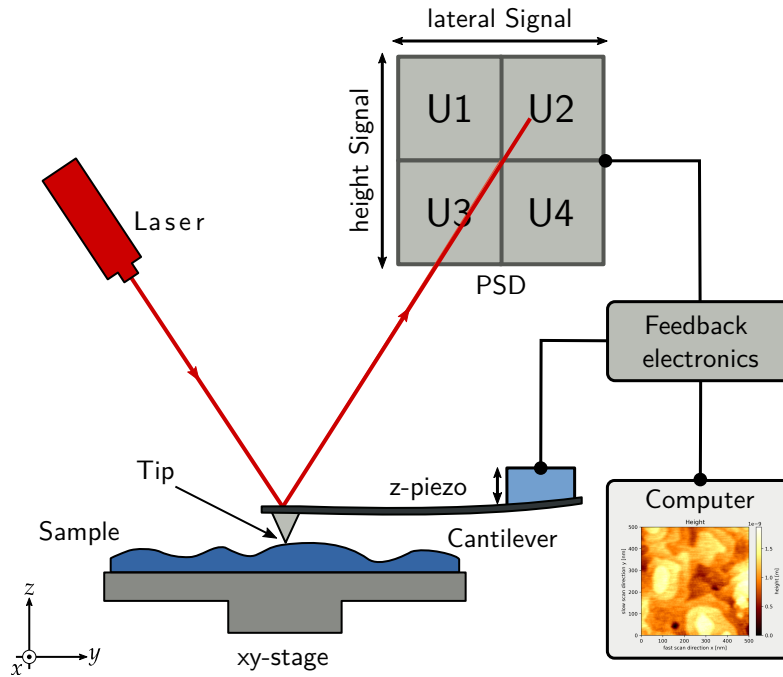


**Figure 4.1:** Principle of operation of a small sample AFM. The interaction between the tip and the sample causes the laser spot on the PSD to displace. By scanning the sample line by line and recording the PSD signal, conclusions can be drawn about the topography, friction, and other material properties.

predominantly in this work is one of the static mode category. For this, the cantilever is pressed onto the sample surface with a constant normal force  $F_N$  and the bending of the cantilever can be used as a feedback signal during the scan.

If the tip is lowered and brought in to contact with the substrate, the acting forces between tip and sample (see section 2.1.3) cause a deflection of the cantilever beam, which can be detected via a laser beam reflected at the rear side of the cantilever onto a four-quadrant position sensitive detector (PSD). The advantage of this type of detector is that both the bending and the torsion of the cantilever can be measured simultaneously during the scan. From the measured signals, the normal, and lateral bending of the cantilever can be determined by:

$$U_N = (U_1 + U_2) - (U_3 + U_4) \quad (4.1)$$

$$U_L = (U_1 + U_3) - (U_2 + U_4) \quad (4.2)$$

where the normal  $U_N$  and lateral signal  $U_L$  are directly proportional to the normal force  $F_N$  and lateral force  $F_L$  acting on the cantilever.<sup>1</sup> To map the topography of a sample, the tip is dragged over the substrate surface in a grid pattern along the  $x$ - and  $y$ -direction, while the  $z$ -displacement of the piezo as well as the PSD-readouts are recorded. At the same time the applied normal force is kept constant. If the normal force deviates from a pre-defined set point,  $F_{N,spt}$  during scanning the  $z$ -piezo is re-adjusted to regulate the normal force to the target value. The combination of all signals allows the reconstruction of a plane of constant normal load, that can be interpreted as a topography map of the sample investigated.

### 4.1.1. Force-Distance-Curves

The forces acting between the cantilever and the specimen are distance-dependent (see section 2.1.3) and vary in terms of their magnitude. To characterize these interactions in an AFM experiment, so called force-distance-curves (FD-curves) can be recorded (see fig. 4.2). These curves are obtained by approaching the cantilever towards the sample from a "large" distance, while at the same time recording the distance dependent deflection of the lever  $U_N$ .

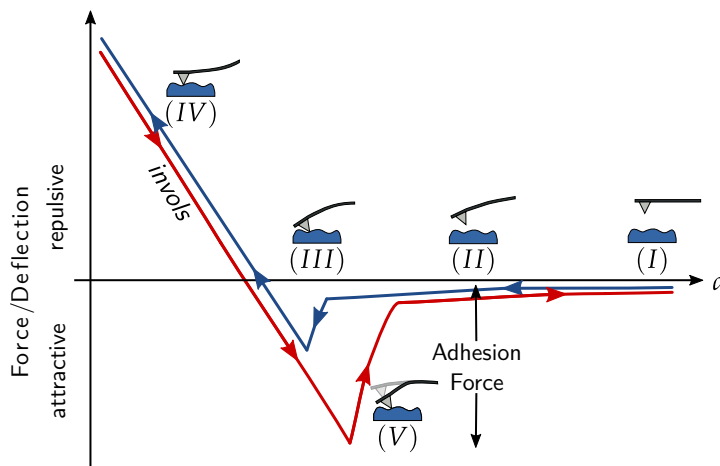


**Figure 4.2:** For large distances between tip and sample, the forces acting are insufficient to deflect it from its resting position (I). If the distance is decreased (II), the attractive interaction forces become larger and deflect the cantilever towards the sample. At a critical distance (III), the attractive forces become large enough so that the tip snaps into contact with the sample (snap-on). Decreasing the distance further (IV) results in an indentation of the cantilever and thus repulsive forces. These forces increase linearly with decreasing distance. By retracting the cantilever, the repulsive forces decrease again, and adhesive forces retain the tip on the specimen. These adhesive forces must be exceeded to detach the cantilever from the surface (V).

<sup>1</sup>Methods used to convert voltages into forces is described in section 4.1.2.

For large distances between the tip and the sample  $d > 100$  nm (see fig. 4.2(I)), the acting forces are attractive and consist of electrostatic and van der Waals forces.<sup>[44]</sup> When the tip approaches the sample surface, the forces acting on the lever increase. At a critical distance (see fig. 4.2(II)), the forces are large enough to overcome the restoring force of the cantilever beam

$$F_R = -c_N \cdot \Delta z, \quad (4.3)$$

and the tip is deflected towards the sample surface. If the distance is steadily reduced further, the attractive forces become large and the distance eventually is small enough so that the cantilever-tip snaps into contact with the sample surface (see fig. 4.2(III) – snap-in). Moving the cantilever further towards the sample leads due to repulsive interactions with the sample, and to a bending of the cantilever away from the sample direction. With decreasing distance, the force acting on the cantilever increases linearly (see fig. 4.2(IV)). In this linear regime, the cantilever tip and sample are in contact. The force measured here equates to the normal force  $F_N$  applied in a contact AFM experiment.

Retracting the cantilever from the sample initially reduces the force on the cantilever again, but adhesive forces initially retain the tip on the sample surface even when no or a negative normal force is applied. Further retraction of the cantilever increases the restoring forces. If these restoring forces become greater than the adhesive forces  $F_0$  retaining the tip on the surface, the tip snaps off (see fig. 4.2(V)) and the cantilever restores to its initial state (see fig. 4.2(I)).

### 4.1.2. Force Calibration

To be able to make quantitative statements about the forces between the tip and the sample in an experiment, it is necessary to calibrate the system beforehand. A first step in this process is to determine the spring constants of the cantilever in the normal  $c_N$  and the lateral direction  $c_L$ . The spring constants can be determined based on the geometrical properties of the cantilever used: width  $w$ , thickness  $t$ , length  $l$  and tip height  $h$ . These properties can be obtained from scanning electron microscope (SEM) measurements of the cantilever (see fig. 4.3). In particular, the accurate measurement of the thickness  $t$  and the tip height  $h$  is prone to error. Therefore, the thickness of the lever can be determined using an alternative approach that involves determining the resonance frequency of the cantilever  $f_0$  from thermal

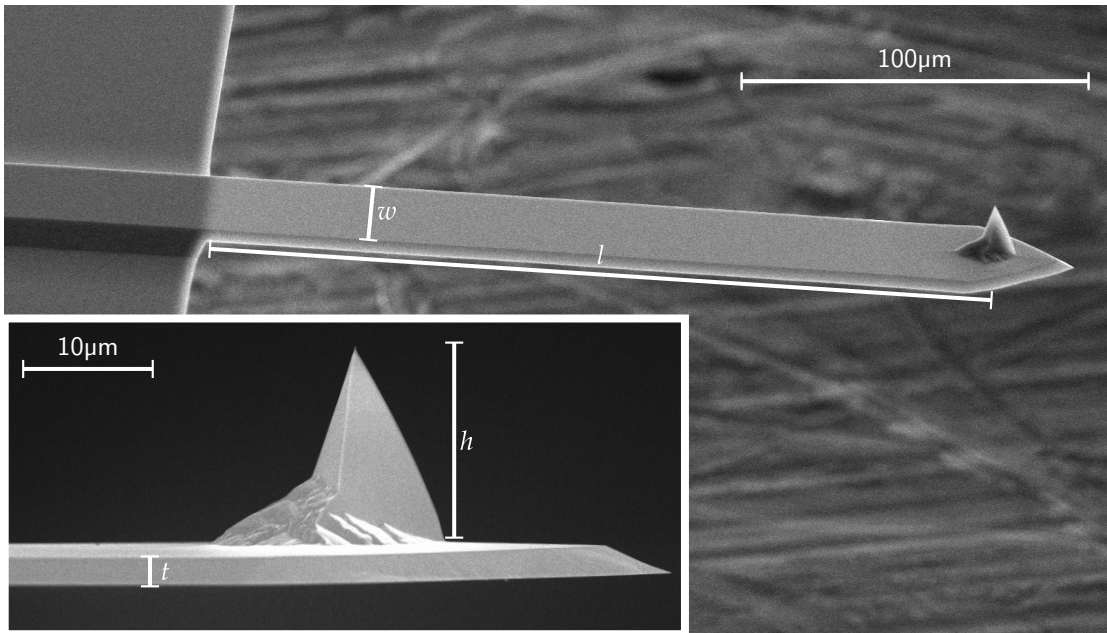


**Figure 4.3:** SEM-measurement of a rectangular silicon cantilever type PPP-LFMR.<sup>[120]</sup> These measurements were used to validate the cantilever dimensions stated by the manufacturer and thus to calibrate the forces measured in an experiment.

noise measurements<sup>[121]</sup>

$$t = \frac{2\sqrt{12}\pi}{1.875^2} \sqrt{\frac{\rho}{E}} f_0 l^2. \quad (4.4)$$

Knowing the cantilever dimensions, the normal and torsional spring constants are given by:<sup>[44]</sup>

$$c_N = \frac{Ewt^3}{4l^3} \quad (4.5)$$

and

$$c_L = \frac{Gwt^3}{3h^2l}. \quad (4.6)$$

In the equations above  $\rho$  is the density,  $E$  the Young's modulus and  $G$  the shear modulus of the cantilever. To calibrate the forces measured in an AFM, the sensitivity of the system  $S_N$  must be determined by measuring a force-distance curve.  $S_N$  is equal to the linearly increasing repulsive force in the contact region (*invol*s, see fig. 4.2(III)). To convert the PSD readouts

$U_N$  and  $U_L$  [V] into forces  $F$  [N] the following relations apply:<sup>[44]</sup>

$$F_N = S_N c_N U_N, \quad (4.7)$$

and

$$F_L = \frac{3h}{2l} S_N c_L U_L. \quad (4.8)$$

## 4.2. Lateral Force Microscopy

Friction forces between a cantilever tip and specimen can be measured by moving in x-direction (perpendicular to the long cantilever axis) while scanning and applying a constant normal force. The forces acting on the tip while scanning lead to a torsion of the cantilever, which can be measured via the lateral signal (see eq. 4.2) of the PSD. These lateral forces can be caused by friction, but can also originate from topography (see fig. 4.4). For example, a large change in the topography can cause a larger torsion of the cantilever, independent of the local friction force. To investigate local friction forces, such effects must first be eliminated. This is achieved by recording so-called friction loops.<sup>[53]</sup> Friction loops are obtained by recording the torsion of

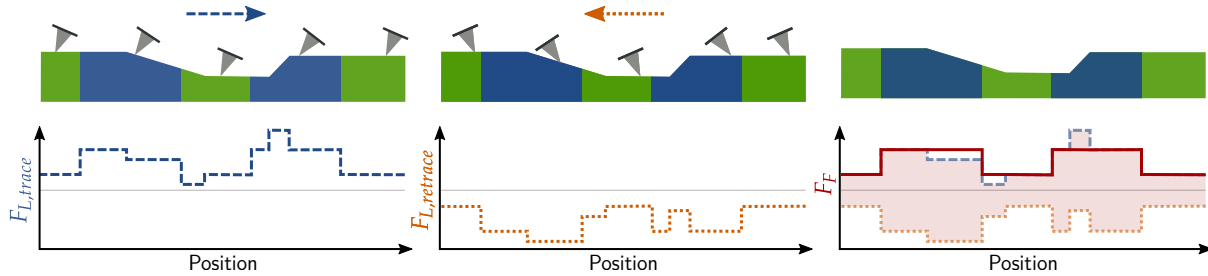


**Figure 4.4:** Friction is measured by recording the torsion of the cantilever as it is moved along the sample surface in the forward ( $F_{L,trace}$ ) and backward ( $F_{L,retrace}$ ) directions. To eliminate topographic artifacts, the difference of the measured torsion of both directions is calculated. This results in a signal proportional to the frictional force ( $F_F$ ) between tip and specimen, and thus to the energy dissipated during sliding.

the cantilever  $\theta \propto U_L \propto F_L$  while scanning the sample along the same line in forward (*trace*) and backward (*retrace*) directions (see fig. 4.4). If the deflection of the cantilever at rest is set to  $\theta = 0$ , a positive torsion is measured in the forward and a negative torsion in the backward direction. If the tip slides over the same sample region, the frictional force remains the same between trace and retrace, whereas topographical influences affect the torsion opposite for the trace and retrace. The local contribution of the friction force is thus obtained by determining

the difference of the deflections of the forward and backward scanning direction,

$$F_F = \frac{F_{L,trace} - F_{L,retrace}}{2}, \quad (4.9)$$

see shaded region fig. 4.4(right).<sup>[122]</sup>

To quantify the frictional behavior between the cantilever tip and specimen surface, the frictional force is typically measured as a function of different normal forces. The plot of the measured friction force for different normal forces is called an Amontons plot, in reference to Amontons laws.

### 4.3. Conductive-AFM

Electronic and electrostatic interactions between tip and sample can have a large influence on the measured forces, see sections 2.1.3 and 4.1.1. To characterize these interactions, the AFM offers the possibility to apply potentials between tip and sample, this method is referred to as conductive AFM (C-AFM). With the setup shown in fig. 4.5, the conductivity of the sample system can be investigated locally. Additionally, when measuring friction, and/or FD-curves as a function of the applied potential, the electrostatic contributions to the forces measured can be characterized (see section 2.1.3).

FD-curves recorded as a function of an applied potential are referred to as spectroscopic measurements.

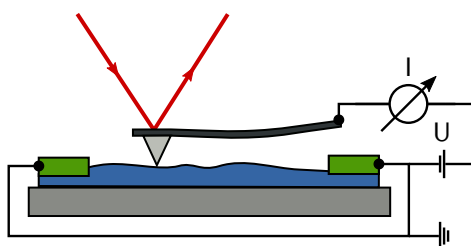


**Figure 4.5:** To perform conductivity measurements, a potential can be applied between the cantilever and sample, and the resulting current flow can be recorded as a function of sample location. Due to the deflection of the cantilever when it is dragged over the sample, a current map can be recorded in addition to the topography and friction map.



## 5. Friction Measurements

In order to address the central question of this thesis "How energy dissipation at a sliding nanoscale contact is connected to the intrinsic properties of the underlying material?" two approaches were followed: First, temperature-dependent friction measurements were performed on a  $\text{La}_{0.8}\text{Sr}_{0.2}\text{MnO}_3$  thin film to investigate the effect of phase transitions on the measured friction forces (see section 5.1). From those measurements, as well as other related studies, the question arose which phonon modes are predominantly dissipating energy and up to which depth material properties contribute to sliding friction. Based on the insights gained and questions raised, friction measurements were performed on seven super lattice samples consisting alternating of  $[\text{LaMnO}_3]_m$  and  $[\text{SrMnO}_3]_n$  layers (see section 5.2).

### 5.1. Polaronic Contributions to Friction in a Manganite Thin Film

The following section was published as "*Polaronic Contributions to Friction in a Manganite Thin Film*" in *Advanced Science* 2003524 (2020). The manuscript was submitted by Niklas A. Weber<sup>1\*</sup>, Hendrik Schmidt<sup>1</sup>, Tim Sievert<sup>1</sup>, Christian Jooss<sup>1</sup>, Friedrich Güthoff<sup>2</sup>, Vasily Moshneaga<sup>3</sup>, Konrad Samwer<sup>3</sup>, Matthias Krüger<sup>4</sup>, Cynthia A. Volkert<sup>1</sup> in 2021 ([Creative Commons Attribution 4.0 International License \(CC BY 4.0\)](#)). The supporting information (SI) are available [online](#),<sup>[2]</sup> the citations and the formatting are adapted to the rest of this thesis.

<sup>1</sup> *Institute of Materials Physics, University of Göttingen, Göttingen, 37077 Germany*

<sup>2</sup> *Institute of Physical Chemistry, University of Göttingen, Göttingen, 37077 Germany*

<sup>3</sup> *1st Physics Institute, University of Göttingen, Göttingen, 37077 Germany*

<sup>4</sup> *Institute for Theoretical Physics, University of Göttingen, Göttingen, 37077 Germany*

## Contributions

Cynthia A. Volkert conceived and supervised the project. Niklas Weber performed all experiments on  $\text{La}_{0.8}\text{Sr}_{0.2}\text{MnO}_3$  and analyzed the data for all experiments shown. Temperature dependent measurements on  $\text{La}_{0.7}\text{Sr}_{0.3}\text{MnO}_3$  were conducted by Hendrik Schmidt. Tim Sievert prepared and pre-characterized the  $\text{La}_{0.8}\text{Sr}_{0.2}\text{MnO}_3$  thin film. Friedrich Güthoff helped to implement the scripts used to conduct the temperature dependent measurements. Christian Jooss, Matthias Krüger, Vasily Moshneaga, Konrad Samwer contributed to the interpretation of the results. All authors contributed to the writing of the manuscript.

### 5.1.1. Abstract

Despite the huge importance of friction in regulating movement in all natural and technological processes, the mechanisms underlying dissipation at a sliding contact are still a matter of debate. Attempts to explain the dependence of measured frictional losses at nanoscale contacts on the electronic degrees of freedom of the surrounding materials have so far been controversial. Here, it is proposed that friction can be explained by considering the damping of stick-slip pulses in a sliding contact. Based on friction force microscopy studies of  $\text{La}_{(1-x)}\text{Sr}_x\text{MnO}_3$  films at the ferromagnetic (FM) metallic to a paramagnetic (PM) polaronic conductor phase transition, it is confirmed that the sliding contact generates thermally activated slip pulses in the nanoscale contact, and argued that these are damped by direct coupling into the phonon bath. Electron-phonon coupling leads to the formation of Jahn–Teller polarons and to a clear increase in friction in the high-temperature phase. There is neither evidence for direct electronic drag on the atomic force microscope tip nor any indication of contributions from electrostatic forces. This intuitive scenario, that friction is governed by the damping of surface vibrational excitations, provides a basis for reconciling controversies in literature studies as well as suggesting possible tactics for controlling friction.

### 5.1.2. Introduction

Understanding and controlling friction is a long-standing, major topic in both research and application. The earliest approaches to controlling friction have focused on changing the sliding contact by modifying surface roughness or adding lubricants. More recently, atomic force microscope (AFM) methods have allowed basic studies of friction which intensively address how energy is dissipated at a sliding contact.<sup>[24,123–125]</sup> In addition to the atomic interactions in the contact interface, it has been found that phonon dissipation mechanisms,<sup>[79]</sup> conduction

electron excitation and drag,<sup>[17]</sup> and electrostatic forces<sup>[15,85,126]</sup> in the surrounding materials can significantly influence the friction between two bodies. This offers the intriguing possibility to change friction by varying material properties, without having to control the exact nature of the contact interface, which is strongly affected by operating conditions. Eventually, the goal is to bridge from the nanoscale contacts of AFM-based studies to macroscale contacts, which are composed of many interacting nanoscale contacts, with the hope of developing a physical basis for optimizing engineering friction.

Although our understanding of the basic mechanisms of energy dissipation at a sliding contact is surprisingly vague, there are two remarkable characteristics of friction which we now understand. The first is the century-old observation that the friction force  $F_F$  on a macroscopic object is proportional to the normal force  $F_N$  between the object and the surface on which it moves and not to the macroscopic contact area.<sup>[127]</sup> This at-first confusing observation seems to contradict the basics of classical mechanics, but was finally resolved by the understanding that the true contact area  $A$  between two objects is composed of many nano-asperities, and is much smaller than the apparent contact area; the true contact also increases roughly linearly with the normal force.<sup>[127,128]</sup> Since then, a number of studies have indeed confirmed that the friction forces at both single asperity nano-contacts and multi-asperity macro-contacts scale with the true contact area,<sup>[37,57,129–131]</sup> so that

$$F_F = \tau A \quad (5.1)$$

where  $\tau$  is a shear stress which is required to generate and propagate the excitations that allow sliding in the contact area.<sup>[132]</sup> It is conceptually analogous to the Peierls stress required for dislocation glide<sup>[73,133]</sup> but is expected to be smaller due to slightly increased interatomic distances due to incommensurability, defects, and the presence of (often amorphous) oxide and contamination layers.

The last several decades have shown great progress in using AFM to identify the excitations that are stimulated at nanoscale sliding contacts. It is widely observed in both experiment and theory that sliding contact does not proceed continuously, but by stick-slip events.<sup>[54,56,57,60,61]</sup> The stick-slip events are observed at all length scales, accounting for earthquakes<sup>[62]</sup> and atomic-scale instabilities,<sup>[56]</sup> as well as the acoustics of violins, squeaky doors, grasshoppers, and squealing brakes. With the exception of contacts containing only a few molecules, interface sliding should be envisioned as the motion of slip pulses through the contact interface, where the local slip velocity far exceeds the average slip velocity of the contact.<sup>[73]</sup> Even cases of apparent continuous sliding are often attributed to local slip pulses moving through the

interface.<sup>[134]</sup> Thus, the average AFM tip or scan velocity can be expressed as

$$v = A\rho v_{SP} \quad (5.2)$$

where  $A$  is the contact area,  $\rho$  is the areal density of active slip pulses (so that  $A\rho$  is the average number of active slip pulses in the contact), and  $v_{SP}$  is their average slip pulse velocity. This equation is analogous to Orowan's equation for the strain rate due to dislocation glide. A single slip pulse should be viewed as a localized slip wave that moves through the interface with an average slip pulse velocity  $v_{SP}$  and, once it traverses the contact area, causes a discrete sliding displacement of the tip. The forward slip distance of a slip pulse  $b$  can vary from meters for earthquakes to Angstroms for dislocations. In the case of a general incommensurate or disordered nanoscale contact,  $b$  is not conserved (in contrast to the case for dislocation Burgers vectors) and will vary from position to position within the contact by converting the slip displacement to local elastic strains. The AFM tip displacement due to slip pulse traversal will equal the average value of  $b$  along the contact area perimeter, and is thus not fixed at an interatomic distance or lattice spacing (or a multiple thereof). We note that not all 3D Molecular Dynamics simulations of atomic-scale sliding friction show evidence of slip pulse generation, which may be because of the high speeds often used in such studies.<sup>[135]</sup> Stick-slip behavior at the atomic scale,<sup>[80,136,137]</sup> through the mesoscale,<sup>[54]</sup> to the macroscale<sup>[60]</sup> has been successfully modeled using minimal 1D models such as the Prandtl–Tomlinson and Frenkel–Kontorova models. The remarkable success of these models lies in the fact that they can account for the strongly nonlinear dependence of friction on scan velocity, which is the second remarkable characteristic of friction. By describing the motion of an AFM tip as spring-loaded thermally activated motion over an energy barrier, a quantitative agreement has been obtained with scan velocity dependences, provided the ratio of barrier height to spring stiffness is high enough that an instability occurs.<sup>[64,65,67,70,136–138]</sup> In essence, the models are based on an Arrhenius-type law for the 1D average slip pulse velocity of the form<sup>[64,67]</sup>

$$v_{SP} = \omega_0 L \exp\left(\frac{-\Delta E}{k_B T}\right) \quad (5.3)$$

where  $\omega_0$  is an attempt frequency,  $L$  is a factor with units of length that depends on the contact stiffness of the experimental set-up and temperature,<sup>[64,67,138]</sup> and  $\Delta E$  is the activation energy barrier which must be overcome for a slip to occur. The basic assumptions that lead to this equation are that a slip event is critically damped, meaning that neither reverse slip jumps (overdamped) nor multiple jumps from inertial effects (underdamped) occur. There is evidence

from atomic stick-slip behavior to support this idea,<sup>[80]</sup> and near-critical behavior may, in fact, be an emergent property in sliding contact.<sup>[134,139]</sup>

Assuming that the activation barrier for slip  $\Delta E$  is reduced from the unloaded value  $E_0$  of the activation barrier by the force  $F_{SP}$  driving the slip event,<sup>[64,67,138]</sup> an equation for the friction force can be obtained that captures the basic features of the scan velocity dependence, namely that the friction force is finite in the limit of zero scan velocity and shows a weak dependence on scan velocity. A number of different approximations and validity ranges have been considered,<sup>[64,65,67,70,135–138]</sup> all leading to a logarithmic dependence of the friction force on the scan velocity. Using a linear approximation  $\Delta E = E_0 - bF_{SP}\pi^{-1}$  to describe the dependence of the activation barrier on the force acting on an individual slip pulse  $F_{SP}$ ,<sup>[64,138]</sup> one obtains an equation that can be used to approximately describe the dependence of the friction force on scan velocity,

$$F_F = F_{ph} = \frac{\pi A}{b^2 \omega} \left[ E_0 + k_B T \ln \frac{v}{v_0} \right] \quad (5.4)$$

In obtaining eq. 5.4, we have used eq. 5.1 to eq. 5.3, set  $v_0 = A\rho\omega_0 L$ , and related  $F_{SP}$  to the shear stress  $\tau$  in the contact interface as  $F_{SP} = \tau b\omega$  where  $b$  is the mean forward slip distance of the slip pulse. This quasi-1D model describes the average tip velocity as a result of slip pulses that span the entire width  $w$  of the contact. Note that the energy barrier  $E_0$  and shear stress  $\tau$  increase with the normal force,<sup>[67]</sup> analogous to the dependence of dislocation glide on normal force, so that the friction force  $F_F$  depends on the normal force  $F_N$  both through the contact area  $A$  and  $E_0$ .

Equations for thermally activated stick-slip behavior with forms similar to eq. 5.4 have been derived from the Prandtl–Tomlinson model and widely used in the literature to discuss the scan velocity dependence of friction.<sup>[64,65,67,70,136]</sup> The models are able to fit the data quite well, but surprisingly, predict that friction should only depend on surface structure (through  $E_0$ ,  $b$ , and  $\rho$ ) and contact area  $A$ , and not on the inherent dissipation rates in the surrounding materials.<sup>[80]</sup> In reality, it is clear that thermally activated jumps at surfaces couple directly to the macroscopic degrees of freedom of the underlying materials, as has been widely discussed within the context of adsorbate vibration relaxation.<sup>[140]</sup> The predicted independence from inherent dissipation within the Prandtl–Tomlinson model follows from the assumption of critical damping, which is supported by both experiment and simulation at the atomic scale.<sup>[80,139]</sup> In fact, thorough modeling of friction for a wide range of dissipation rates show that the friction force increases with the dissipation rate in both the underdamped and overdamped regimes, but is relatively constant in the critically damped regime,<sup>[137]</sup> in good agreement with Kramers

reaction rate theory.<sup>[141]</sup> The question of which regime best describes experimental data remains open.

In fact, a number of experimental studies show a clear dependence of friction on the surrounding material properties,<sup>[14–17,20,85,126,142,143]</sup> suggesting that it is time to move beyond the widely used critically damped Prandtl–Tomlinson model (e.g., eq. 5.3 and eq. 5.4), despite its impressive success in accounting for the scan velocity dependence of friction. The most compelling experimental studies for the effect of surrounding material properties have investigated friction across the superconducting transition. Despite relatively unchanged surface bonding and structure, a clear increase in friction on transitioning from the superconducting to the normal state has been observed in a variety of materials.<sup>[14,16,17,20]</sup> One explanation given for the behavior is based on viscous damping of the tip by electronic excitations: in the superconducting state, the electrons form Cooper pairs that exhibit an energy gap in their excitation spectrum, while in the normal state quasi-free electrons are easily excited and dissipate the sliding energy. An electronic friction force  $F_{el}$  is simply added to the total friction force as  $F_F = F_{ph} + F_{el}$ , where the phononic friction  $F_{ph}$  results from the slip pulse excitations described above in eq. 5.4. The electronic friction force  $F_{el} = -B_{el}v$  is assumed to represent damping by normal carriers near the Fermi energy through a viscous damping coefficient  $B_{el}$  as a result of electromagnetic or van der Waals interactions with the tip.<sup>[14,16,17]</sup> Although van der Waals interaction forces are believed to make significant contributions to the adhesion force,<sup>[144]</sup> theoretical values for the van der Waals friction based on generating electronic excitations near the Fermi energy and then dragging them behind the tip<sup>[123]</sup> (Coulomb drag) deliver forces that are much too small (on the order of  $10 \times 10^{-18}$  N for typical AFM measurement conditions) to account for the measured changes in the sliding friction force on the order of  $10 \times 10^{-10}$  N or larger.<sup>[14,16]</sup> On the other hand, there is good agreement with the much smaller forces measured in non-contact friction studies,<sup>[17]</sup> where presumably the slip pulse excitations described in eq. 5.4 are not active. This suggests that viscous electronic damping of van der Waals interactions with the tip is active and presumably contributes to sliding contact friction; it is simply completely overshadowed by the energy dissipated in the slip pulse excitations. This same problem with the order of magnitude of possible contributions from electronic excitations has been encountered when trying to explain the effect of doping and carrier density on the sliding friction of various semiconductors,<sup>[15,143]</sup> although it is conceivable that the local electric fields generated in these studies might be large enough to modify the near-surface electronic properties.

Since the energies required to generate electronic excitations through electrodynamic inter-

actions with the sliding tip or to drag image charges (Coulomb drag) are both too small to explain the observed correlation between material properties and contact sliding friction, the effect of electrostatic forces has also been considered.<sup>[14–16,85,143]</sup> Forces both parallel and perpendicular to the surface normal can be generated depending on the distribution of charges or dipoles in the contacting materials. Electrostatic normal forces have the effect of increasing  $A$  in eq. 5.1 described by elastic contact mechanics (e.g., Hertz contact theory), while net electrostatic forces parallel to the sample surface will directly add to the friction forces. In some cases, an order-of-magnitude agreement with the experiment has been achieved, but quite large and specific trapped charge densities have often been required to explain the measurements. For example, in order for electrostatic forces to contribute to the lateral forces felt by the tip, the “line of charges” left in the wake of the sliding tip must have lifetimes long enough to slow the advancing tip but short enough to have annihilated by the time the tip is rescanned along the same path.<sup>[15,85]</sup> Such highly specific scenarios have not yet been verified, although they would offer promising methods to control friction by tailoring electric fields.<sup>[145]</sup> In this paper, we investigate nanoscale single asperity sliding friction at the surface of lanthanum strontium manganite ( $\text{La}_{(1-x)}\text{Sr}_x\text{MnO}_3$ ) films ( $x = 0.2$  and  $0.3$ ) while heating through transitions from the FM to a PM state. The transitions in these films allow us to probe the effect of electronic and phononic degrees of freedom on friction without a change in the crystal structure. We use experimental conditions where the contact contains many atoms (ca. 100), rather than attempting single-atom contacts, in order to probe the behavior of typical nano-asperities that make up macroscopic contacts. We observe a clear increase in friction on crossing from the metallic to small polaron hopping conductivity state, which is due to the damping of the slip pulse excitations generated in the sliding contact. We argue that the strong increase in electron-phonon coupling at the transition causes a change in the lifetime of the slip pulses and can quantitatively account for the excess friction in the polaronic phase. This explanation is distinct from many previous explanations, which were based on van der Waals and ohmic losses and were unable to quantitatively account for the observed friction.

### 5.1.3. Results and Discussion

#### Friction and Adhesion Forces at the Phase Transition

$\text{LaSrMnO}_3$  films with  $x = 0.2$  and  $x = 0.3$  were chosen for the friction studies because they manifest temperature-driven transitions in electrical ( $T_{MM}$ ) and magnetic ( $T_C$ ) properties without changes in the bulk film crystal structure and in atomic bonding. At low temperatures, the films are FM with metallic conduction governed by the double exchange mechanism.

They become PM above the transition temperatures, with strongly increased electrical resistivity due to the transition to a small polaron conductor. The strong increase in electron-phonon coupling results in the localization of charge carriers at the Jahn–Teller distortions to form small polarons.<sup>[104,106,107,146,147]</sup> We note that the transition temperatures are dependent on the exact composition (including possible oxygen vacancies) and on stresses that result from the epitaxial relation with the substrate<sup>[148,149]</sup> and may be different at the surface of the films due to an observed reconstruction.<sup>[150]</sup> Often the two transitions overlap due to the coupling between spin, electron, and phonon degrees of freedom, but can also be shifted from each other.<sup>[104,106,107,146,147]</sup> In addition to allowing systematic tests of the effects of electronic, magnetic, and phononic degrees of freedom on friction, the manganite films offer potential technological application since it has recently been shown that resistive switching of manganite films offers a practical tactic for controlling friction without having to vary the temperature.<sup>[1]</sup> A 6 nm thick film of  $\text{La}_{0.7}\text{Sr}_{0.3}\text{MnO}_3$  ( $x = 0.3$  specimen) was fabricated on a buffered  $\text{SrTiO}_3$  substrate by metal-organic aerosol deposition,<sup>[151]</sup> with a FM-PM transition at  $T_C = 338$  K and a metal-like to hopping small polaron conductivity transition at  $T_{MM} = 330$  K. A 70 nm thick film of  $\text{La}_{0.8}\text{Sr}_{0.2}\text{MnO}_3$  ( $x = 0.2$  specimen) was fabricated on  $\text{SrTiO}_3$  by sputter deposition and exhibits a FM-PM transition at  $T_C = 220$  K and a metal-polaronic conductor transition at  $T_{MM} = 187$  K. The crystal structure is rhombohedral both above and below the transitions ( $R\bar{3}c$  space group) and strained due to the epitaxial relation with the underlying substrates.<sup>[148]</sup> Measurements to determine crystal structure, film thickness, magnetic properties, and resistivity are summarized in the SI for both films (see fig. S1–S10).

Nanoscale friction force measurements<sup>[53]</sup> were performed on heating through the transition temperature using AFM-based lateral force microscopy for a range of normal loads and scan speeds. The AFM studies were performed in a UHV environment in order to avoid complications from water condensation and other surface contamination. Details of the force calibration and scaling, as well as data analysis, are described in the section 5.1.5. The normal forces  $F_N$  between the conducting nanoscale Si tip and the film were kept below 30 nN to avoid detectable wear contributions. A typical friction loop for an applied normal force of 0.7 nN is shown in fig. 5.1a. Including the adhesion force (fig. 5.1e) gives an actual normal force of about 12 nN and a true contact area of about  $A = 5 \text{ nm}^2$ , according to elastic Hertz contact theory and using the nominal tip radius of 10 nm (see section 5.1.5 and fig. S11). According to eq. 5.1, the friction force then corresponds to an interface shear stress on the order of  $\tau = 2 \text{ GPa}$ , which is reasonable, roughly a factor of 5 smaller than the Peierls barrier in perovskite oxides.<sup>[152]</sup> A comparison of the friction force with topography (fig. 5.1a) shows that the approximately 10 % variations in the magnitude of the friction force during

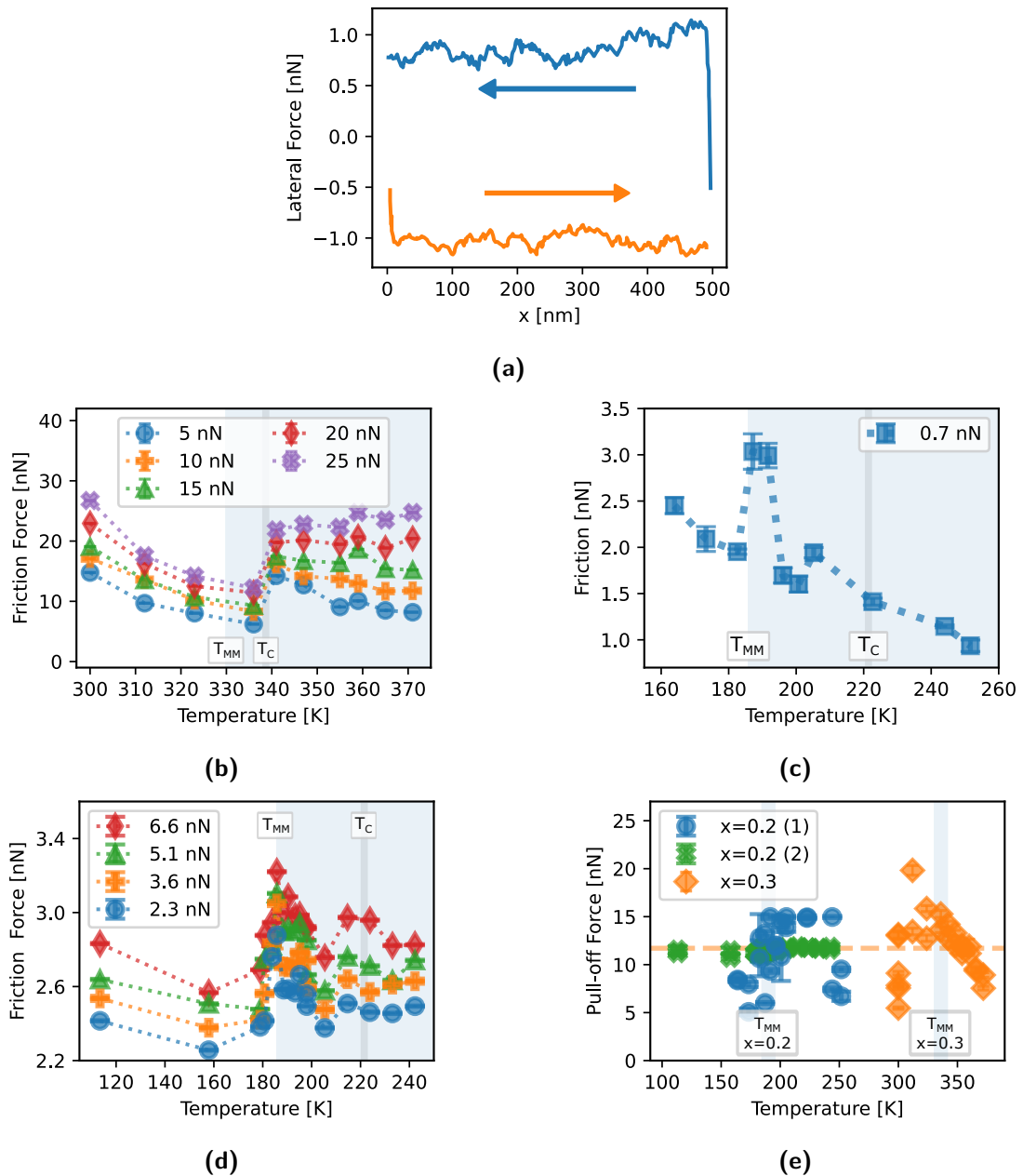


**Figure 5.1:** Friction and adhesion forces near the FM metal to PM polaronic conductor transition for  $x = 0.2$  and  $x = 0.3$   $\text{LaSrMnO}_3$  films. **(a)** Lateral friction force loop (solid lines) and topography (dotted lines) for the  $x = 0.2$  film obtained at an applied normal force of  $0.7 \text{ nN}$  and a scan velocity of  $2.5 \mu\text{m s}^{-1}$  showing a strong hysteresis and stick-slip activity. **(b)** Average friction forces for the  $x = 0.3$  film as a function of temperature for different applied normal forces at a scan velocity of  $2.5 \mu\text{m s}^{-1}$ . **(c,d)** Two measurement series with different cantilevers of average friction forces for the  $x = 0.2$  film as a function of temperature for different normal forces at a scan velocity of  $2.5 \mu\text{m s}^{-1}$ . **(e)** Adhesion forces estimated from pull-off force measurements for the  $x = 0.3$  and  $x = 0.2$  films. The error bars are given by the standard error; the number of friction scans used to determine average friction forces lies between 100 and 256 (see section 5.1.5).

the forward and backward traces do not correlate with topography (see also the section 5.1.5 and fig. S12, fig. S13). The variations in friction are attributed to slip pulses traversing the contact. To first approximation in the quasi-1D model used above, the average forward slip distance of the slip pulses can be estimated from the 10 % force variations in fig. 5.1a as  $b = 10 \% \cdot \sqrt{4A/\pi} = 0.25 \text{ nm}$ ,<sup>[53]</sup> which is a reasonable number in that it is comparable to an interatomic distance. Friction forces  $F_F$  were obtained for each normal load and temperature by averaging the magnitude of the forces for many friction loops (figs. 5.1b to 5.1d). The friction forces for both films show a gradual decrease with increasing temperature, followed by an abrupt increase at the transition from the metallic to polaronic conducting state. Note that the large temperature difference (35 K) in the electrical and magnetic transition temperatures in the  $x = 0.2$  film allows us to identify that the friction change is correlated with the onset of polaron formation and not with a change in magnetic order (figs. 5.1c and 5.1d). In contrast, the transitions for the  $x = 0.3$  films are too close (within 10 K) (fig. 5.1b) to distinguish which causes the friction change (see section 5.1.5 for a discussion of specimen temperature accuracy) so that we presume it is also here caused by the polaron formation. Depending on the normal force, the friction force then either falls again for low normal forces or stays at an elevated value for larger normal forces. Friction measurements recorded first and last in the temperature series were performed at the same temperature (room temperature for  $x = 0.3$  and 250 K for  $x = 0.2$ ) and show no significant difference relative to the error bars, so we assume no or only insignificant changes in the tip geometry or surface chemistry during the friction measurements.<sup>[53]</sup> Although the friction forces for the  $x = 0.2$  film are smaller than for the  $x = 0.3$  film (even for the same normal force), the fact that both films, with different compositions, different thicknesses, and different transition temperatures, both show the same behavior indicates that the correlation between the friction increase and the formation of small polarons is robust. We note that switching AFM tips while measuring a given specimen can easily lead to changes in the friction forces by a factor of four, presumably due to differences in the tip geometry.

The adhesive forces between the tip and LaSrMnO<sub>3</sub> films can be estimated by the pull-off forces that were obtained from force-distance measurements as a function of temperature. They are plotted in fig. 5.1e for both films and show no systematic trends with respect to the temperature or the order of measurement. In particular, values recorded at the same temperature and first and last in the temperature series give the same value of the adhesive force, confirming that there was no measurable change in the tip geometry. The adhesion energy can be estimated as  $0.09 \text{ J m}^{-2}$  using the Derjaguin, Muller, and Toporov contact model,<sup>[33]</sup> which is consistent with typical interface energies measured in AFM studies.<sup>[49]</sup> The lack of

an abrupt change in adhesion at the transition temperature rules out the possibility that the variations in friction are caused by changes in the contact area. This is consistent with the fact that the elastic modulus changes by less than 5 % at the transition temperature<sup>[153]</sup> and should lead to changes in the adhesion force on the order of 1 nN or less. Furthermore, the constant adhesion force confirms that the interatomic forces, van der Waals forces, and electrostatic forces due to Coulomb and capacitive interactions do not change significantly at the phase transition. Thus, the observed changes in friction at the transitions are due to a fundamental change in the ability of the near-surface regions of the films to dissipate energy.

### Friction Coefficient and Normal Force Dependence

The friction force is observed to increase linearly with the normal force at each temperature, with a non-zero intercept (fig. 5.2a). Even in the absence of an applied normal force ( $F_N = 0$ ), an attractive force between the tip and specimen leads to friction forces between 5 and 15 nN and to the consequence that friction forces may be larger than the normal forces (see also fig. 5.1a). The observed linear dependence of the friction force on the normal force is in agreement with a number of other nanoscale friction studies,<sup>[24,81,85,154,155]</sup> although contact mechanical considerations for a sphere pressed against a flat surface predict sublinear behavior, which is also often seen.<sup>[49,122]</sup> The widely observed linear behavior occurs for small adhesion energies<sup>[122,156]</sup> and may result from deviations from a spherical tip shape, from possible dependencies of  $\tau$  on the contact area size,<sup>[73]</sup> or simply from the combined effect of the normal force dependence of the contact area and the slip barrier (eq. 5.4). The approximate linear dependence allows the microscopic definition of the friction coefficient (slope of the  $F_F$  vs.  $F_N$  curve) to be used to characterize dissipation. The plot of the friction coefficient as a function of temperature (fig. 5.2b) shows two distinct trends. The friction coefficient gradually decreases with increasing temperature below the transition temperature and then abruptly increases at and above the transition temperature, eventually leading to more than a doubling in value. The gradual decrease in friction coefficient with increasing temperature is attributed to thermally activated stick-slip behavior.<sup>[14,70,122,136,137,157]</sup> This decrease is often successfully fit for small friction forces with an Arrhenius dependence  $F_F = F_0 \exp(-E_a/k_B T)$ , where  $E_a$  is assumed to be the rate-limiting activation barrier for the slip event.<sup>[69,80,81,157]</sup> The best fit to the data in the FM state gives an activation energy of  $E_a = 0.159(13)$  eV, which is similar to the activation energy values obtained in previous studies on a range of different materials.<sup>[81,85]</sup> Note that eq. 5.4 predicts a linear or power law decrease in the friction force with temperature ( $v < v_0$ ), which has also been widely applied in the literature.<sup>[14,65,67,157]</sup>

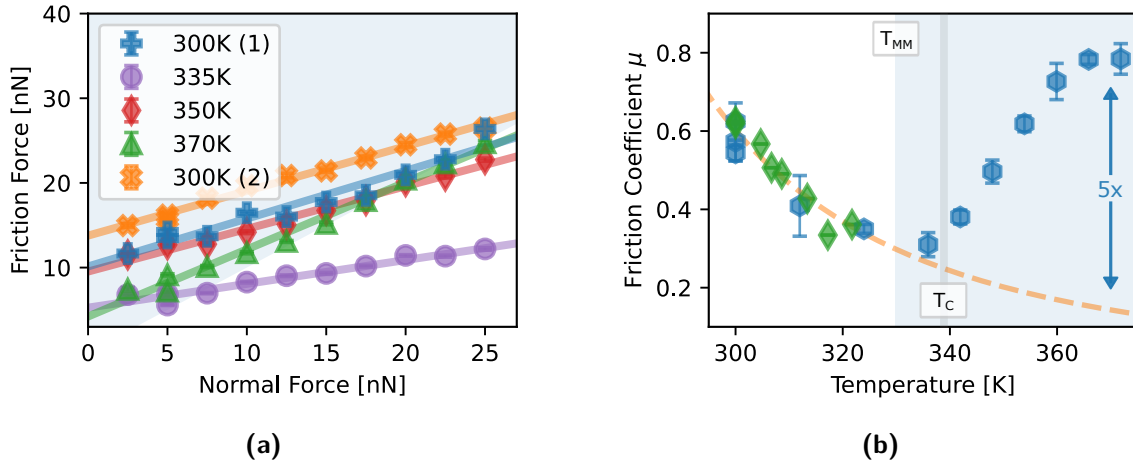


**Figure 5.2:** Friction of the  $x = 0.3$   $\text{LaSrMnO}_3$  film. **(a)** Friction forces show a linear dependence on the applied normal force for all temperatures both above and below the transition. **(b)** The friction coefficient obtained from two sets of measurements with different cantilevers (blue hexagons and green diamonds) from the slopes in **(a)** shows distinct behavior in the FM metal and PM polaronic conductor states. The dashed line shows a fit to the data with an Arrhenius dependence. The error bars are given by the standard error; the friction forces are averages of 256 measurements (see section 5.1.5).

### Scan Velocity Dependence of Friction

The friction forces were measured for both films as a function of scan velocity (fig. 5.3) and show a clear non-linear increase with velocity, both above and below the transition temperature (fig. 5.3b). The scan velocity dependence is well described by a logarithmic dependence, as expected from thermally activated stick-slip models. [64,65,67,138,157] Fits were made to the data using eq. 5.4 and setting  $E_0 = 0.159$  eV, [85] as obtained from the temperature dependence for the  $x = 0.3$  film. Otherwise, the fits are under-constrained and do not stably converge. We obtain values between 1 and  $3 \text{ nm s}^{-1}$  for  $v_0$ , in good agreement with the literature, [122] and values for  $b$  which increase with the temperature from 0.04 nm at 112 K to 0.14 nm at 300 K. These values are comparable to the values estimated from fig. 5.1a. The idea that the slip distance might increase with temperature seems reasonable, considering that the slip interface will include regions with low slip barriers which may be overcome by inertial processes.

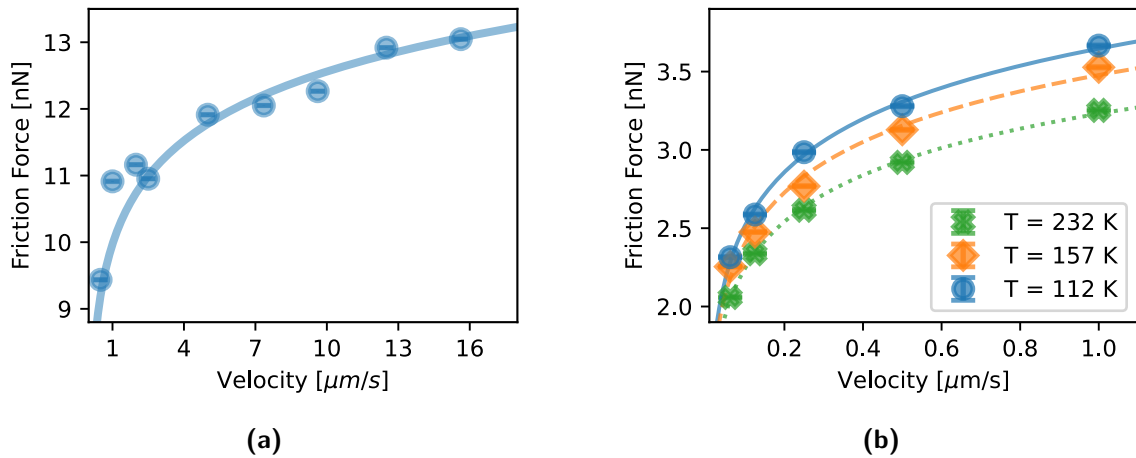


**Figure 5.3:** Friction forces as a function of scan velocity for the  $\text{LaSrMnO}_3$  films. **(a)** Friction force in the  $x = 0.3$  film for  $F_N = 5$  nN at room temperature in the FM state. **(b)** Friction force in the  $x = 0.2$  film for  $F_N = 2.3$  nN below, near, and above the transition temperature. The error bars are given by the standard error; the number of friction scans used to determine average friction forces lies between 100 and 256 (see section 5.1.5).

### Effect of Electrostatic Forces

Previous literature studies have proposed that electrostatic interactions between charges that are trapped near the specimen and tip surfaces might account for the observed dependence of friction on electronic properties.<sup>[14–16,85,143]</sup> For instance, the increase in friction at the insulator to the metal transition of  $\text{VO}_2$ ,<sup>[85,142]</sup> at the superconducting to normal transition of an oxide,<sup>[14,16]</sup> or as a result of changes in semiconductor doping,<sup>[15,143]</sup> have been discussed in terms of electrostatic forces resulting from charges or fields set up by the tip-specimen interactions. In some cases, the friction change has been accompanied by an adhesion change, lending quantitative support to the argument that electrostatic forces have increased the normal force and thereby increased the contact area.<sup>[15,85]</sup> In other cases, the required trapped charge densities are estimated, leading to reasonable numbers in the case of Si,<sup>[143]</sup> but requiring specific time-dependent distributions of charges in other cases.<sup>[15,85]</sup>

In our studies, the lack of a temperature-dependent adhesion force indicates that there are no significant differences between the Coulomb and capacitive interactions of the tip with the high and low-temperature manganite phases under the conditions used to measure pull-off forces. This means that contact electrification (the charges transferred between two materials when brought together and then taken apart) is not measurably different for the two phases. On the other hand, it is well-known that the charges generated at two contacting surfaces depend on their sliding speed (tribocharging),<sup>[18]</sup> so that the possibility must be explored whether

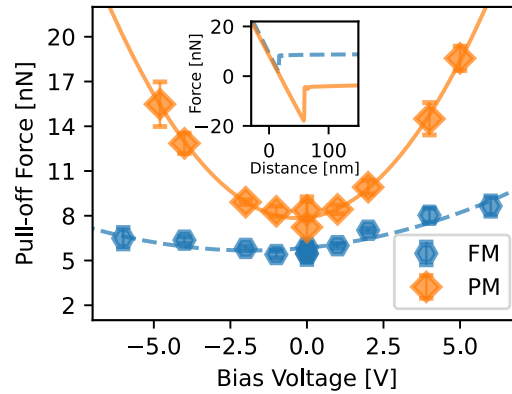


**Figure 5.4:** Pull-off forces for the  $x = 0.3$  film as a function of bias voltage in the ferromagnetic (FM) (300 K) and paramagnetic (PM) (380 K) states obtained from pull-off force measurements (see inset). The adhesion has a quadratic dependence on bias in both states (solid and dashed lines). The capacitance in the PM state is roughly 5 times larger than in the FM state. The contact potential difference between the AFM tip and specimen (given by the voltage at minimum adhesion) differs by approximately 2 V between the two states. The error bars are given by the standard error; the adhesion forces are each obtained from averages of 256 measurements.

tribocharging is very different in the two phases. This possibility can be indirectly ruled out by considering the tribo-current that would be necessary above the transition to account for the measured change in friction. In fig. 5.1b, we observe an increase in friction force of almost 10 nN at the transition. According to fig. 5.2a, this requires an increase in the normal force of about 20 nN. According to measurements of the pull-off force as a function of the applied bias voltage between the tip and the  $x = 0.3$  film (fig. 5.4), a bias voltage in excess of 6 V would be needed to produce electrostatic forces of 20 nN between the tip and the PM phase. Such a large voltage is sufficient to cause resistive switching of  $\text{La}_{(1-x)}\text{Sr}_x\text{MnO}_3$ .<sup>[158]</sup> Furthermore, conducting AFM measurements of the  $x = 0.3$  manganite film in both low and high-temperature phases (see fig. S14) show that currents of 100 nA would be generated by a bias voltage of 6 V. This would lead to a large current density of  $2 \times 10^{10} \text{ A m}^{-2}$  at the contact, easily sufficient to produce large temperature rises. The behavior shown in fig. 5.1 allows us to rule this out. We thus find no support for the idea that electrostatic forces due to contact potential differences, contact electrification, or tribocharging can explain the observed increase in friction at the phase transition.

### Excess Friction in the Small Polaron Hopping Conductivity State

The clear increase in friction at the transition from the metallic to polaronic state (figs. 5.1 and 5.2) in both the  $x = 0.2$  and  $x = 0.3$  films shows that the excess friction results from the properties of the polaronic state. The absence of a corresponding increase in adhesion at the transition reveals that contributions from changes in the interatomic bonding or in the contact at the transition are insignificant, so that the excess friction must result directly from changes in the inherent damping of the near surface region of the  $\text{LaSrMnO}_3$ . Further, the thermally activated behavior and the logarithmic scan velocity dependence of the friction coefficient point to control by stick-slip events in both the metallic and polaronic conducting states (fig. 5.3). Thus, the interaction of the tip with the sample generates the same stick-slip pulse excitations above and below the transition, but these slip pulses are damped more strongly in the PM phase due to their interactions with small polarons. The idea of adding a viscous dissipation channel due to interactions of the tip with electronic degrees of freedom, as has been considered in previous publications (e.g.,  $F_F = F_{ph} + F_{el} = (\mu_{ph} + \mu_{el})F_N$ )<sup>[14–16,85,143]</sup> is not relevant here. Furthermore, as has been noted previously, estimates of the magnitude of possible electronic contributions  $F_{el}$ , whether due to van der Waals interactions or to ohmic losses, are several orders of magnitude too small to explain the observed changes in sliding friction both in the literature<sup>[14–16,85,143]</sup> and in our study.

We suggest instead that the friction force can be expressed as  $F_F = \alpha_P F_M(T)$  where  $F_M(T)$  is the friction force needed to generate slip pulse excitations in the metallic state (e.g., the dashed line in fig. 5.2b) and  $\alpha_P$  is a slip pulse-polaron damping factor that reflects the strength of the slip pulse coupling to small polarons. The polarons that emerge around the transition temperature in  $\text{LaSrMnO}_3$  consist of  $e_g$ -electrons localized on dynamic Jahn–Teller distorted  $\text{Mn}^{3+}$ .<sup>[106,107,146–148]</sup> This transition is also reflected in the electrical resistivity (see fig. S4 and S9, which is governed by the double-exchange mechanism well below the transition, but increases on passing through the transition as the Jahn–Teller energy increases and electron-phonon coupling becomes stronger.<sup>[106,107,146–148]</sup> The resistivity increases further with temperature until the electron-phonon coupling is strong enough that hopping polaronic conduction sets in with an accompanying decrease in resistivity (see fig. S4 and S9).<sup>[106,107,147,148]</sup> In fact, the slip pulse-polaron damping factor defined above for the  $x = 0.3$  film scales very well with the electrical resistivity in the neighborhood of the transition temperature where small polarons begin to form (fig. 5.5). This provides support for the idea that the vibrational slip-pulse excitations couple strongly to the phonon degrees of freedom, and through them, to the electron degrees of freedom as a result of the strong electron-phonon coupling which emerges

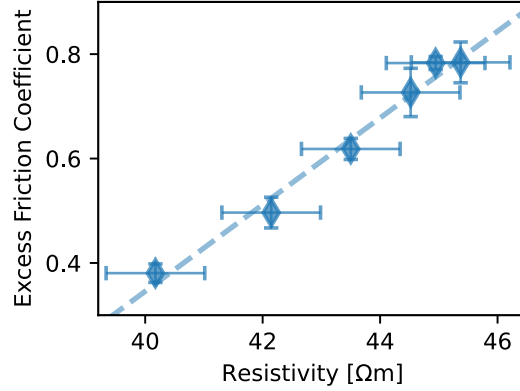


**Figure 5.5:** The slip pulse damping factor in the  $x = 0.3$  film polaronic state scales with the resistivity.

around the transition. Coupling to the magnetic degrees of freedom will also occur, but is expected to be weaker than the electron-phonon coupling effects in the temperature range investigated here;<sup>[54]</sup> furthermore, there is no evidence of an effect of the FM transition in our studies (fig. 5.2b). We are now faced with the question whether the coupling of slip-pulses to polarons can account for an increase by a factor of 5 in the slip pulse damping  $\alpha_P$  around the transition temperature (fig. 5.2b). The dominant phononic contribution to damping at the low velocities used for studying friction comes from the generation of sound waves,<sup>[123,133,159–161]</sup> as considered for the dissipation of absorbate vibrations.<sup>[123,162]</sup> It is argued that the rate of frictional energy dissipation is proportional to  $\omega^2$  or  $\omega^4$  depending on whether the phonons with mode frequency  $\omega$  are laterally coupled or oscillate independently, respectively.<sup>[140]</sup> In the case of  $x = 0.3$  material, a large change in the phonon spectrum is documented at the transition,<sup>[163,164]</sup> with the appearance of high wave number peaks associated with Jahn–Teller bond-stretching<sup>[163]</sup> above the transition temperature. Assuming a complete shift of the populated phonon states from Mn–O bond excitations at  $\hbar\omega \approx 47$  meV<sup>[165]</sup> below the transition temperature to the Jahn–Teller peaks at  $\hbar\omega \approx 62$  meV and  $\hbar\omega \approx 78$  meV above the transition,<sup>[162,165]</sup> would result in an increase in friction by factors between 1.8 and 7.5, which could account for the observed friction increase by a factor of almost 5. It remains to argue that the slip pulses couple strongly to the Jahn–Teller modes. This will depend on complex details of the slip pulse excitations and the interatomic potentials. One possible reason for a strong coupling will be discussed in the following section. Another is based on the fact that slip pulses at the surface of LaSrMnO<sub>3</sub> are not only vibrational excitations; due to the different interatomic bonding and valence states in LaSrMnO<sub>3</sub>, slip pulse motion will induce polarization and lead to dielectric excitations of the Mn–O octahedra and thereby to the Jahn–Teller modes.

### Slip Pulse Model for Friction with Explicit Damping Dependence

Given the success of the Prandtl–Tomlinson model in accounting for essential features of friction behavior, it is appealing to consider whether it can be extended to explicitly include damping of the slip pulse excitations. As already mentioned, most studies have focused on the critically damped regime of spring-driven Prandtl–Tomlinson models where there is no explicit dependence of friction on damping.<sup>[80]</sup> Critically damped behavior is supported by atomic stick-slip experiments which rarely show evidence of barrier re-crossing (overdamping) or inertial multi-slip (underdamping).<sup>[80]</sup> Furthermore, a recent simulation study<sup>[139]</sup> argues that phonon “dephasing”<sup>[162]</sup> in reaction to an atomic stick-slip event will lead to emergent critically damped behavior. Which damping regime is relevant depends on the ratio of the inherent dissipation rate in the material  $\eta$  to the local undamped contact resonance frequency  $\sqrt{k/m}$ , where  $k$  is the contact stiffness and  $m$  is an effective mass of the asperity. Critical damping occurs when the two rates are approximately equal, while underdamping and overdamping occur for smaller and larger inherent dissipation rates, respectively. A careful numerical study of the effect of damping on thermally activated stick-slip behavior shows that the friction force increases steeply with the dissipation rate in both the underdamped and overdamped regimes, and is relatively constant in the critically damped regime.<sup>[137]</sup> Since local contact stiffnesses and effective masses depend on local atomic structure and normal stresses, all three damping behaviors may be simultaneously manifested in a general, incommensurate, nanoscale contact and an explicit dependence on the dissipation rate may be expected.

In this paper, we take a heuristic approach using guidance from the theory of dislocation glide to develop a model for nanoscale friction which explicitly includes inherent material dissipation.<sup>[73,133]</sup> In comparison with previously discussed scenarios, we take advantage of the 2D nature of the contact interface and the fact that the dynamic atomic-level processes for slip pulse motion may be different, parallel, and perpendicular to the slip direction, just as the motion of dislocation is governed by overcoming the Peierls barrier to form a kink pair and then by the lateral motion of the kinks. The equation we obtain provides a framework to explain our observations, but we have not attempted a fully quantitative approach and do not claim the model is unique in being able to motivate our findings. However, the equation is successful in explaining the observed dependence of friction on the phase transition as well as on the temperature and scan velocity. Effectively, our equation describes underdamped Prandtl–Tomlinson behavior where the size of the slip step is controlled by viscously damped kink motion.

The well-studied example of dislocation glide in crystals provides a helpful analogy for un-

understanding the atomic mechanisms and role of damping in the motion of a slip pulse. The essential feature is that dislocation glide is controlled by two distinct mechanisms: initiation of glide by kink pair nucleation, followed by lateral motion of the kinks (perpendicular to the slip direction) apart from each other. Even if it is clear that the topological constraints on dislocation structure, glide, and kink motion do not apply to slip pulses in an incommensurate interface between two dissimilar materials, it is also clear that the 2D nature of the contact interface requires mechanisms for propagation both parallel and perpendicular to the slip direction. For a disordered interface with large local variations in slip barriers, one might expect that slip pulses may disappear after propagating only a short distance along and perpendicular to the slip direction. In the limit that these distances are atomic distances, the resultant atomic stick-slip behavior provides the upper limit for the friction force at a fixed scan velocity.<sup>[73]</sup> However, atomic stick-slip is unlikely to be a major contributor to a general frictional contact, so that dislocation glide models based on non-adiabatic creation of kink pairs followed by viscously damped lateral motion of the kinks, may capture the essentials of slip pulse motion at a sliding interface. The unloaded activation energy barriers for slip at an incommensurate interface between two dissimilar materials that are not chemically bonded ( $E_0$  in eq. 5.4) are presumably quite a bit smaller than the Peierls barriers in single-crystalline materials. Thus, given the large shear stresses acting on a slip pulse (here,  $\tau \approx 2$  GPa), it is reasonable to assume that only forward-moving kink pairs are generated in the sliding contact and that the large shear stress relative to the barrier height entirely hinders backward moving kink pairs. This is the same condition described by the critically damped 1D Prandtl–Tomlinson model for friction. Once a forward moving kink pair is nucleated, the large shear stresses in the interface will sweep the kinks laterally apart. Just as for dislocations, the barrier for lateral kink motion in a slip pulse is smaller than for kink nucleation. Therefore, we assume that kink velocity is controlled by drag,  $v_k = \tau b w_k B_K^{-1}$ , where  $v_k$  is the kink pair separation velocity,  $\tau$  is the shear stress acting on the kinks (assumed for simplicity to be the same as that driving kink pair nucleation),  $w_k$  is the lateral distance swept out by the kink pair, and  $B_K = \eta_k m$  is a kink pair viscous damping coefficient that is dependent on  $T$ .<sup>[166,167]</sup> The kink pair dissipation rate  $\eta_k$  is the inverse of a kink pair lifetime. This then allows us to express the scan velocity as the product of the rate of kink pair generation in the contact  $A\rho \exp(-\Delta E/k_B T)$ , the kink pair velocity  $v_k$ , and a factor  $\alpha'$  describing the contribution of each kink pair to forward sliding,<sup>[166,168]</sup>

$$v = \alpha' v_k A \rho \exp\left(\frac{-E_0 + F_F \Omega_{kp} / \pi A}{k_B T}\right) = \frac{\beta F_R}{B_K} \exp\left(\frac{-E_0 + F_F \Omega_{kp} / \pi A}{k_B T}\right) \quad (5.5)$$

where we have used eq. 5.1 to eq. 5.3 and replaced  $b^2w$  in the 1D expression for  $\Delta E$  (eq. 5.4) with the volume  $\Omega_{kp}$  of the kink pair nucleus. Furthermore, we have defined  $\beta = \alpha'bw_k\rho$ , which is a geometrical measure of the contribution of all kink pairs to forward sliding.<sup>[166]</sup> This equation has a similar form to eq. 5.3, but with the essential difference that the scan velocity pre-factor has now been replaced with a term proportional to the friction force and inversely proportional to a damping coefficient in the material. Just as for the Prandtl-Tomlinson model, this equation describes the generation of stick-slip events by non-adiabatic thermal activation of kink pairs, but in this case, the contribution of each slip pulse to the scan velocity is determined by the viscously damped motion of the kink pairs in the interface.

Equation 5.5 gives fits to the scan velocity dependence of the friction force (fig. 5.3) that are indistinguishable from those of eq. 5.4, but the interpretation of the fitting parameters is different. In contrast to the temperature dependence of  $b$  obtained from fitting with eq. 5.4, the value of  $\Omega_{kp}$  from the fit with eq. 5.5 is roughly temperature-independent, which seems physically reasonable. Meanwhile,  $b$  increases by a factor of around 4 as the temperature increases from 112 to 232 K, consistent with the idea that the damping increases in the polaronic phase by the same factor as the friction. Except at low temperatures, the dominant dislocation drag effects are due to the phonon subsystem which generally behaves viscously.<sup>[133,167]</sup> The largest phonon loss contribution at low dislocation glide velocities is due to the generation of sound waves (phonon radiation friction), and has been estimated for the case of kinks moving along straight dislocations.<sup>[167]</sup> According to phonon coupling, a kink of width  $D$  will couple most strongly into phonons with wavelengths  $\gtrsim 2D$ .<sup>[167]</sup> Since the barrier to kink motion is assumed to be small,  $D$  will be larger than the atomic spacing, so that the main coupling to the Jahn–Teller modes of the Mn–O octahedral occurs via an electron-phonon coupling.

We note that in addition to the explicit appearance of a viscous damping coefficient in eq. 5.5, there is also a dependence on the friction force  $F_F$  in the pre-factor. This gives the velocity equation features of both strongly driven systems (seen as a reduction of activation barrier by the friction force) and a weakly driven system (linear dependence on the driving force). Both the linear and exponential dependence of the scan velocity  $v$  on the friction force  $F_F$  result in a range of possible behaviors. At constant temperature, the scan velocity is more sensitive to changes in the friction force through the exponential term than through the linear term, explaining the observed logarithmic dependence of the friction force on scan velocity (fig. 5.3).

### 5.1.4. Conclusion

We report a clear increase in friction of two different  $\text{LaSrMnO}_3$  films that correlates with the formation of Jahn–Teller distortions and small polarons. We are able to reproduce the temperature and scan velocity dependence of the friction and provide an order of magnitude justification based on the picture that the slip pulses generated in the sliding interface are damped by coupling to the phonon bath. In the case of the  $\text{LaSrMnO}_3$ , this coupling increases at the transition temperature due to the emergence of small polarons in the near-surface region of the material. We believe this model, which combines the widely accepted stick-slip behavior at sliding contacts with concepts for damping of moving dislocations, provides a solid basis for interpreting nanoscale friction, also in other materials. We emphasize that our interpretation of the frictional dissipation mechanism is distinct from other studies where viscous electronic damping of the tip motion has been discussed but also recognized as much too small to account for the observed effects. Future studies may take advantage of tailoring phonon degrees of freedom in materials to better understand the damping of slip-pulses, as well as to develop tactics to control friction. In this respect, 2D layered materials are particularly promising, since they offer a number of tactics for phonon engineering.<sup>[169]</sup>

### 5.1.5. Experimental Section

#### $\text{La}_{(1-x)}\text{Sr}_x\text{MnO}_3$ Films

The  $x = 0.3$  film ( $\text{La}_{0.7}\text{Sr}_{0.3}\text{MnO}_3$ ) was deposited on a (001)  $\text{SrTiO}_3$  substrate with a  $\text{La}_{0.4}\text{Sr}_{0.6}\text{MnO}_3$  buffer layer using the metal-aerosol deposition technique.<sup>[113]</sup>  $\Theta - 2\Theta$  X-ray diffraction experiments (XRD) showed no indications of any impurity phase and confirmed highly oriented growth on the substrate (see fig. S1). Small-angle X-ray scattering gave thicknesses of 5.8(2) nm and 5.4(2) nm for the  $x = 0.3$  film and buffer layer, respectively (see fig. S2). The  $x = 0.3$  film undergoes the typical second-order phase transition from an FM metal to PM metal which was accompanied by a change in the sheet film resistance with increasing temperature, which is characteristic for the formation of Jahn–Teller polarons.<sup>[104,106,107,146,147]</sup> The transition was characterized using SQUID magnetometry (see fig. S3) and four-point sheet resistance measurements (see fig. S4). The metal-metal transition temperature extracted from the resistivity data was  $T_{MM} = \max(\rho^{-1}d\rho/dT) = 330$  K and the Curie temperature extracted from the magnetometry data was  $T_C = \max(d\mu/dT) = 338$  K. According to the phase diagram,<sup>[89]</sup> this transition occurred in the 5.8 nm thick  $\text{La}_{0.7}\text{Sr}_{0.3}\text{MnO}_3$  layer, while the buried  $\text{La}_{0.4}\text{Sr}_{0.6}\text{MnO}_3$  buffer layer remained a PM-metal above room tem-

perature and at all temperatures probed in this study. The specimen has an RMS-roughness of approximately 0.7 nm (see fig. S5), extracted from  $500 \times 500 \text{ nm}^2$  AFM topography scans, which did not change as the temperature was cycled.

The  $x = 0.2$  film ( $\text{La}_{0.8}\text{Sr}_{0.2}\text{MnO}_3$ ) was deposited on a (001)  $\text{SrTiO}_3$  substrate by sputter deposition.<sup>[149]</sup>  $\theta$ - $2\theta$  x-ray diffraction (XRD) showed no indications of any impurity phases and confirmed highly oriented growth on the substrate (see fig. S6). The film thickness of 70 nm was determined by x-ray reflectivity (XRR) (see fig. S7). The film undergoes a phase transition from an FM metal to PM metal which was characterized using SQUID magnetometry giving a Curie temperature at  $T_C = \max(d\mu/dT) = 222 \text{ K}$  (see fig. S8). The resistance measurement associated with the phase transition was characterized using a temperature-dependent four-point measurement (see fig. S9). This yielded a transition from the metal to polaronic state at  $T_{MM} = \max(\rho^{-1}d\rho/dT) = 186.8 \text{ K}$ . By tuning the deposition temperature and optimizing deposition parameters, the transition temperature was reduced by more than 100 K compared to the phase diagram,<sup>[89]</sup> presumably due to stresses from the epitaxial relation with the substrate and from sputter preparation-induced point defects.<sup>[149]</sup> The film showed an RMS-roughness of less than 0.2 nm, extracted from  $500 \times 500 \text{ nm}^2$  AFM topography scans (see fig. S10).

### AFM Measurements

AFM experiments were performed with a commercial Omicron VT-AFM/STM in a vacuum chamber at a base pressure of  $p = 10 \times 10^{-10} \text{ mbar}$ . The  $\text{La}_{0.7}\text{Sr}_{0.3}\text{MnO}_3$  film ( $x = 0.3$ ) was radiatively heated from the back, and the sample surface temperature was directly calibrated before experiments were performed. For measurements on  $\text{La}_{0.8}\text{Sr}_{0.2}\text{MnO}_3$  ( $x = 0.2$ ), the sample was clamped to a cryogenic stage whose temperature was controlled by adjusting the heating power of a resistor integrated into the stage and the liquid nitrogen flow. The surface temperature of the specimen was expected to be around 20 K warmer than the stage due to the poor thermal contact between the stage and the lightly clamped specimen.

Commercially available rectangular, single crystalline silicon cantilevers (Nanosensors PPP-CONTSCR) with a nominal tip radius of less than 10 nm were used (although a scanning electron microscopy (SEM) image, fig. S11, suggests an actual radius of 21 nm). The normal  $k_n$  and torsional  $k_t$  cantilever spring constants used for the  $x = 0.3$  measurements were obtained from the manufacturer values for the median cantilever dimensions and literature values for elastic constants ( $k_n = 0.52 \text{ N m}^{-1}$  and  $k_t = 42.74 \text{ N m}^{-1}$ ), while the normal and lateral forces were calibrated using the procedures described in the literature.<sup>[170–173]</sup>

The  $\text{La}_{0.8}\text{Sr}_{0.2}\text{MnO}_3$  specimen ( $x = 0.2$ ) was measured with an un-calibrated, pre-mounted cantilever of the same type as for the  $x = 0.3$  film. Estimates of the spring constants were obtained by assuming the average pull-off forces are the same for the  $x = 0.2$  and  $x = 0.3$  specimens (fig. 5.1e), leading to normal spring constants of  $k_n = 0.03$  and  $0.02 \text{ N m}^{-1}$  for the first and second  $x = 0.2$  measurements, respectively. These values are lower than for the  $x = 0.3$  cantilevers, presumably due to variations in cantilever dimensions, but are still within the manufacturer specifications. Assuming they result from a decreased cantilever thickness, values for the torsional spring constants were obtained for the cantilevers used in the first and second measurements of the  $x = 0.2$  film of  $k_t = 15.02 \text{ N m}^{-1}$  and  $k_t = 9.87 \text{ N m}^{-1}$ , respectively.

Nanoscale friction measurements were performed using AFM-based lateral force microscopy.<sup>[53]</sup> The lateral forces during sliding at a constant scan velocity and under a constant applied normal force were obtained from the measured torsion of the cantilever. By measuring the torsion during friction loops (trace and retrace scanning along the same line on the film surface, fig. 5.1a), the effects of topography were largely separated out from friction effects.<sup>[53]</sup> The friction forces  $F_F$  were obtained by averaging 100 or 256 friction loops that were performed in  $100 \times 100 \text{ nm}^2$  or  $500 \times 500 \text{ nm}^2$  regions on the surface of the specimens for each normal load and temperature of interest. To minimize wear during the friction experiments, the applied normal forces  $F_N$  were kept below 30 nN and any possible changes in the contact were monitored through tip-sample adhesion measurements. Adhesion forces were obtained by recording 100 force-distance curves before and after probing the frictional properties at each temperature and determined by averaging the extracted pull-off forces.

### Statistical Analysis

The friction and adhesion data were obtained in three independent sets of experiments on two different  $\text{LaSrMnO}_3$  thin film samples. To eliminate contributions from the specific film deposition method, two different deposition methods were used: sputter deposition for the  $x = 0.2$  film and metal-aerosol deposition<sup>[113]</sup> for the  $x = 0.3$  film. The large difference in the transition temperatures of the two films allowed experiments to be performed in very different temperature ranges and to rule out possible thermal artifacts. To rule out effects from tip wear, the first, and last measurements in a given series were performed at the same temperature.

The data evaluation was performed with user-written Python and MATLAB scripts. Each friction force or adhesion force data point represents the mean value of 100 ( $x = 0.2$  film) or

256 ( $x = 0.3$  film) individual friction loops or pull-off measurements, while the displayed error is the standard error.

Correlations between the friction forces and surface height, height gradient, and surface curvature were ruled out on the basis of the Spearman  $r_S$  coefficients ( $-0.11 \leq r_S \leq 0.1$ ) (see fig. S12 and S13).

### 5.1.6. Acknowledgements

This work was funded by the Deutsche Forschungsgemeinschaft (DFG, German Research Foundation) 217133147/SFB 1073, project A01 and project C02. The authors thank P. Ksoll and D. Schwarzbach for providing four-point measurements to characterize the phase transition in  $\text{La}_{0.8}\text{Sr}_{0.2}\text{MnO}_3$ . Furthermore, the authors thank O. Gordon for providing a Python interface<sup>[174]</sup> to perform partially automated measurements, and R.L.C. Vink, S. Merten, T. Brede, and F. Schönwald for discussions of the results, and A. Wodtke for allowing to use the vacuum AFM system.

## 5.2. Nanoscale Friction Controlled by Top Layer Thickness in $[\text{LaMnO}_3]_m/[\text{SrMnO}_3]_n$ Superlattices

The following section was submitted as “*Nanoscale friction controlled by top layer thickness in  $[\text{LaMnO}_3]_m/[\text{SrMnO}_3]_n$  superlattices*” in October 2022 to a peer-reviewed journal. The latest version of the manuscript can be accessed via [ArXiv:2210.09677](https://arxiv.org/abs/2210.09677). The manuscript was submitted by Niklas A. Weber<sup>1\*</sup>, Miru Lee<sup>2</sup>, Florian Schönewald<sup>1</sup>, Vasily Moshneaga<sup>3</sup>, Matthias Krüger<sup>2</sup>, Cynthia A. Volkert<sup>1</sup>. The corresponding supporting information (SI) are included as appendix A, the citations and the formatting are adapted to the rest of this thesis.

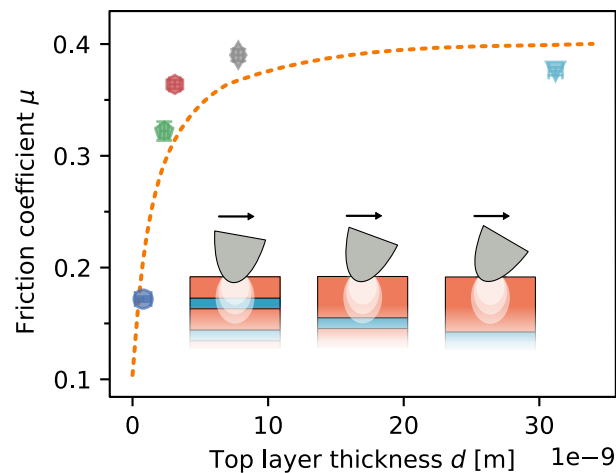
<sup>1</sup> *Institute of Materials Physics, University of Göttingen, Göttingen, 37077 Germany*

<sup>2</sup> *Institute for Theoretical Physics, University of Göttingen, Göttingen, 37077 Germany*

<sup>3</sup> *1st Physics Institute, University of Göttingen, Göttingen, 37077 Germany*

### Contributions:

Cynthia A. Volkert conceived and supervised the project. Niklas Weber performed all friction experiments on the  $[\text{LaMnO}_3]_m/[\text{SrMnO}_3]_n$  thin film samples and analyzed the data for all experiments shown. Florian Schönewald performed and evaluated the x-ray photoelectron spectroscopy (XPS)-measurements. Leonard Schüler prepared and pre-characterized the seven  $[\text{LaMnO}_3]_m/[\text{SrMnO}_3]_n$  superlattice thin films studied. Vasily Moshneaga supervised the preparation and characterization of the samples and contributed to the design of the experiments. Miru Lee and Matthias Krüger contributed to the theoretical interpretation of the results. All authors contributed to the writing of the manuscript.



### 5.2.1. Abstract

We conducted lateral force microscopy measurements on seven  $[\text{LaMnO}_3]_m/[\text{SrMnO}_3]_n$  superlattices with varied layer thicknesses. We observe that the friction forces and the friction coefficients initially increase with increasing  $\text{LaMnO}_3$  top layer thickness, followed by saturation when the top layer thickness exceeds a few nanometers. These observations clearly demonstrate that sliding friction is affected by sub-surface material properties to a depth of several nanometers and is not just determined by dynamics in the contact interface. We argue that the sub-surface dissipated energy is governed by damping in the elastically strained volume below the AFM tip, an effect which we estimate via thermoelasticity. The absence of a correlation between friction and the thermal resistivity of our superlattices shows furthermore that high-frequency phonons and heat conduction do not play a role in determining friction. Our observations thus demonstrate that friction can be tailored by sub-surface material properties.

### 5.2.2. Introduction

During the relative motion of two bodies in contact, kinetic and mechanical energy is converted into heat. This energy dissipation process is called friction and understanding its origins has been a long-standing issue in research, technology, and society. One of the main challenges of the last centuries has been that friction could only be studied on macroscopic scales, which kept the underlying dissipation mechanisms hidden for a long time. The emergence of atomic force microscopy (AFM) in the 1980s<sup>[118]</sup> facilitated the study of friction at the single nanoasperity level.<sup>[1,2,14–17,19,85,145,175–178]</sup> In the case of nanoscale low-wear, dry sliding friction, two mechanisms have been predominantly discussed: 1. frictional losses due to phonon excitation by mechanical interactions between the tip and surface, and 2. dissipative interactions linked to the electron system. To unravel the different contributions to sliding friction, several literature studies have so far systematically varied temperature,<sup>[2,14,16,17]</sup> contact pressure<sup>[85]</sup> or bias voltages<sup>[1,15,19,145]</sup> to alter the electronic and electrostatic interactions between the tip and the samples.

In our recent experimental studies on manganite thin films<sup>[1,2]</sup> we found evidence that electronic and electrostatic interactions are not sufficient to account for the observed changes in friction. Instead, it could be shown that phononic and vibrational contributions are the dominant factor contributing to energy dissipation at a nanoscale sliding contact. However, it remained hidden which phonon modes and wavelengths dominate dissipation and to what depth beneath the surface the material properties influence friction. These findings motivated the studies presented here, of nanoscale friction measurements on  $[\text{LaMnO}_3]_m/[\text{SrMnO}_3]_n$  su-

perlattices.

The question of how material properties below the surface affect friction has received considerable attention.<sup>[3,175–177,179–186]</sup> Friction measurements on layered materials, such as graphene, MoS<sub>2</sub>, NbSe<sub>2</sub>, WS<sub>2</sub>, WSe<sub>2</sub> and h-BN report a decrease in friction with an increase in layer count.<sup>[176,177,179]</sup> To explain these observations, several mechanisms have been proposed<sup>[3,179–181,185]</sup> that are related to the so-called puckering effect, which only is expected in materials with weak interlayer forces, and changes in the elastic properties. At the same time, studies<sup>[176,179]</sup> shows that the measured frictional forces approach a bulk value for increasing layer numbers, but do not specify the parameters that determine the length scale at which saturation occurs. In this regard, a viscoelastic model developed by Lee et al.,<sup>[3]</sup> which attributes top layer thickness dependent friction to viscous dissipation inside the evanescent waves excited in the top layer by a vibrating tip provides a possible explanation. In their study, the authors relate the saturation length to the decay length of such evanescent waves.

In this manuscript, we present AFM friction measurements on seven [LaMnO<sub>3</sub>]<sub>m</sub>/[SrMnO<sub>3</sub>]<sub>n</sub> superlattice films, with varying layer thicknesses in the range of  $m = 2$  to 80 atomic layers (or 0.8 to 32 nm). Our main finding is an increase in friction with the top layer thickness, which saturates after the layer thickness exceeds a few nanometers. We further observe no correlation between friction and the thermal properties of our films.<sup>[117,187]</sup> This enables us to rule out thermal conductivity, and thus high-frequency phonons, as the dominant contribution to friction in our systems. From the observed thickness dependence of the friction coefficients, we develop a model connecting friction to the energy losses occurring in the stressed volume near the contact interface through thermoelastic damping. Our model provides a possible explanation for the dependence of friction on the surrounding material properties and is consistent with the observed linear correlation between friction and normal force. We thus propose that friction can be actively controlled through tailored material selection, such as the thermal expansion coefficient, which consequently opens new possibilities for control of friction.

### 5.2.3. Materials and Methods

Six epitaxial superlattice films of [LaMnO<sub>3</sub>]<sub>m</sub>/[SrMnO<sub>3</sub>]<sub>n</sub>, where  $m$  refers to the number of LaMnO<sub>3</sub> unit cell layers, and  $n$  to the number of SrMnO<sub>3</sub> unit cell layers, were grown using metalorganic aerosol deposition (MAD) technique.<sup>[113]</sup> An overview of the  $m$  to  $n$  ratio of the films studied here can be found in table 5.1. Each superlattice stack was terminated with a layer of [LaMnO<sub>3</sub>]<sub>m</sub> to ensure equivalent chemical composition on the surface. The layer thicknesses and periodicity were monitored during deposition using in-situ ellipsometry measurements (see

appendix A.1.1). The total superlattice film thicknesses were kept constant at around 30 nm. Additionally, a single layer  $m = 80$  thick  $[\text{LaMnO}_3]_{80}$  film was prepared using the same technique. All films were deposited on  $5 \times 5 \times 0.5 \text{ nm}^3$  (100)-oriented  $\text{SrTiO}_3$ : 1.0 at. % Nb  $K \leq 0.5^\circ$  substrates.

The films were characterized after deposition using standard x-ray methods including XRD, XRR, and x-ray photoelectron spectroscopy (XPS) measurements. Additionally, the magnetic properties of the films were characterized by temperature dependent measurements of the magnetic moment (SQUID).

XRD measurements show Kiessig fringes<sup>[188]</sup> near the substrate peak, and no reflexes related to impurities (see appendix A.1.2). XRR measurements show the superlattice reflections and have intensities consistent with an interface roughness of  $RMS \leq 0.6 \text{ nm}$  for all films (see appendix A.1.3). XPS measurements have been performed on all samples using a Kratos Axis Supra spectrometer to investigate the chemical compositions of the near surface regions (see appendix A.1.4).

Thermal resistivities  $1/\kappa$  of the films studied here were estimated by using measurements made previously on films deposited with the same protocols and in the same deposition chamber.<sup>[117]</sup> Specifically, the thermal resistance  $1/\kappa$  of various  $[\text{LaMnO}_3]_m/[\text{SrMnO}_3]_n$  films, including films with the same  $m$  and  $n$  ratios as those shown here, were obtained using optical transient thermal reflectivity measurements and exhibit a linear dependence on the interface density. The linear relation was used to estimate the thermal resistivity  $1/\kappa$  of the films used here and are listed in table 5.1 (see appendix A.1.5). The validity of this comparison was additionally supported by SQUID measurements (see appendix A.1.6), that revealed magnetic properties of the films studied here in good agreement to those in earlier work.<sup>[117,187]</sup>

### AFM Measurements

AFM measurements were performed at room temperature ( $T = 293 \text{ K}$ ) under UHV ( $p \approx 2 \times 10^{-10} \text{ mbar}$ ) conditions using an Omicron VT-AFM/STM. For lateral force microscopy measurements, standard rectangular, single crystalline silicon cantilevers (*NANOSEN-SORS<sup>TM</sup> PPP-LFMR*<sup>[120]</sup>) with a nominal tip radius  $r \leq 10 \text{ nm}$  were used. The cantilevers exhibit normal spring constants  $k_N$  ranging from 0.88 to  $1.3 \text{ N m}^{-1}$  and lateral spring constants  $k_T$  ranging from 132.3 to  $177.4 \text{ N m}^{-1}$ . The latter were calculated based on geometric properties provided by the manufacturer and material parameters from literature.<sup>[190]</sup> Normal spring constants were measured using the so called *Sader method*<sup>[191,192]</sup> which is based on a known cantilever geometry and measuring the quality factor of the oscillation resonance. A

m [3.9 Å]	m [3.9 Å]	Film thickness [nm]	Thermal resistivity $\kappa^{-1}$ [mK W <sup>-1</sup> ]
2	2	32	0.91(2)
4	2	34	3.27(7)
6	6	32	0.43(2)
8	4	31	1.84(7)
14	7	32	1.23(7)
20	10	35	0.99(7)
80	0	32	0.77(7)

**Table 5.1:** Layer thicknesses and thermal resistivity values<sup>[117]</sup> of the seven superlattices studied. Individual thicknesses of layers  $m$  and  $n$  were obtained from XRR measurements.<sup>[189]</sup> Thermal resistivity values were approximated from thermal transient reflectivity measurements (see appendix A.1.5).<sup>[117]</sup> Depending on the  $m/n$  ratio,  $\text{LaMnO}_3$  is either cubic ( $m/n = 1$ ) or a rhombohedral ( $m/n = 2$ ).

representative SEM-image of an AFM cantilever and tip can be found in section 4.1.2.

Friction measurements were performed using lateral force microscopy measurements, whereby the torsion of the cantilever is measured as it is dragged over the film surface at a constant applied normal force  $F_N$  and velocity ( $v = 250 \text{ nm s}^{-1}$ ). The measured torsion is directly proportional to the lateral forces  $F_L$  during sliding. To separate changes in topography from friction effects, so-called friction loops – trace and retrace scanning along the same line on the film surface – are recorded  $F_F = 1/2 \cdot (F_{L,trace} - F_{L,retrace})$ .<sup>[53]</sup>

Friction forces  $F_F$  were obtained by averaging over 50 friction loops that were recorded within a  $100 \times 250 \text{ nm}^2$  surface region with a point density of  $1 \text{ nm}^{-1}$  along the fast, and  $0.5 \text{ nm}^{-1}$  along the slow scan direction for each normal load and film. To assess how robust and reproducible the friction measurements are and to determine the order of magnitude of possible variations, the measurements were repeated several times on randomly selected areas on the film surface. In addition, to minimize wear during the friction experiments, the applied normal forces  $F_N$  were kept below 30 nN and any possible changes in the contact were monitored through adhesion measurements.

By measuring the frictional forces on the same surface area as a function of an applied load, a friction coefficient  $\mu$  between the tip and the specimen can be determined using a modified Amontons relation

$$F_F = \mu \cdot (F_N + F_{F0}) \quad (5.6)$$

where the term  $F_{F0}$  is the non-vanishing frictional force at  $F_N = 0 \text{ N}$  and is related to adhesion forces  $F_A$  between tip and film, that are non-negligible at the nanoscale.<sup>[53]</sup>

Adhesion forces were equated to the pull-off forces obtained by averaging over 50 force-distance curves. Significant changes in adhesion forces before and after probing the frictional properties can indicate changes in tip geometry due to wear, changes in the surface chemistry, or electrostatic forces do to triboelectrification.<sup>[193]</sup> To ensure that our friction measurements did not alter the surface morphology or affect the friction forces measured, an overview scan of the measurement area was performed after friction measurements.

To measure several films consecutively without the need to change the cantilever or the force calibration, up to four films were adhered to a Omicron stainless steel sample plate using a silver-filled epoxy (*EPO-TEK H21D*) to ensure good thermal and electric conductivity. Additionally, a small droplet of contact silver (*ACHESON 1415 G3692*) was placed at the edge of each film, far away from the area studied, to electrically contact the sample surfaces.

## 5.2.4. Results and Discussion

### XPS Measurements

XPS measurements were performed to confirm the chemical composition of the manganite film surfaces. In addition to the La, Sr, and Mn peaks, the spectra's exhibit an additional peak at 684.45 eV which can be assigned to fluorine (F) (see fig. 5.6a, full spectrum, see appendix A.1.4).

In manganites, F is known as a source of contamination in sample preparation involving Teflon components<sup>[194]</sup> or as a dopant in  $\text{LaMnO}_3/\text{SrMnO}_3$ .<sup>[195]</sup> If F is present as a contaminant on the sample surface, a F1s binding energy of 689.8 eV is expected, together with a C1s signal at 292.5 eV, reflecting C-F bonds.<sup>[194]</sup> However, the measured F 1s binding energy is significantly smaller and no component in the C1s peaks at 292 eV is observed (see appendix A.1.5). Therefore, we can rule out that F is present as a surface contaminant. Instead, the binding energy of the F1s peak matches with  $\text{SrF}_2$  (684.6 eV)<sup>[196]</sup> or  $\text{LaF}_3$  (684.5 eV),<sup>[197]</sup> suggesting that F dopes the material by replacing oxygen in our films.<sup>[195]</sup>

The fluorine content in our films was estimated from the F1s and Mn2p peak intensities using standard methods (see fig. 5.6b and appendix A.1.4). It can be observed that the films with top layer thickness of  $m = 4$  and 14 exhibit a particularly high F concentrations compared to the other five superlattice films.

In systems such as  $\text{SrMnO}_{(3-x)}\text{F}_x$  fluorine doping can result in ferromagnetic behavior, the occurrence of a charge ordered magnetic transition, local distortions of Mn octahedra,<sup>[195]</sup> and a reduced electrical conductivity.<sup>[198]</sup> Similarly, F doping can introduce a short-range magnetic

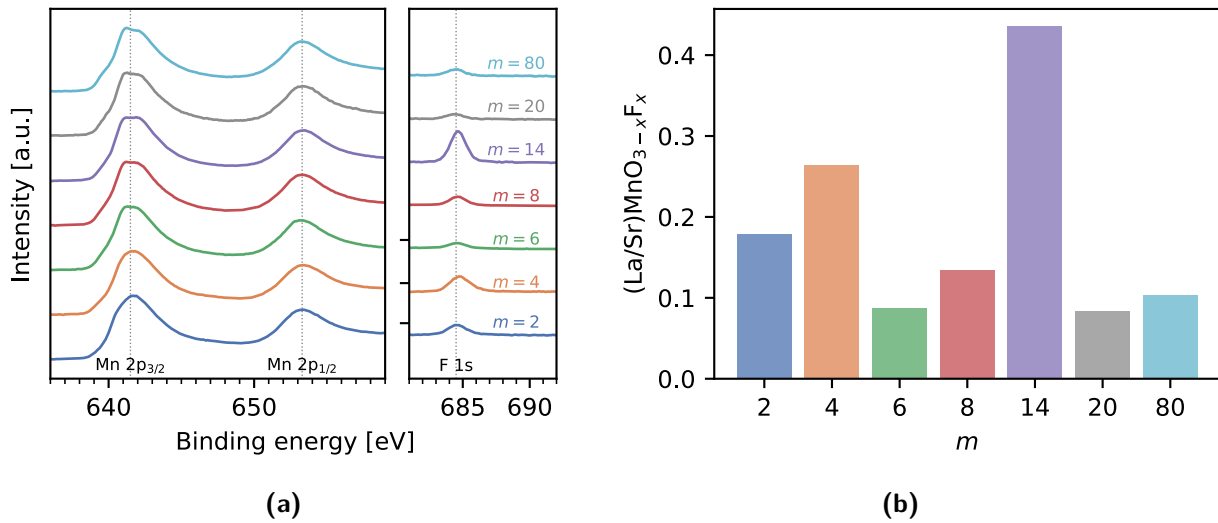


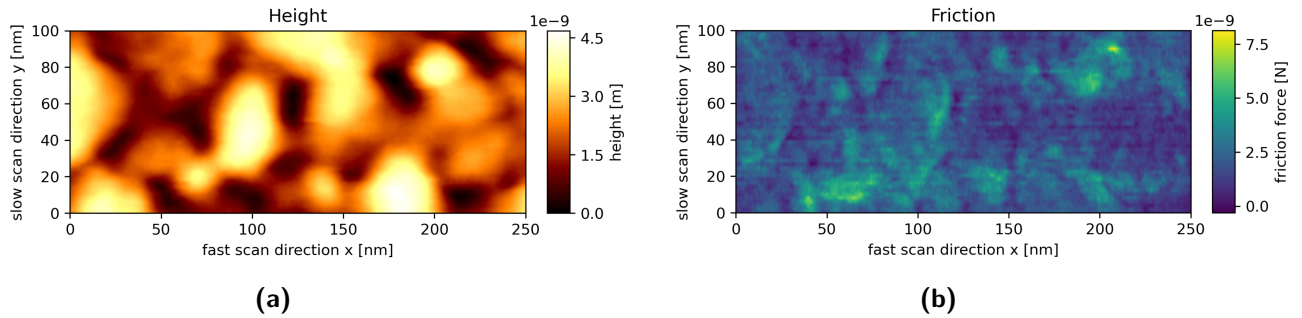
**Figure 5.6:** (a) Excerpts from XPS spectra showing the  $\text{Mn}2p_{1/2}$  and  $\text{Mn}2p_{3/2}$  peaks at binding energies of 653 eV and 641 eV, as well as the  $\text{F}1s$  peak at a binding energy of 685 eV. (b) The fluorine concentration in the near surface region of the superlattice samples is determined from the ratio of the Mn to F-peak areas. The full spectra, as well as further details on the evaluation, are presented in the supporting information (see appendix A.1.4).

order in  $\text{LaMnO}_{2.8}\text{F}_{0.2}$ <sup>[199]</sup> or can lead to ferroelectric properties of  $\text{LaMnO}_2\text{F}$ ,<sup>[200]</sup> thus altering structural, electric, and magnetic properties. However, such a variation is not detected in our SQUID measurements (see appendix A.1.6).

Since we will observe in the subsequent sections that the significantly higher fluorine concentration in samples  $m = 4$  and 14, will have a significant influence on the measured frictional forces, we will discuss them separately.

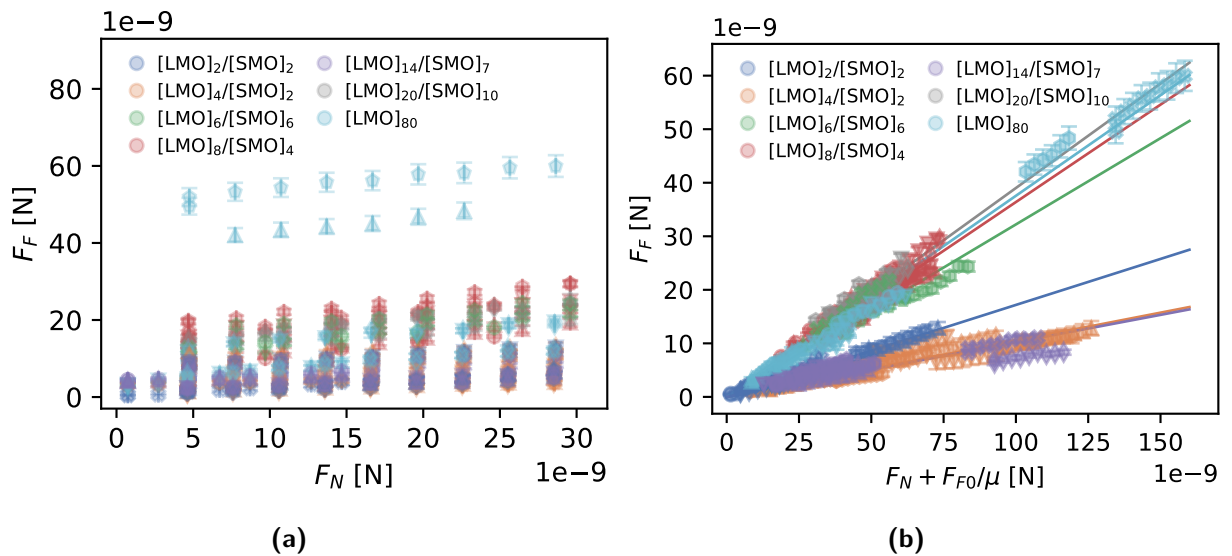
## Friction Measurements

Figure 5.7 depicts a topography map and the corresponding friction map, that is calculated from the lateral traces measured for a  $[\text{LaMnO}_3]_2/[\text{SrMnO}_3]_2$  film. A Spearman correlation coefficient of  $r_S = 0.014$  between the height and friction maps and of  $r_S = 0.08$  between the friction and height gradient along  $x$ -direction, indicating no correlations between friction and topography, and support the validity of the lateral force method<sup>[53]</sup> to measure friction. Similar surface topographies and friction maps were obtained on all  $[\text{LaMnO}_3]_m/[\text{SrMnO}_3]_n$  films and show comparably low correlations  $r_S < 0.15$  and surface roughness  $\text{RMS} \leq 0.5$  nm. All films show small variations in the friction force ( $\pm 2$  nN) on a length scale of about 50 nm (see fig. 5.7). Shifts in the absolute values of friction forces from map to map are on the order



**Figure 5.7:** (a) Topography and (b) corresponding friction maps of a  $[\text{LaMnO}_3]_2/[\text{SrMnO}_3]_2$  surface. The topography map shows a smooth surface with a roughness of  $\text{RMS} = 0.4$  nm, and no apparent correlation between the calculated friction map and topography.

of  $\pm 5$  nN and indicate small changes in surface chemistry, variations in top layer thickness (see table 5.1), carbon-based surface residues and adsorbed water. Occasional larger shifts ( $\pm 10$  nN) are sometimes observed when comparing different measurements made with different cantilevers and can be attributed to changes in tip shape. Representative friction and topography maps for all films can be found in appendix A.2.



**Figure 5.8:** Friction forces  $F_F$  measured for each  $[\text{LaMnO}_3]_m/[\text{SrMnO}_3]_n$  film show (a) linear dependencies on the applied normal load  $F_N$  with slopes  $\mu$  that are fairly constant for each film and intercepts  $F_{F0}$  which vary strongly from map to map. (b) The friction forces for each film collapse onto a single proportional line when plotted against  $F_N + F_{F0}/\mu$ .

Friction forces  $F_F$  for each film were measured for applied normal loads  $F_N$  ranging from 1 to 30 nN by averaging over a single friction map ( $250 \text{ nm} \times 100 \text{ nm}$ ) region). The friction increases

linearly with normal force, irrespective of the  $m/n$  ratio and fluorine content (see fig. 5.8a and appendix A.3.1). Linear regressions (eq. 5.6) to the friction data were performed to obtain the non-zero friction force intercept  $F_{F0}$  as well as a friction coefficient  $\mu$  (slope) for each individual friction versus normal force measurement (see fig. 5.8a and appendix A.3.1). While the slopes  $\mu$  did not show a large variation between measurements on a given sample, the values for  $F_{F0}$  vary from map to map and show no clear dependence on nominal layer thicknesses or other material properties (see appendix A.3.1). However, when divided by the friction coefficient  $F_{F0}/\mu$ , they correlate well with the pull-off forces obtained from force-distance-curves (see appendix A.3.2), in good agreement with various models for elastic contacts that include adhesion.<sup>[24,48]</sup> In fact, we find that the friction forces for each film are reasonably well described as proportional to the sum of the applied normal load  $F_N$  plus the adhesive force as estimated by  $F_{F0}/\mu$  (see fig. 5.8b and appendix A.3.3). Average friction coefficients  $\bar{\mu}$  for each film were obtained from the best fit slopes to these data (fig. 5.8b).

The fact that the friction forces for each sample are approximately described by a master curve that is linear in the applied normal load plus  $F_{F0}/\mu$ , is in good agreement with the Derjaguin, Muller and Toporo (DMT) model for adhesive elastic contacts.<sup>[24,33]</sup> This model provides a good description of adhesive contacts between two hard materials and includes adhesion forces both inside and outside the contact area.<sup>[24]</sup> The model assumes that the contact profile remains the same as for a Hertzian contact, although this is clearly an over-simplification, particularly in the limit of small, applied forces. Several different descriptions of the adhesive contribution have been considered, but in the simplest approach, the adhesive force is added to the applied force in the Hertz contact equations.<sup>[48]</sup> In this model, the adhesive force is equal to the pull-off force and given by  $F_A = 2\pi R\gamma$  where  $R$  is the radius of the AFM tip (assumed spherical) and  $\gamma$  is the work of adhesion. The measured pull-off forces (between 3 and 75 nN, appendix A.3.3) agree well with this model for a tip radius  $R = 10$  nm, yielding values of  $\gamma$  between 0.05 and 1.20 J m<sup>-2</sup>.<sup>[48,49]</sup>

The friction coefficients  $\mu$  (fig. 5.8a) and  $\bar{\mu}$  (fig. 5.8b) obtained from the best fit slopes to the data for the different films are between 0.1 and 0.4, and are comparable to AFM friction coefficients on other manganite thin films.<sup>[1,2]</sup> The coefficients are plotted against the thermal resistivity  $1/\kappa$  and top layer thickness  $d$  of each film (fig. 5.9), where the two films with the highest fluorine content are indicated by red data points and have noticeably lower friction coefficients than most other films. There is no clear trend of the friction coefficients with thermal resistivity (fig. 5.9), even after considering the two different  $m/n$  ratios and possible effects of F doping. In contrast, the plot of the friction coefficients versus the top layer thickness (fig. 5.9b) shows a clear trend, when the highly F doped specimens are excluded: the

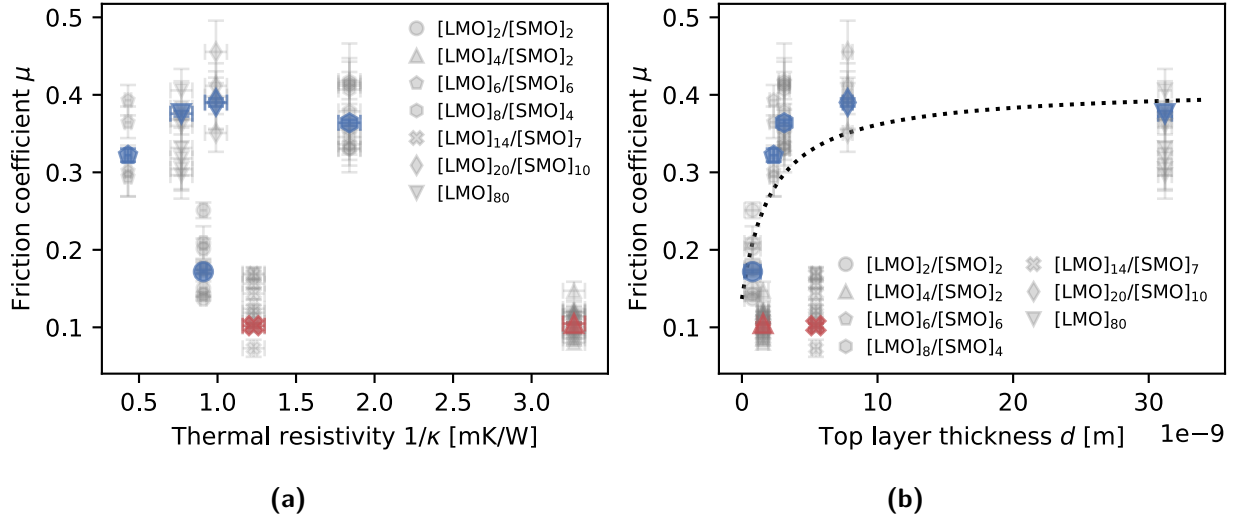


**Figure 5.9:** Friction coefficients of the seven different superlattice films plotted against **(a)** thermal resistivity  $\kappa^{-1}$ , and **(b)** LaMnO<sub>3</sub> top layer thickness. The friction coefficients  $\mu$  obtained from each individual series of measurements are shown as gray data points (from fig. 5.8a and appendix A.3.1); the blue or red data points are the average values  $\bar{\mu}$  for each film (from fig. 5.8b and appendix A.3.3). The red data points indicate the films with high fluorine concentrations. There is no apparent trend of friction coefficient with thermal resistivity **(a)**, while the coefficients of the undoped films (blue data points) increase and saturate with LaMnO<sub>3</sub> top layer thickness **(b)**. The dashed line is a fit with eq. 5.8.

friction coefficient increases with top layer thickness and then saturates above a thickness of around 5 – 10 nm. This is also seen in fig. 5.8b, where the slope of the friction force versus  $(F_N + F_{F0})/\mu$  systematically increases with top layer thickness.

The lack of a clear dependence of the friction coefficient on the thermal resistivity (fig. 5.9a) suggests that friction is not controlled by the GHz to THz range phonons which determine the thermal conduction in these materials.<sup>[117]</sup> Instead, it seems likely that friction is dominated by the much lower frequency mechanical vibrations that are present during AFM measurements, such as observed in studies of sonolubricity.<sup>[201]</sup> These mechanical vibrations range from washboard frequencies on the order of 1 kHz up to cantilever mechanical resonances as high as 100 kHz. Presumably, excess GHz to THz phonons are not strongly generated by the mechanical vibrations, and so do not play a role in determining friction. Furthermore, these results indicate that the dissipation of heat by thermal conduction does not appear to play a decisive role in friction.

Instead, the friction coefficients show a clear trend with LaMnO<sub>3</sub> top layer thickness, pointing to the role of the sub-surface material properties on friction, since the surfaces of all film samples are the same. Further, the fact that the friction coefficient saturates for layers thicker

than around 10 nm indicates that material properties to this depth affect energy dissipation at the sliding AFM contact. The idea that surrounding material properties affect friction is not new, and several studies support it. [1,2,14–17,19,85,145,175–178] However, to our knowledge, all these studies involve either a change in electronic properties (and possibly in electrostatic forces) or a phase transformation, so that the bonding states of the atoms at the surface are likely changed. In the results we present here, the surface roughness and chemistry of all samples are the same, yet the material properties at a depth between 0.8 and 10 nm below the surface cause the friction coefficient to change by up to a factor of more than two.

In most discussions of friction, it is assumed that the friction force results from dissipative processes occurring exclusively in the contact area. The ground-breaking model of Bowden and Tabor, [25] which was able to provide a physically reasonable interpretation of the seemingly nonphysical Amontons/Coulomb friction laws, is based on the idea that friction is simply proportional to the true area of contact between the sliding materials. For AFM measurements of friction,  $F_F \propto \pi a^2$ , where  $a$  is the contact area radius between the tip and the sample. However, our results show unequivocally that contributions from the surrounding materials also contribute. In addition, for an elastic contact between a tip of radius  $R$  and a flat sample, the contact area scales sub-linearly with the normal force,  $a^2 \propto F^{2/3}$ , which contradicts the measured linear dependence observed here.

We therefore propose that the stressed regions of the material surrounding the contact interface contribute to friction through internal damping, an effect which we estimate from thermoelasticity. According to Hertz elastic contact theory, [30,40] the stress fields under a spherical AFM tip fall off over several nanometers for typical AFM tip radii and normal forces, consistent with our observation that the friction "feels" to a depth of around 10 nm. Through thermoelastic coupling, the stress fields produced by a sliding tip would – under adiabatic conditions – cause local temperature changes  $\Delta T = -(\alpha/\rho c_p) T_0 \Delta\sigma$ , where  $\alpha$  is the linear thermal expansion coefficient,  $\rho$  the density,  $c_p$  is the volumetric specific heat at constant pressure,  $T_0$  is the ambient temperature and  $\Delta\sigma$  is the sum of the principle stresses. [41] The resultant temperature gradients produce heat flow which can be as large as  $Q = -\varepsilon_{th} V \Delta\sigma$ , where  $V$  is the stressed volume, and  $\varepsilon_{th} = T_0 \alpha$  the thermal strain. For an AFM tip sliding with speed  $v_s$ , the power  $P = F_F v_s$  of sliding friction that can be dissipated by the thermoelastic effect can be estimated as,

$$P = F_F v_s = 2f \varepsilon_{th} V \Delta\sigma \approx v_s \cdot 8/\pi \cdot \varepsilon_{th} \cdot (F_N + F_A), \quad (5.7)$$

where  $f$  is the frequency of loading and unloading under the tip. The factor of 2 after the second equality originates from the assumption that the heat flow is generated both on loading and unloading. eq. 5.7 assumes that these processes are entirely irreversible, and eq. 5.7 is to be seen as an upper limit of the contributions to friction from thermoelasticity. How closely realistic conditions may come to it will be investigated in future work using microscopic models. For continuous, smooth sliding,  $f$  is given by  $v_s/(2a)$ . The quantity  $V\Delta\sigma$  can be approximated as  $8a^3 p_m$  where  $p_m = (F_N + F_A)/(\pi a^2)$  is the mean contact pressure within the contact<sup>[30,40]</sup> and falls off over a distance that scales with  $a = (3R \cdot (F_N + F_A)/(4E^*))^{1/3}$ , which is the radius of the contact area between a tip of radius  $R$  and the flat sample. Using the nominal AFM tip radius of  $R = 10$  nm, the contact radius will range between 0.52 and 2.83 nm, and the contact pressure will range between 1.18 and 6.56 GPa for our experiments.<sup>[44,202,203]</sup>  $E^*$  is the so-called indentation modulus depending on elastic properties of both the sample and the tip and is 97 GPa for our system.<sup>[44,202]</sup> Since the elastic constants of the layer materials differ by only about 7%, we can ignore effects of the composite structure on the stress fields. The estimation of the stressed volume under the tip by  $V\Delta\sigma$  is a strongly simplified; the reasons being that the stresses are heterogenous and the exact form of the adhesive forces in the contact area are unknown.

In addition to providing an explanation for the dependence of the friction force on the sub-surface material properties according to eq. 5.7, the thermoelastic damping due to the moving stress fields under the sliding tip predicts a linear dependence of friction on normal force, with a contribution from thermoelasticity to the friction coefficient that can be as large as  $\mu_{TE} = 8/\pi \cdot \varepsilon_{th}$ . A necessary requirement is that the diffusion occurs much faster than tip motion, which is the case for our system  $D_{th} > v_s/f$ , where  $D_{th}$  is the thermal diffusivity and is of order  $7 \times 10^{-7} \text{ m}^2 \text{ s}^{-1}$  for  $[\text{LaMnO}_3]_m/[\text{SrMnO}_3]_n$  superlattices.<sup>[117]</sup> The thermal expansion coefficients of the superlattices are of order  $1.5 \times 10^{-6} \text{ K}^{-1}$ <sup>[204]</sup> so that the contribution of thermoelasticity to friction is  $\mu \approx 1.2 \times 10^{-2}$ . Surprisingly, this is only a factor of 10 smaller than the measured friction coefficients and comes closer to explaining the experimental values than the available models based on electronic excitations,<sup>[15,84]</sup> which are many orders of magnitude too small. Any structural or electronic defects will increase the damping above what is discussed here. Contributions from dissipative processes in the contact area will also contribute to the friction, although the exact mechanism continues to be a topic of debate.<sup>[31,33,205,206]</sup>

For the superlattice films investigated here, any contributions to the friction from contact area dissipation will be the same for all films, while the contribution from the thermoelastic effect

will depend on the layer thicknesses and the depth of the stress fields, which depend on the normal force. We can write an approximate expression for the thermoelastic contribution to friction,

$$\mu_{TE}(d) = (\mu_{LMO} - \mu_0) \cdot g(d/a) + \mu_0 \quad (5.8)$$

where  $\mu_{LMO} = 8/\pi \cdot \varepsilon_{LMO}$  and  $\mu_0 = 8/\pi \cdot \varepsilon_0$ . The function  $g(d/a)$  represents the fraction of the thermoelastically damped volume that lies in the top  $\text{LaMnO}_3$  layer and changes from 0 to 1 as  $d$  increases from zero to infinity. A plot of the measured friction coefficients versus  $d/a$  shows the data can be described by the simple functional form  $g(d/a) = d/(d+a)$  (see appendix A.3.4) although there is no apparent physical basis for this dependence. The same functional form also gives a good description of the integrated stress fields under a spherical tip<sup>[30,40]</sup> (see appendix A.4). Moreover, the functional form is in quantitative agreement with a viscoelastic model developed by Lee et al.<sup>[3]</sup>, which attributes top layer thickness dependent friction to viscous dissipation inside the evanescent waves set up in the top layer by a vibrating tip.

We use eq. 5.8 to fit the data in fig. 5.9b, which shows that the expansion coefficients of  $\text{LaMnO}_3$  must be larger than that of  $\text{SrMnO}_3$  by more than a factor of two to account for the measurements, since the friction coefficient increases from around  $\bar{\mu} = 0.17$  for the thinnest layers, where the stressed volume under the tip extends over several different layers, up to  $\bar{\mu} = 0.4$ , where the stressed volume lies entirely in the  $\text{LaMnO}_3$  top layer. We have found two literature sources for thermal expansion coefficients in these materials, confirming that the thermal expansion coefficient of  $\text{LaMnO}_3$  ( $\alpha_{LMO} \approx 14.6 \times 10^{-6} \text{ K}^{-1}$  [204]) is larger than of  $\text{SrMnO}_3$  ( $\alpha_{SMO} \approx 8.75 \times 10^{-6} \text{ K}^{-1}$  [207]), although not quite by a factor of two.

As far as we can tell, this publication and a recent theoretical study<sup>[3]</sup> are the first to discuss contributions of thermoelastic damping to measured friction, although thermoelastic damping in AFM cantilevers is routinely considered when interpreting dynamic AFM measurements.<sup>[17]</sup> We have found no literature discussing thermoelastic damping in the stressed volume around the contact area, which yields an estimate for vibrational damping.<sup>[208,209]</sup> Although the thermoelastic contributions are somewhat too small to fully account for the measured friction forces, they do provide a simple and clear framework for explaining why friction forces often scale linearly with normal forces and why they are dependent on sub-surface material properties. Internal damping has indeed been suggested theoretically as a main contribution to damping of a weakly coupled probe.<sup>[3]</sup> In this study, the found dependence on layer thickness is strikingly similar to what is observed in our experiments and to what is estimated from thermoelasticity. Lee et al.<sup>[3]</sup> identified the local dissipation as originating from evanescent

phonons, which can be interpreted as being excited by a moving stress field. How far these mechanisms share the same physical origins poses an exciting question for future work.

Macroscale contacts are composed of many individual elastic and plastic contacts between micrometer- to nanometer-scale asperities, each of which is expected to behave similarly to an AFM contact. As such, thermoelastic damping should play an important role in macroscale friction as well. The stress fields under a macroscale contact reach to a depth comparable to the individual asperity contact area dimensions, on the order of nanometers or micrometers, so that the contributions of thermoelastic damping relative to dissipation in the contact area should be the same in macroscale contacts as in the AFM studies. Of course, friction at macroscale contacts also involves contributions from plasticity, so the separation of all the contributions and prediction of friction coefficients becomes even more complex.

### 5.2.5. Conclusions

We report AFM-based friction measurements on seven  $[\text{LaMnO}_3]_m/[\text{SrMnO}_3]_n$  superlattice films, finding an increase in friction with increasing in  $\text{LaMnO}_3$  top layer thickness for chemically identical surfaces. When the layer thickness exceeds several nanometers, friction saturates to the value found for bulk  $\text{LaMnO}_3$ . This observation shows a connection between friction and material properties up to several nanometers below the surface, and thus contradicts the widely accepted picture that friction at an elastic contact only occurs by dissipative processes in the contact area. [\[31,33,205,206\]](#)

We explain the contribution of the surrounding material to friction by thermoelastic damping in the stressed material near the contact interface. Using simple scaling arguments from elastic contact theory, we can show that thermoelastic damping provides a non-negligible contribution to measured friction forces at both nanoscale and macroscale contacts. Furthermore, thermoelastic damping provides a possible explanation for the observed linear dependence between AFM friction and normal forces, which is otherwise expected to show sublinear behavior if only dissipative processes in the contact area are considered.

The work presented here introduces thermoelastic damping as an important contribution to AFM friction. In contrast to the dissipative processes occurring directly in the contact, which are highly sensitive to real-time conditions, the contributions from thermoelastic and internal damping can be tailored through material selection, thus revealing possible strategies to reliably control friction.

### 5.2.6. Acknowledgements

This work was funded by the German Research Foundation (DFG) 217133147/SFB 1073 Project A01 and Project A02. The authors thank D.R. Baer, M.H. Engelhard from [Pacific Northwest National Laboratory](#) for discussion and help in interpreting the fluorine contamination observed in XPS measurements. We would like to thank R.L.C. Vink for critical discussions of our measurement results. We thank T. Brede for x-ray characterization of all films and SEM measurements of cantilevers. Additionally, we thank A. Wodtke and F. Güthoff from the [Max Planck Institute for Multidisciplinary Sciences, Göttingen](#) for providing access and to maintain the Omicron VT-AFM system.

## 6. Conclusion

This goal of this thesis was to refine our understanding of how the friction forces measured at the surface are correlated to the surrounding material properties. In particular, the objective was to identify the dominant dissipation channels which are responsible for converting high-quality mechanical energy into heat, and disentangle the underlying mechanisms.

The question of how friction is correlated with the surrounding material properties has received considerable attention<sup>[1,2,14–17,19,85,145,175–178]</sup> and two dominant energy dissipation mechanisms are identified: 1. Dissipation due to interactions with the electron system, and 2. dissipation due to phonon excitation. Which of these two dominates for the specific system varies greatly, and the interpretations are not always consistent with one another. To clarify these questions, AFM-based studies on manganite thin films were conducted, in which the phononic and electronic degrees of freedom of the system can be selectively controlled by phase transitions or interfaces in the material.

### Temperature Dependent Friction Measurements

To decipher which material properties contribute to friction, temperature-dependent friction measurements on  $\text{La}_{0.8}\text{Sr}_{0.2}\text{MnO}_3$  thin films were performed in the first part of the thesis. Thereby, the fundamental concept was to study how friction is altered by the change in material properties at the second order phase transformation ( $T_C = 220\text{ K}$ ) in the manganite thin film.

In connection with the phase transformation from a FM metal to a PM polaronic conductor, a significant change in friction force was observed (see section 5.1). The measurements on  $\text{La}_{0.8}\text{Sr}_{0.2}\text{MnO}_3$  allowed to assess the reproducibility of the temperature dependent measurements on  $\text{La}_{0.7}\text{Sr}_{0.3}\text{MnO}_3$  conducted prior to this thesis.<sup>[11]</sup> In addition, based on additional velocity dependent friction and electrostatic measurements, the influence of the electrical/electrostatic and phononic contributions could be characterized more thoroughly. It was concluded that the former are orders of magnitude too small to be accountable for the observed change in friction.<sup>[11]</sup> Based on these observations, and further measurements on

manganites,<sup>[1]</sup> it was concluded that the increase in friction is associated with the emergence of Jahn-Teller-distortions and small-polarons at the phase transformation – an observation that is consistent with theoretical predictions regarding these contributions (see section 2.3).

The results of these studies were published as “*Polaronic Contributions to Friction in a Manganite Thin Film*” in *Advanced Science* 2003524 (2020),<sup>[2]</sup> and summarizes the insights gained from the temperature-dependent friction measurements on  $\text{La}_{(1-x)}\text{Sr}_x\text{MnO}_3$  performed in this thesis.

In addition to the temperature-dependent friction measurements conducted in this thesis, further temperature-dependent friction measurements were performed on a  $\text{La}_{0.55}\text{Ca}_{0.45}\text{MnO}_3$ <sup>[1]</sup> thin film and a  $(\text{La}_{0.6}\text{Pr}_{0.4})_{0.67}\text{Ca}_{0.33}\text{MnO}$  thin film<sup>[210]</sup>. The aim here was to investigate to what extent a second order phase transition of the surrounding material affects the friction measured at the surface, and whether similar dependencies as in the case of  $\text{La}_{(1-x)}\text{Sr}_x\text{MnO}_3$  are evident. However, in contrast, these measurements did not reveal any changes in friction force and coefficient in connection with the phase transition, apart from the thermolubricity effect (decrease in friction force with increasing temperature, see section 2.2.2). The observations in both cases were explained by a possible depleted/altered insulating surface layer with a thickness up to a few nanometers.<sup>[150,211]</sup>

These conclusions raised the question of the depth into the material to which changes in material properties below the tip are detectable in friction measurements, and how universal the conclusions from the measurements on  $\text{La}_{(1-x)}\text{Sr}_x\text{MnO}_3$  are. At the same time, the previous measurements did not resolve which phonon modes are responsible for the observed change in energy dissipation. The questions raised were addressed in the second part of the thesis. The main findings and conclusions are summarized in the next section.

### **Friction Measurements on Superlattices**

Building on the successful demonstration of how friction can be controlled by a specific change in the material properties, friction measurements on seven superlattice samples, consisting of alternating  $\text{LaMnO}_3$  and  $\text{SrMnO}_3$  layers, were performed in the second part of the thesis. This material system seemed promising for several reasons: First, by keeping the chemistry of the top layer the same for all films studied, the influence of changing contact dynamics can be largely excluded. Secondly, by systematically varying the thickness ratio of the alternating  $\text{LaMnO}_3$  and  $\text{SrMnO}_3$  layers, the propagation of thermal phonons can be specifically suppressed.<sup>[117]</sup> Thirdly, by systematically varying the thickness of the surface layer, theoretical predictions<sup>[3]</sup> and the question up to what depth changes in material properties affect friction

could be addressed.

To examine the proposed correlations by theory<sup>[3]</sup> and to address open questions, friction measurements were performed on seven superlattice samples  $[\text{LaMnO}_3]_m/[\text{SrMnO}_3]_n$ . The samples were prepared by MAD and extensively characterized (see appendix A.1). All superlattice stacks were terminated with a  $\text{LaMnO}_3$  layer, whose thickness ranged between 0.8 and 32 nm (see section 5.2) to ensure comparable surface chemistry.

These measurements revealed that for samples with comparable surface chemistry, the measured friction forces and coefficients are not affected by the thermal resistivity properties of the given samples. The lack of correlation indicates that the observed changes in friction are likely not attributed to propagation of high-frequency phonons (THz-GHz) which are associated with this material property.<sup>[117]</sup>

Instead, a clear dependence of the friction coefficient on the  $\text{LaMnO}_3$  top layer thickness was observed. The friction coefficients measured increase with increasing top layer thickness and saturate when the top layer thickness exceeds 5 nm. Based on the apparent correlation between the two quantities, the notion that sliding friction can solely be attributed to interactions at the surface could be ruled out. Instead, the friction measurements suggest that friction is determined by the material properties within the elastically strained volume below the sliding tip. This conclusion is conceptually similar to a viscoelastic model proposed by Lee et al.<sup>[3]</sup> Here the authors attribute the energy dissipated at a sliding nanoscale contact to the excitation of evanescent waves, that decay over a length scale set by the interaction area.

In summary, the study suggests that thermoelastic material properties within the first few nanometers of the contact surface govern the amount of energy dissipated. Further, the proposed dependence of friction on the thermoelastic properties presents a novel strategy to control friction by a tailored material selection.

The results of the experimental study on superlattices were submitted to a peer-reviewed journal in October 2022. The latest version of the manuscript is available at [ArXiv:2210.09677](https://arxiv.org/abs/2210.09677).<sup>[4]</sup>

In the studies on manganites, we could identify that a change in phononic or thermoelastic degrees of freedom of the surrounding material are crucial to estimate the energy dissipated during sliding friction. In the following, we will compare these two interpretations and explore to what extent they are compatible.

### Thermoelastic Contributions

In solids, phonons are responsible for all kinds of thermal properties, such as heat content and transport. Therefore, the thermal expansion coefficient, which was used to estimate the energy dissipation in friction measurements on the superlattice films (see section 5.2), is directly connected to the anharmonic part of the lattice vibrations in the respective system.<sup>[93]</sup> For systems in which the phononic degrees of freedom are strongly altered, e.g. through a phase transition, it is therefore to be expected that a change in the elastic properties will accompany the phase transformation. A change in the elastic properties, such as the bulk modulus  $B$ , is tantamount to a change in the thermal expansion coefficient. The proportionality between the two quantities is given by:<sup>[93]</sup>

$$\alpha = \frac{\gamma_G \rho c_V}{3B}, \quad (6.1)$$

$\gamma_G$  being the Grüneisen-parameter,<sup>1</sup>  $\rho$  the density and  $c_V$  the specific heat.

A measurement of elastic properties can be accomplished experimentally by either static measurements (nanoindentation) or kinetic measurements of the sound wave propagation. The latter method was used by Rajendran et al.<sup>[153]</sup> to characterize temperature dependent change elastic properties of a  $\text{La}_{0.67}\text{Sr}_{0.33}\text{MnO}_3$  thin film deposited on a MgO substrate. Here, the authors observe an abrupt lattice softening at the phase transformation from a ferromagnetic-metal to a paramagnetic-conductor, that they attribute to the coexistence of both phases at  $T_C = 367\text{ K}$ . Overall, the bulk modulus decreases by about 5% when comparing pre- and post-phase transition values. The authors<sup>[153]</sup> attribute the changes in elasticity, or rather the changes in sound velocities in both low and high-temperature phases, to a change in electron-phonon interactions originating from Jahn-Teller-distortions of the oxygen octahedra. Above  $T_C$  the overall decrease in sound velocity, and thus a decrease in modulus, is attributed to the hopping of small lattice polarons, that break up below  $T_C$ , and thus lead to an increase in modulus in the FM-phase.<sup>[153,212]</sup>

In addition to the elastic modulus  $B$ , the specific heat  $c_V$  enters eq. 6.1 as a temperature-dependent parameter. In measurements on  $\text{La}_{0.7}\text{Sr}_{0.3}\text{MnO}_3$ , it has been reported that the specific heat increases as a function of temperature.<sup>[213]</sup> In connection with the phase transition, an additional sudden increases in specific heat (approximately 20%) is observed.<sup>[213]</sup> After the phase transformation, the specific heat immediately drops to a value slightly elevated compared to before the phase transition.<sup>[213]</sup> For further increasing temperatures, the specific heat tends to slowly further increase.<sup>[213,214]</sup>

---

<sup>1</sup>The Grüneisen-parameter describes proportionally between a change of lattice vibration frequencies in connection with a lattice expansion. Typical values of the Grüneisen-parameter are in the range of  $\gamma_G = 2$ .<sup>[93]</sup>

From the measurements of specific heat  $c_V$  and bulk modulus measurements  $B$ , the thermal expansion coefficient  $\alpha$  would be expected to increase abruptly at the phase transition, by 20%, according to eq. 6.1. For temperatures  $T > T_C$ , an increase in  $c_V$  by 5% would be conceivable compared to a pre-phase transition value, based on the reported change in  $B$ .<sup>[153]</sup> The expected change in the thermal expansion coefficient in connection with the phase transition is thus in qualitative agreement with the temperature-dependent friction measurements on  $\text{La}_{(1-x)}\text{Sr}_x\text{MnO}_3$  (see figs. 5.1b to 5.1d). Here, too, a sudden increase in the measured friction forces (50% for  $x = 0.2$ , or 100% for  $x = 0.3$ ) was observed in connection with the phase transition. For temperatures  $T > T_C$  we observed that the friction forces are increased for both films (10% for  $x = 0.2$  and 80% for  $x = 0.3$ ) compared to a value before the phase transition. Although the change in  $\alpha$  estimated here is not sufficient to fully account for the magnitude of the observed changes in friction, it indicates that a change in thermoelastic properties makes a non-negligible contribution.

In summary, it is thus likely that our earlier considerations relating surface friction to the thermoelastic properties are applicable to the temperature-dependent friction measurements, and that the conclusions from both studies are consistent. However, further work is needed to explore the exact magnitude of this contribution.

### Fluorine Doping

Apart from the correlation between friction coefficient and film thickness, the friction experiments on  $[\text{LaMnO}_3]_m/[\text{SrMnO}_3]_n$  thin films revealed that small changes in surface chemistry can lead to significantly lower friction coefficients.

The evidence of near-surface fluorine was characterized by the means of XPS measurements. In addition to peaks that can be assigned to La, Sr, Mn and O, an additional peak at 685 eV was detected, especially pronounced at  $m = 4$  and  $m = 14$ , which can be assigned to F1s. By the peak position, the binding energy could be matched to systems such  $\text{SrF}_2$ <sup>[196]</sup> (684.6 eV) or  $\text{LaF}_3$ <sup>[197]</sup> (684.5 eV). As part of the investigations, the possibility of the occurrence of C-F bonds (F1s binding energy 689.8 eV<sup>[194]</sup>) was also considered; however, the presence of C-F bonds was ruled out for the superlattices investigated.

The question of how fluorine affects friction has been systematically studied only for fluorine intercalated in a graphene lattice, or C-F compounds, better known as PTFE or Teflon.<sup>[215–217]</sup> Here, the authors observe a strong influence of fluorine content on friction, which they attribute to a corrugation of the surface potential,<sup>[216]</sup> altered van der Waals forces,<sup>[217]</sup> or changes in the out-of-plane stiffness.<sup>[215]</sup> However, it appears that there is insufficient consensus in regard

to the experimental and theoretical mechanisms underlying these changes in friction.<sup>[217]</sup> In addition, due to the vastly different material properties of graphene in respect to perovskites, it is questionable how applicable these considerations would be for fluorine doped LaMnO in the first place.

In the context of our model,<sup>[3,4]</sup> a decrease in friction associated with increasing fluorine doping, would indicate increased rigidity of the crystal lattice. In systems such as SrMnO<sub>3</sub> and LaMnO<sub>3</sub> different studies report that fluorine doping can lead to a distortion of the Mn<sup>3+</sup> octahedra, resulting in altered magnetic and electronic properties.<sup>[195,198–200]</sup> Besides the ones cited here, there are no literature studies addressing how fluorine doping affects the stiffness of a perovskite lattice. The question of how fluorine influences the mechanical properties of the [LaMnO<sub>3</sub>]<sub>m</sub>/[SrMnO<sub>3</sub>]<sub>n</sub> superlattices studied in this thesis therefore remains unanswered. However, it is conceivable that the mechanical properties are altered due to the reported lattice distortion, as in the case of La<sub>0.67</sub>Sr<sub>0.33</sub>MnO<sub>3</sub>.<sup>[153]</sup> In order to make reliable statements in this respect, systematic investigations of the elastic properties in connection with fluorine doping would be required.

### Outlook

The AFM-based friction measurements performed in the thesis have provided clear evidence that the phononic degrees of freedom and especially the excitation of anharmonic modes play a crucial role in how energy is dissipated during friction on the nanometer scale. In addition, we have worked out to what depth material properties contribute, and discovered that the elastically strained volume below the tip can be used to estimate the length scale (5-8 nm). Based on this model, a gauge of the friction coefficient can be assessed from the thermoelastic properties of the sample studied.

However, these insights into the mechanisms underlying friction at the nanoscale were decisively fostered by the close collaboration between theory and experiment in Project A01 of the SFB 1073. Therefore, for the successful continuation of this project, it is of interest to continue the extensive teamwork.

With regard to the continuation of experimental work, materials should be considered in which the phononic contributions to frictional losses, or rather elastic properties, can be varied in a targeted manner. Thereby, it would be possible to further test both the viscoelastic model,<sup>[3]</sup> and the experimental conclusions of this work. Additionally, in favor of successful collaboration, methods should be used/develop that can directly test theoretical predictions in experimental setup. In terms of methodology, this could be achieved by a transition from

contact to non-contact AFM measurements, considering the non-trivial contribution of surface dynamics in contact experiments. In the non-contact experiment, the cantilever is excited to an oscillation close to its resonance frequency and held at a distance  $d$  above the sample surface. Approaching the cantilever towards the sample, leads to a deviation in oscillation frequency relative to the excitation frequency, due to interaction forces between tip and sample (see section 2.1.3). The shift in oscillation frequency, in respect to the tip sample distance, can thus be used to characterize the interactions between the cantilever and the sample surface.<sup>[218,219]</sup> A main assignment in the transition from contact to non-contact experiments will be to investigate to what extent the energy dissipation measured in non-contact mode can be compared to friction measurements in contact mode. Therefore, it would be advisable to initially study well-characterized sample systems, such as the manganite thin films used here,<sup>[1,2,4]</sup> or 2D materials such as graphene.<sup>[176,177,179]</sup> In addition to a comparison with established friction measurements, non-contact measurements on graphene could be utilized to characterize the relevance of possible edge effects, which could be of great interest for the further theory development.

In a second step, the non-contact method could be further developed so that, in addition to the excitation to perpendicular oscillations, parallel oscillations of the cantilever, relative to the sample surface, become possible. Theoretical considerations<sup>[3]</sup> did show that perpendicular or parallel oscillation of the cantilever above the sample stimulates different excitations in the sample, which could be investigated experimentally with this method.



# A. Appendix

The following sections contain the supporting information to the friction measurements on  $[\text{LaMnO}_3]_m/[\text{SrMnO}_3]_n$  superlattices (see section 5.2).

## A.1. SI - Sample Characterization

### A.1.1. Ellipsometry Measurements

The phase shift angle  $\Delta$  as a function of time  $t$  is monitored in situ during metal organic aerosol deposition technique (MAD). Using the known deposition rate  $v_{\text{LMO}} = 0.37 \text{ u.c. s}^{-1}$  and  $v_{\text{SMO}} = 0.25 \text{ u.c. s}^{-1}$  from previous studies, a superlattice with the desired  $m$  to  $n$  was deposited. The layer thicknesses were additionally characterized by XRR measurements (see appendix A.1.4).

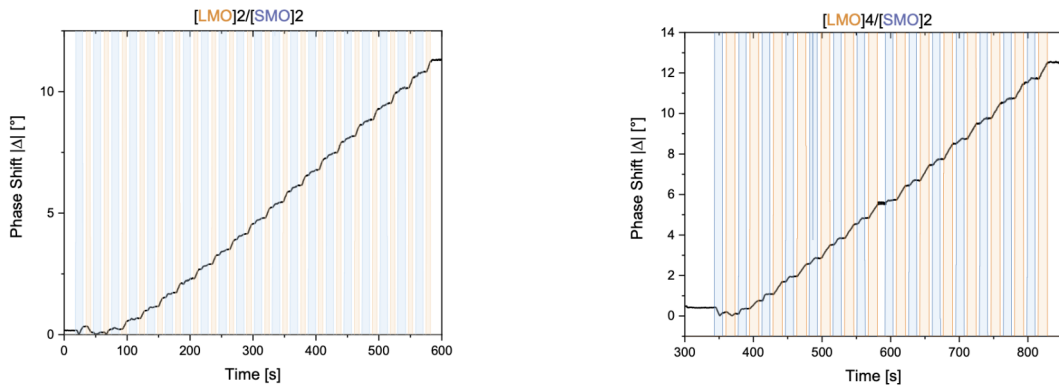
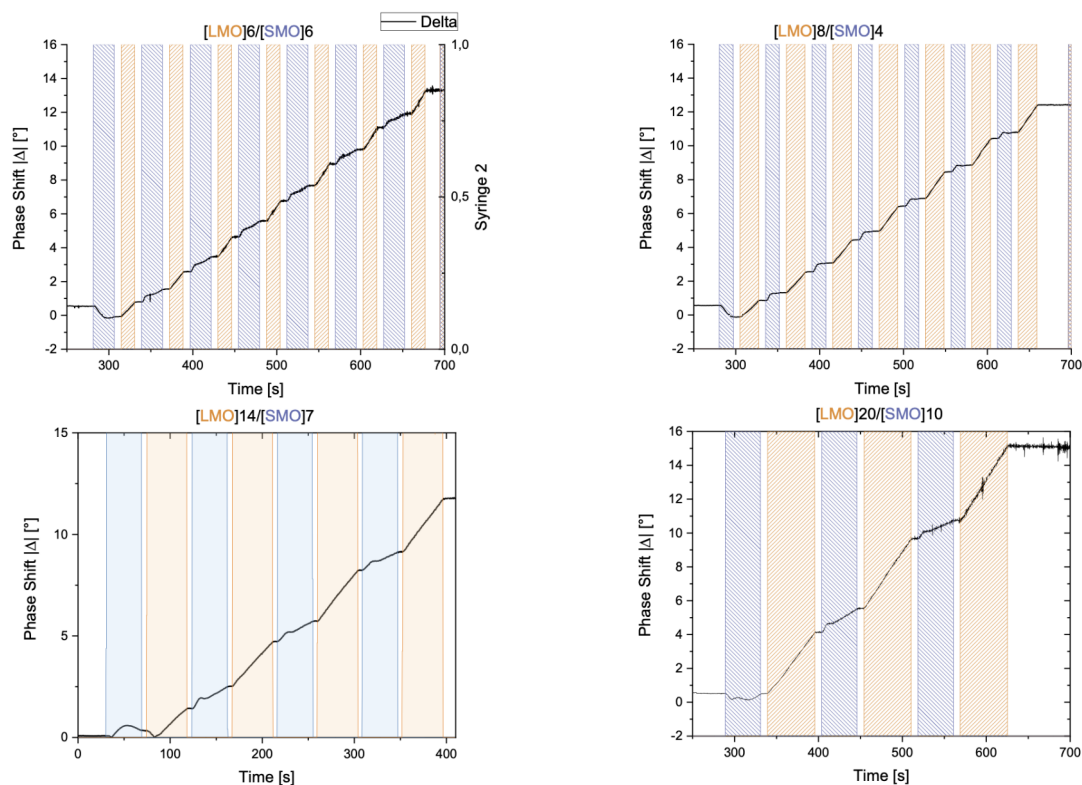


Figure A.1: Caption on next page.



**Figure A.1:** Ellipsometry phase shift angles  $\Delta$  measured during deposition of the superlattice films. The orange shaded regions correspond to  $\text{LaMnO}_3$  deposition and blue to  $\text{SrMnO}_3$  deposition.

### A.1.2. XRD Measurements

diffraction measurements were performed using a Bruker D8 Discover equipped with a  $\text{Cu } K_\alpha$  source. The measurements confirm the superlattice periodicity through superstructure reflections labeled by the numbers in below (see fig. A.2). Additionally, peaks that correspond to the characteristic wavelength of tungsten (W) can be identified, which are due to aging of the copper source. The peak positions indicated by dashed lines in fig. A.2 are listed in table A.1.

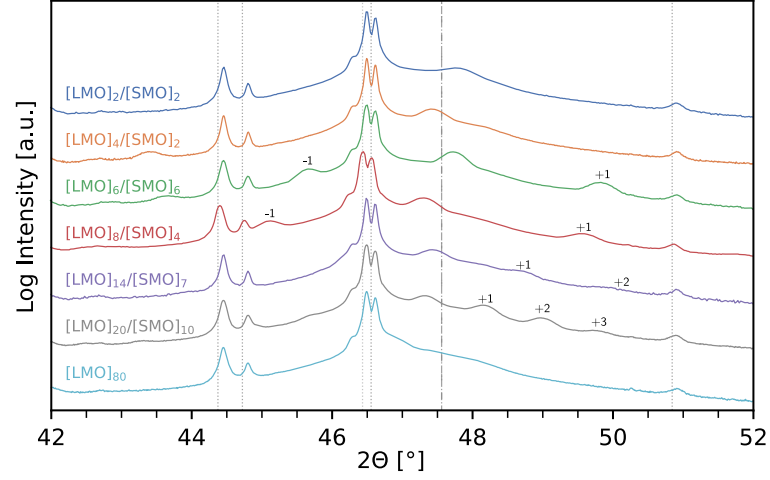


**Figure A.2:**  $\theta$ - $2\theta$  x-ray diffraction pattern from the films studied showing peaks corresponding to the substrate  $\text{SrTiNbO}_3$  as well as to the superlattice structure. The peak positions indicated by dashed lines are listed in table A.1.

Material	(hkl)	Wavelength	$2\Theta$
$\text{SrTiNbO}_3$	(002)	Cu $K\alpha_1$	46.433
		Cu $K\alpha_2$	46.555161
		W $K\alpha_1$	44.3734354
		W $K\alpha_2$	44.7219802
		W L	50.843
$\text{SrMnO}_3$	(200)	Cu $K\alpha_1$	47.559
$\text{LaMnO}_3$	(002)	Cu $K\alpha_1$	46.9399526
		W $K\alpha_1$	43.4585829

**Table A.1:** Peaks shown in the  $\theta$ - $2\theta$  x-ray diffraction pattern can be assigned to the  $\text{SrTiNbO}_3$  substrate and the  $\text{LaMnO}_3/\text{SrMnO}_3$  layers of the superlattice films. Further peaks that correspond to the characteristic wavelength of tungsten (W) are observable.

### A.1.3. XRR Measurements

x-ray reflectivity (XRR) measurements were carried out using a Bruker D8 Advance equipped with a Cu  $K\alpha$  source. To determine layer thicknesses and periodicities as well as interface roughness, the data was modeled using the GenX software.<sup>[220]</sup> In this software, the samples were modeled as a stack of alternating  $\text{LaMnO}_3$  layers with thickness  $d_{\text{LMO}}$  and roughness  $\sigma_{\text{LMO}}$ , and  $\text{SrMnO}_3$  layers with thickness  $d_{\text{SMNO}}$  and roughness  $\sigma_{\text{SMO}}$ . The measured data with the corresponding fits are depicted in fig. A.3. The parameters obtained from fitting are listed in table A.1.

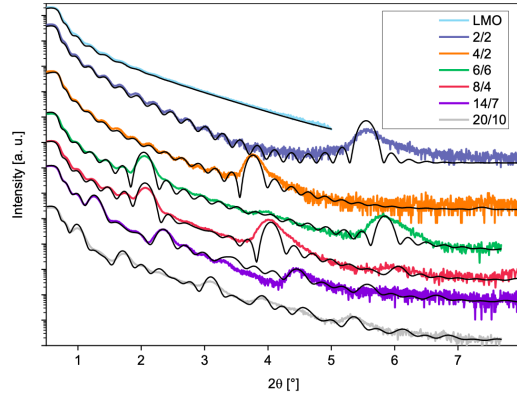


**Figure A.3:** XRR measurements of the  $m/n$ - superlattice films  $[\text{LaMnO}_3]_m/[\text{SrMnO}_3]_n$ . The black curves show the best fit for each sample using the algorithms provided by the GenX software.<sup>[220]</sup>

Sample	$d_{\text{LaMnO}}$ [Å]	$\sigma_{\text{LaMnO}}$ [Å]		
LaMnO <sub>3</sub>	316(3)	5.08(3)		
m/n	$d_{\text{Bilayer}}$ [Å]	$\sigma_{\text{LaMnO}}$ [Å]	$\sigma_{\text{SrMnO}}$ [Å]	
2/2	16(1)	6 (1)	3(2)	
4/2	24(1)	4(1)	7(3)	
m/n	$d_{\text{Bilayer}}$ [Å]	$\sigma_{\text{LaMnO}}$ [Å]	$d_{\text{SrMnO}}$ [Å]	$\sigma_{\text{SrMnO}}$ [Å]
6/6	23(1)	3.1(3)	23(1)	3.4(7)
8/4	31(2)	3.8(6)	13(1)	4.5(2)
14/7	54(1)	3.3(3)	27(2)	6.7(9)
20/10	75(2)	3.6(2)	42(2)	5.6(7)

**Table A.2:** Peaks shown in the  $\theta$ - $2\theta$  x-ray diffraction pattern can be assigned to the SrTiNbO<sub>3</sub> substrate and the LaMnO<sub>3</sub>/SrMnO<sub>3</sub> layers of the superlattice films. We also identify diffraction peaks that correspond to the characteristic wavelength of tungsten (W).

#### A.1.4. XPS Measurements

XPS measurements have been performed on all films using a Kratos Axis Supra spectrometer with a monochromatic Al K<sub>α</sub> source. The overview spectrum (see fig. A.4 (left)) in the binding energy range of 750 eV – 0 eV was obtained with a pass energy of 40 eV and 0.1 eV step size. Higher resolution spectra of the F1s, Mn2p, Mn3p and C1s transitions were acquired with a pass energy of 20 eV and step size 0.1 eV. In addition, an enlarged section of the spectrum is shown on the right, in which the Mn2p and the F1s peak are more clearly visible (see fig. A.4 (right)). The binding energy scale has been corrected by shifting the C1s main peak energy to 284.8 eV. Element ratios were calculated by peak intensity ratios after Shirley-background subtraction and transmission correction using the instrument-specific relative sensitivity factors.

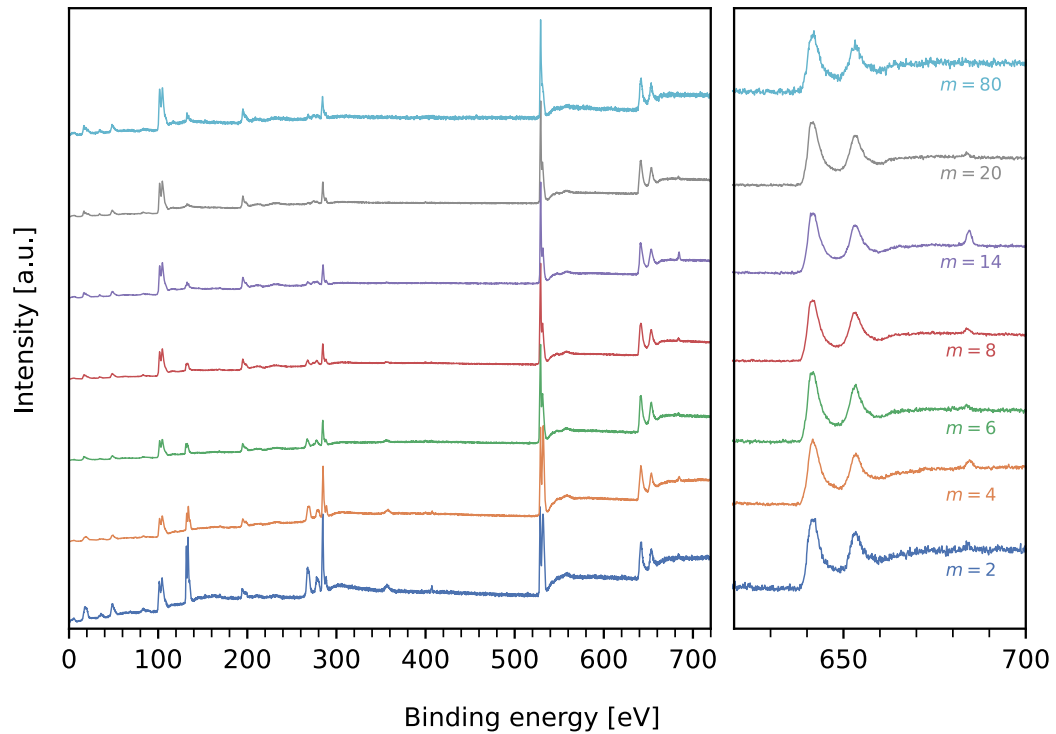


**Figure A.4:** XPS spectra in a binding energy range of 0 to 750 eV. The figure on the right shows an enlargement of the left figure, in which the Mn2p peaks and the F1s peak are more clearly visible.

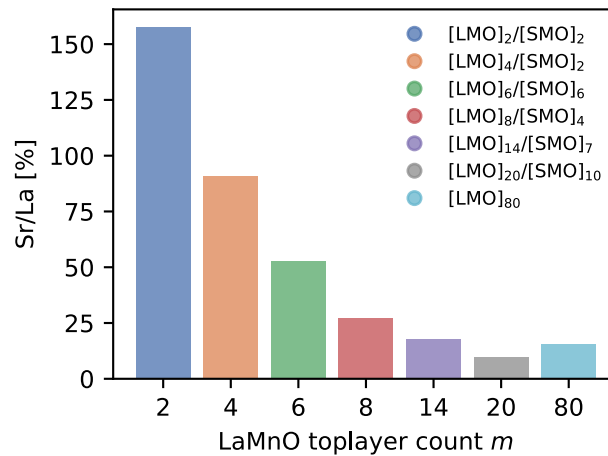


**Figure A.5:** The Sr/La concentration ratio decreases exponentially with increasing LaMnO<sub>3</sub> toplayer thickness due to the exponential decay of information intensity with depth.

The overview spectra are consistent with a [LaMnO<sub>3</sub>]<sub>m</sub>/[SrMnO<sub>3</sub>]<sub>n</sub> layered system. A plot of the Sr/La ratio (fig. A.5) shows that the relative strontium signal decreases as expected

exponentially with increasing  $\text{LaMnO}_3$  top layer thickness due to surface sensitivity of XPS measurements. The inelastic mean free path of the excited  $e^-$  is  $\lambda = 2.3$  nm in the multilayer system<sup>[221,222]</sup> The Sr/La ratio of 160% for the 2/2-superlattice can be explained by considering the interface roughness of the superlattice. Assuming a local  $\text{LaMnO}_3$  top layer thickness of 1 and a  $\text{SrMnO}_3$  layer thickness of 3, a Sr/La ratio of 160% is expected according to the lambert beer intensity decay with depth and the calculated IMFP of 2.3 nm.

### A.1.5. Thermal Resistivity Values

The thermal properties of the films studied here were determined using the results of previous studies<sup>[117,187]</sup>, which were obtained from thermal transient reflectometry (TTR) measurements on films prepared in the same system with equal or similar  $m$  to  $n$  ratios. The  $m$  to  $n$  ratio can be translated into a unitless interface density  $c/\Lambda$  from an effective unit cell thickness  $c$  and the superlattice period  $\Lambda = m + n$ . The estimated values used in this work for thermal resistivity are shown in fig. A.7, along with the values from films investigated in the literature.<sup>[223]</sup> Further details about the linear model and the two trend lines, depending on the  $m/n$ -ratio, can be found in<sup>[117]</sup>.

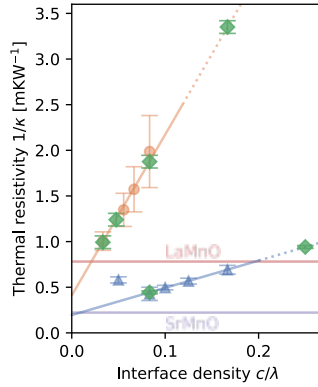


**Figure A.6:** TTR measurements by D. Meyer et al.<sup>[117]</sup> reveal scaling between thermal properties and interface density  $c/\lambda = 1/(m + n)$  depending on the  $m/n$  ratio. The data, provided by the authors (orange circles and blue triangles), was used to estimate the thermal resistivity for the samples studied in this work (green diamonds).

### A.1.6. Magnetic Measurements

To examine the stoichiometry and interface charge transfer, the magnetic moment was measured using a Quantum Design MPMS-XL magnetometer (SQUID). fig. A.7 depicts the tem-

$c/\Lambda$	$m$	$n$	$1/\kappa$ [mK W <sup>-1</sup> ]
0.25	2	2	0.91(2)
0.166	4	2	3.27(7)
0.083	6	6	0.43(2)
0.083	8	4	1.84(7)
0.048	14	7	1.23(7)
0.033	20	10	0.99(7)
—	80	0	0.77(7)

**Table A.3:** Estimates of thermal resistivity  $1/\kappa$  for the superlattice samples, based on TTR measurements.<sup>[117]</sup>

perature dependent magnetization of the samples. The 32 nm thick LaMnO<sub>3</sub> thin film is ferromagnetic with Curie-temperature  $T_C = 152$  K which is expected for stoichiometric LaMnO<sub>3</sub> due to the epitaxial strain from the SrTiO<sub>3</sub>: 1.0 at. % Nb substrate.<sup>[223]</sup> For the superlattices, the electron transfer between up to 3 unit cells at the [LaMnO<sub>3</sub>]<sub>m</sub>/[SrMnO<sub>3</sub>]<sub>n</sub> interface leads to magnetic properties similar to randomly ordered La<sub>m/(m+n)</sub>Sr<sub>n/(m+n)</sub>MnO<sub>3</sub>, which is the optimally doped La<sub>2/3</sub>Sr<sub>1/3</sub>MnO<sub>3</sub> with  $T_C \approx 350$  K for the [LaMnO<sub>3</sub>]<sub>2n</sub>/[SrMnO<sub>3</sub>]<sub>n</sub> superlattices and the antiferromagnetic La<sub>0.5</sub>Sr<sub>0.5</sub>MnO<sub>3</sub> for the [LaMnO<sub>3</sub>]<sub>m</sub>/[SrMnO<sub>3</sub>]<sub>n</sub> series.<sup>[224]</sup> With increasing layer thickness, the magnetic properties gradually change to those of the ferromagnetic bulk LaMnO<sub>3</sub> and antiferromagnetic SrMnO<sub>3</sub> shown by the decrease in saturation magnetization and increasing conductivity with increasing SrMnO<sub>3</sub> thickness in the case of the [LaMnO<sub>3</sub>]<sub>2n</sub>/[SrMnO<sub>3</sub>]<sub>n</sub> samples (figs. A.7 and A.8). Therefore, the magnetic properties also support smooth interfaces without intermixing. Overall, the magnetic properties are in line with those known for MAD grown [LaMnO<sub>3</sub>]<sub>2n</sub>/[SrMnO<sub>3</sub>]<sub>n</sub> superlattices along with the high- $T_C$  interfacial magnetic phase, giving further justification to using the thermal resistivity values from D. Meyer et al.<sup>[117]</sup>

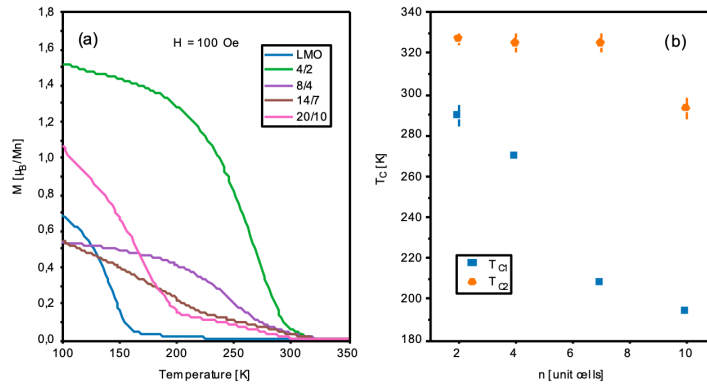


**Figure A.7:**  $M(T)$  curves of the  $[LaMnO_3]_m/[SrMnO_3]_n$  samples with  $m = 2n$  at an external field of 100 Oe (a) and Curie-temperatures  $T_{C1}$  of "bulk" and  $T_{C2}$  of the interfacial phase as a function of  $SrMnO_3$  layer thickness.

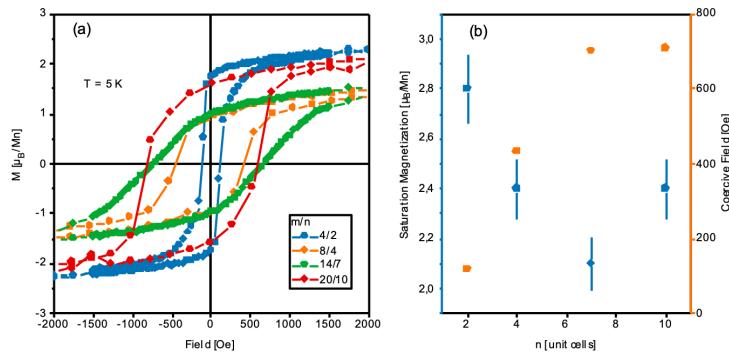


**Figure A.8:** Magnetic hysteresis of the  $[LaMnO_3]_m/[SrMnO_3]_n$  with  $m = 2n$  at  $T = 5$  K (a) and change of saturation magnetization at  $B_{ext} = 5$  T and co-active field with  $SrMnO_3$  thickness  $n$  (b).

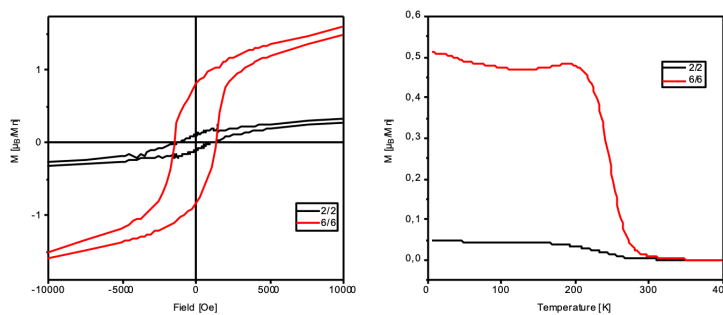
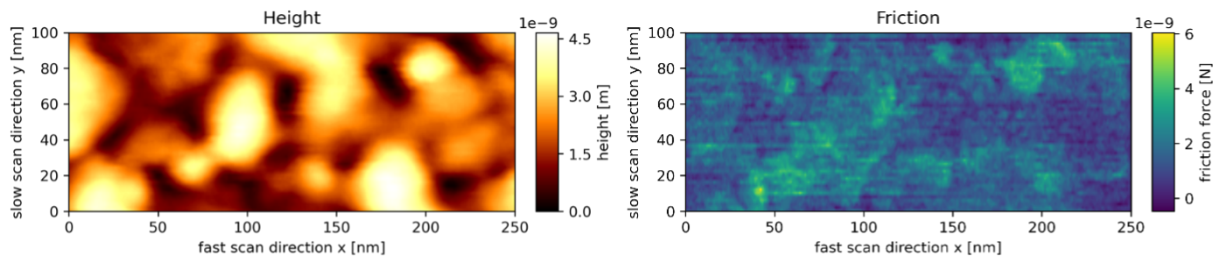


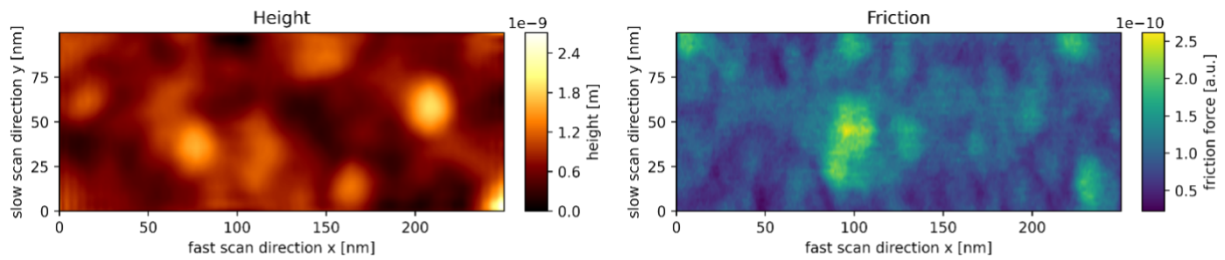
**Figure A.9:** Magnetic properties of the superlattices with periodicity  $m = n$ : hysteresis at  $T = 5$  K (left) and field cooled magnetization at  $H = 100$  Oe (right).

## A.2. SI - Topography and Friction Maps

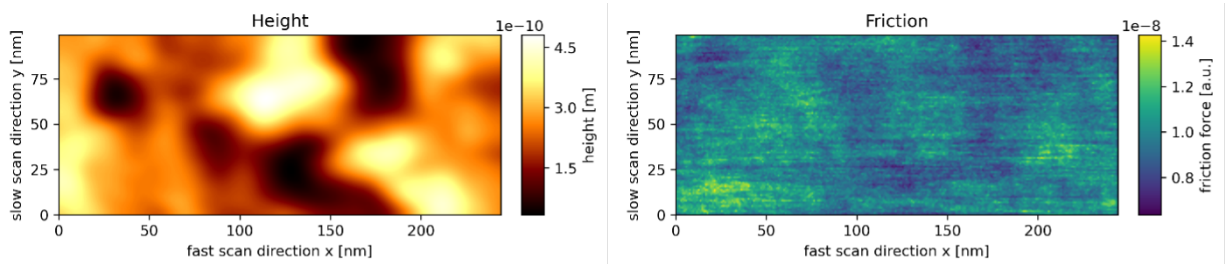
Figure A.10 depicts a representative topography and corresponding friction map for all the seven  $[\text{LaMnO}_3]_m/[\text{SrMnO}_3]_n$  films studied. All maps were measured at room temperature under UHV conditions using an Omicron VT-AFM. The surface roughness  $RMS \leq 0.5$  nm is in good agreement with the XRR measurements (see appendix A.1.3). We observe low correlations ( $r_S < 0.15$ ) between the friction force and the height and height gradient maps. All films show local variations in the friction force on a length scale of about 50 nm.



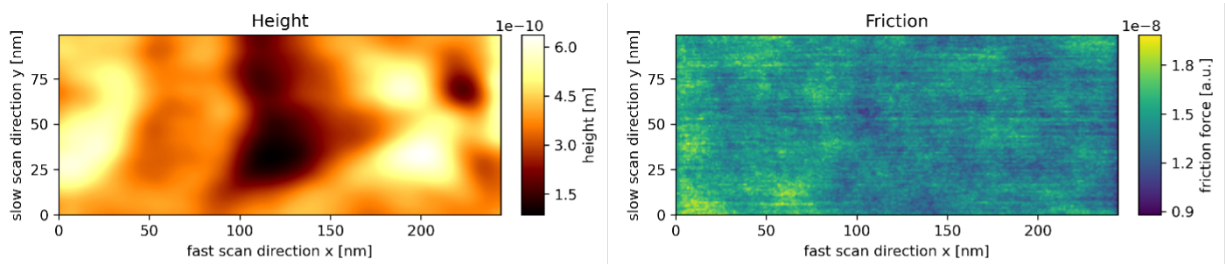
(a) Topography (left) and corresponding friction map (right) of  $[\text{LaMnO}_3]_2/[\text{SrMnO}_3]_2$



(b) Topography (left) and corresponding friction map (right) of  $[\text{LaMnO}_3]_4/[\text{SrMnO}_3]_2$



(c) Topography (left) and corresponding friction map (right) of  $[\text{LaMnO}_3]_6/[\text{SrMnO}_3]_6$



(d) Topography (left) and corresponding friction map (right) of  $[\text{LaMnO}_3]_8/[\text{SrMnO}_3]_4$

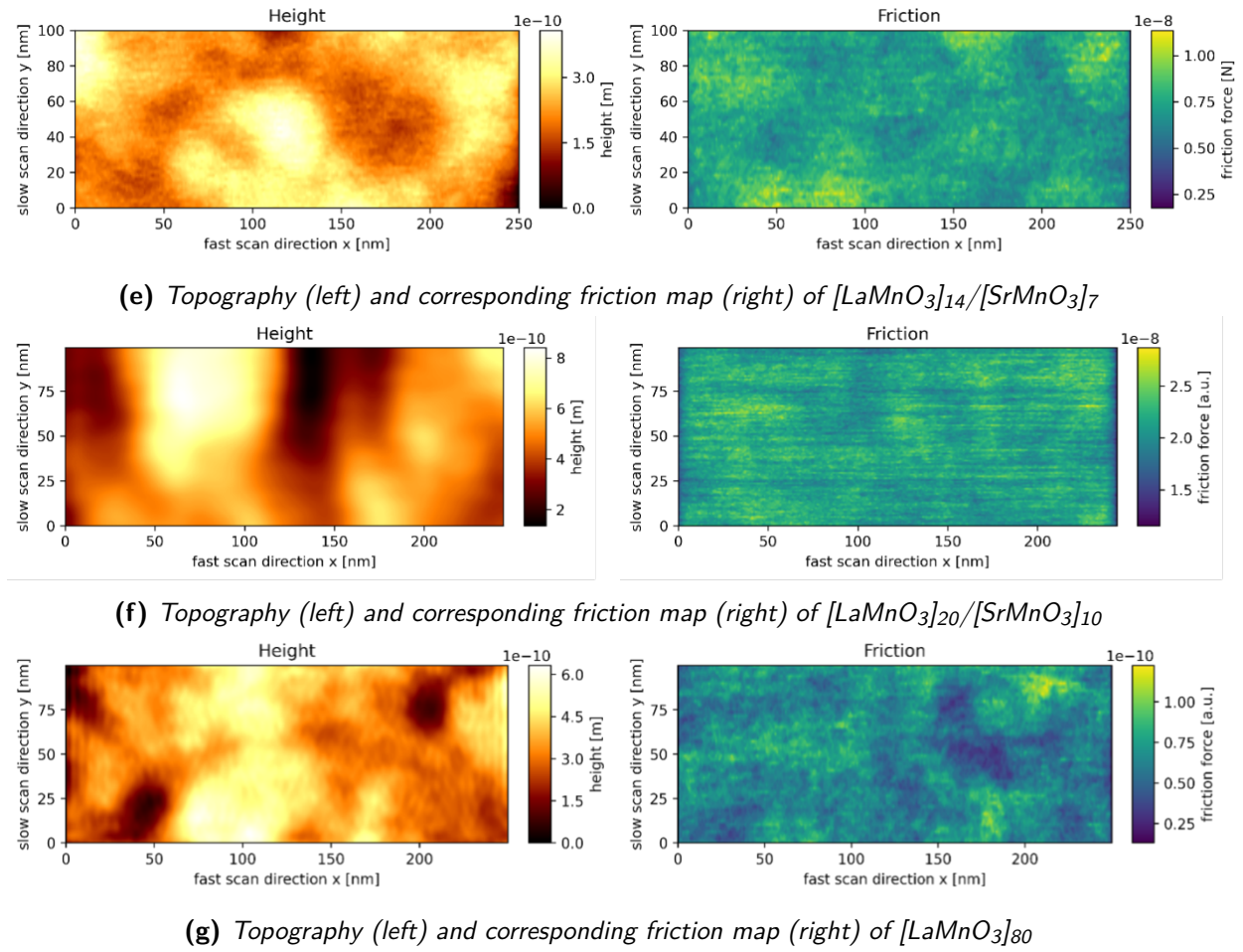


**Figure A.10:** Topography and friction map, calculated from lateral traces, of the seven superlattice samples studied in this manuscript. All samples, regardless of the  $m/n$  ratio, show comparable surfaces with a roughness  $RMS < 0.5$  nm, and low correlation coefficients  $r_s < 1.5$  between the friction and the height maps.

### A.3. SI - Friction versus Normal Force Measurements

#### A.3.1. Friction Force as a Function of Applied Normal Force

The seven plots below (see fig. A.11) show the results of the friction force versus normal force measurements on all seven  $[\text{LaMnO}_3]_m/[\text{SrMnO}_3]_n$  superlattice films. Here, the different point styles indicate different series of measurements on different locations of the sample surface.

Each measurement set was performed within a map (100 nm by 250 nm) and the friction forces recorded as the normal force was increased from the initial value and then reduced back to the initial value to check for any changes in tip shape. Independent of the location of the measurement, a linear dependence between the frictional force and the applied normal force can be observed for all films. In contrast, the magnitudes of the measured forces vary strongly from map to map, presumably due to small changes in surface chemistry and/or variations in top layer thickness (see fig. A.11). Occasional larger shifts in friction forces ( $\pm 10$  nN) are sometimes observed when comparing different measurements made with different cantilevers and are attributed to changes in tip shape.

Linear regressions were performed on each dataset individually, using a modified Amontons relationship<sup>[53]</sup>

$$F_F = \mu \cdot F_N + F_{F0}. \quad (\text{A.1})$$

The friction coefficients or slopes  $\mu$  of the friction force vs applied normal force data are very similar for all of the maps for a given superlattice film, while the y-axis intercept  $F_{F0}$  varies strongly from map to map. The friction coefficients of the films not strongly doped with fluorine show a clear dependence increase and saturate with the top  $\text{LaMnO}_3$  layer thickness (see fig. A.12). The two fluorine doped samples  $m = 4, 14$  show significantly lower friction coefficients. In contrast, no correlation of the zero intercept  $F_{F0}$  with the film thickness or other material properties can be observed (see fig. A.12(right)).

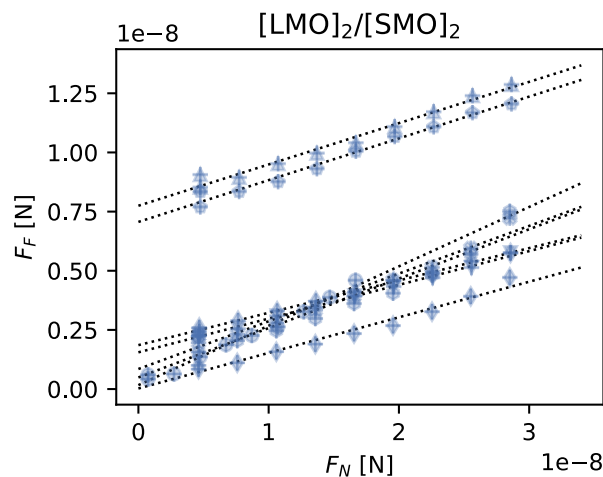


**Figure A.11:** *Caption on next page.*

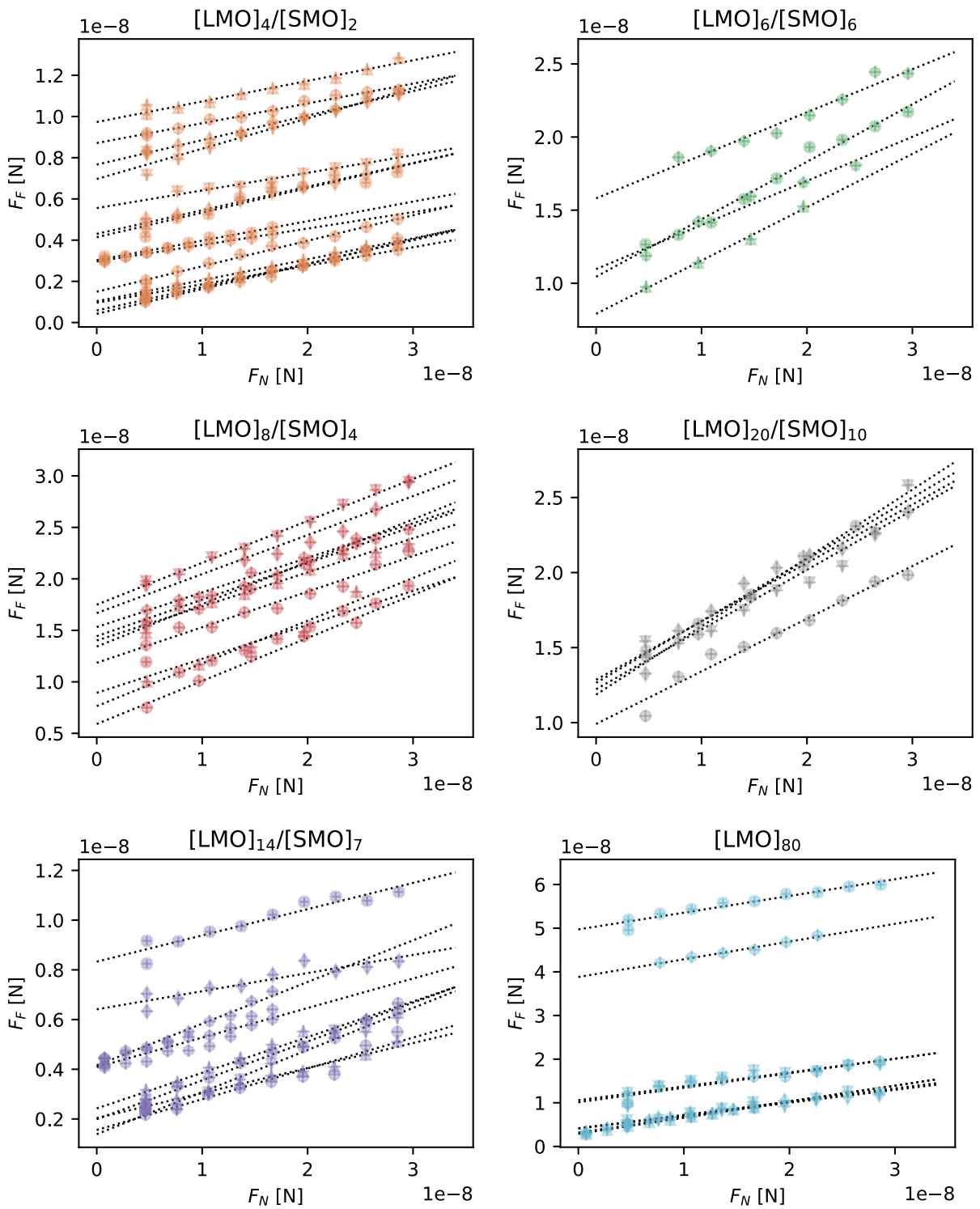


**Figure A.11:** Friction forces versus applied normal force for all superlattice films. Each dataset corresponds to the average of a single lateral force map ( $100 \text{ nm} \times 250 \text{ nm}$ ).

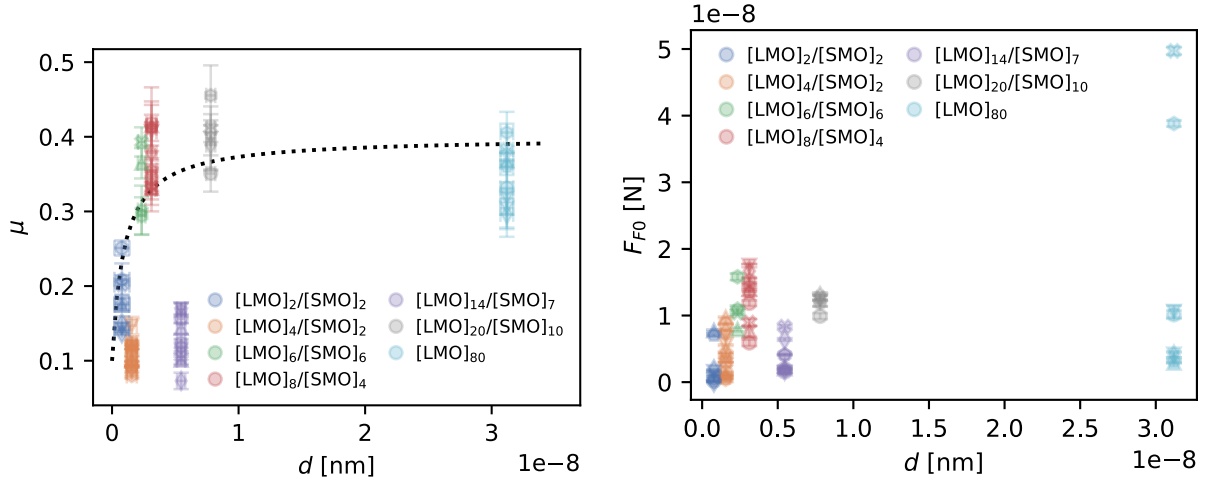


**Figure A.12:** Friction coefficient  $\mu$  (left) and friction force at zero applied normal force  $F_{F0}$  (right) plotted against the LaMnO top layer thickness for each individual Amontons measurement (see fig. A.11). The two fluorine doped samples  $m=4$  and  $m=14$  show much smaller coefficients that we attribute to an altered surface chemistry.

### A.3.2. Correlation between $F_{F0}/\mu$ and Adhesion

Contact models such as the DMT and JKR model<sup>[24,48]</sup> postulate that the friction force becomes zero when the applied force cancels the adhesive forces. This means that the value  $F_{F0}/\mu$ , which is the magnitude of the applied force at which the friction forces extrapolate to zero, should be similar in magnitude to the adhesion force, which can be obtained from the pull-off measurements (force-distance curves). The two forces are compared in the plot below. The good agreement between the two quantities supports the idea that adhesive forces are the cause of the offset in friction force  $F_{F0}$ .

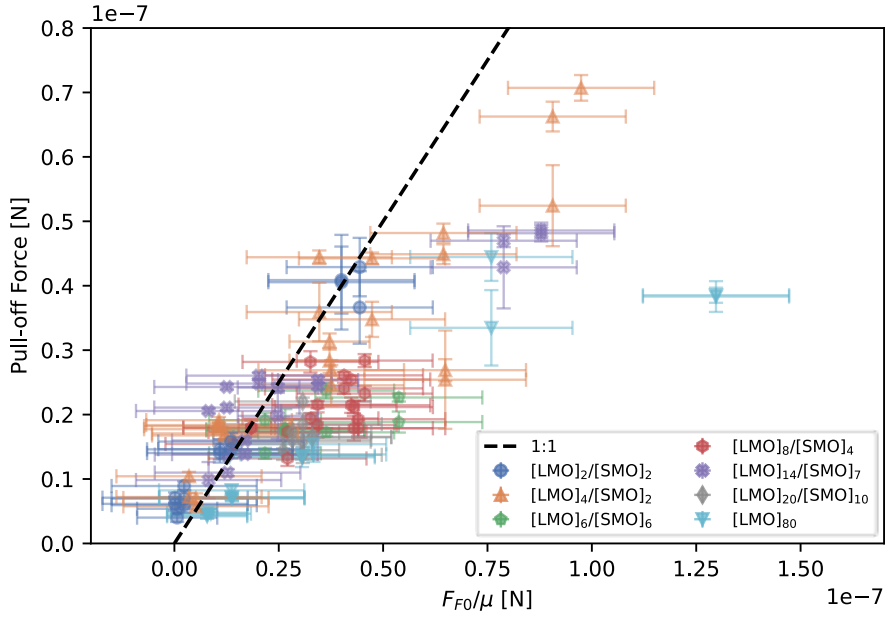


**Figure A.13:** Pull-off forces obtained from force distance measurements versus the  $F_{F0}/\mu$  obtained in the appendix A.3.2. The dashed line indicates where the two quantities are equal.

### A.3.3. Friction Force as a Function of $(F_N + F_{F0})/\mu$

The good agreement between the pull-off force and the applied force at zero friction suggests that adhesion forces are the cause of the shift in the frictional force  $F_{F0}$ . Adding this adhesive force  $F_{F0}/\mu$  to the applied normal force  $F_N$  collapses the friction measurements presented in appendix A.3.1 onto a common linear master curve for each superlattice film. The slopes of these curves are referred to as average friction coefficients  $\bar{\mu}$  in the manuscript and increases continuously up to a LaMnO<sub>3</sub> top layer thickness of  $d = 8 - 10$  nm, after which a saturation to a bulk friction coefficient is observed.

The seven plots (see fig. A.15) below show the collapse of the friction data to a single master curve for each superlattice film. fig. A.16 depicts the average friction coefficients  $\bar{\mu}$  as a function of LaMnO<sub>3</sub> top layer thickness. The friction coefficients initially increase, with increasing LaMnO<sub>3</sub>-thickness, and saturate at a film thickness of 5 – 8 nm to a bulk value.

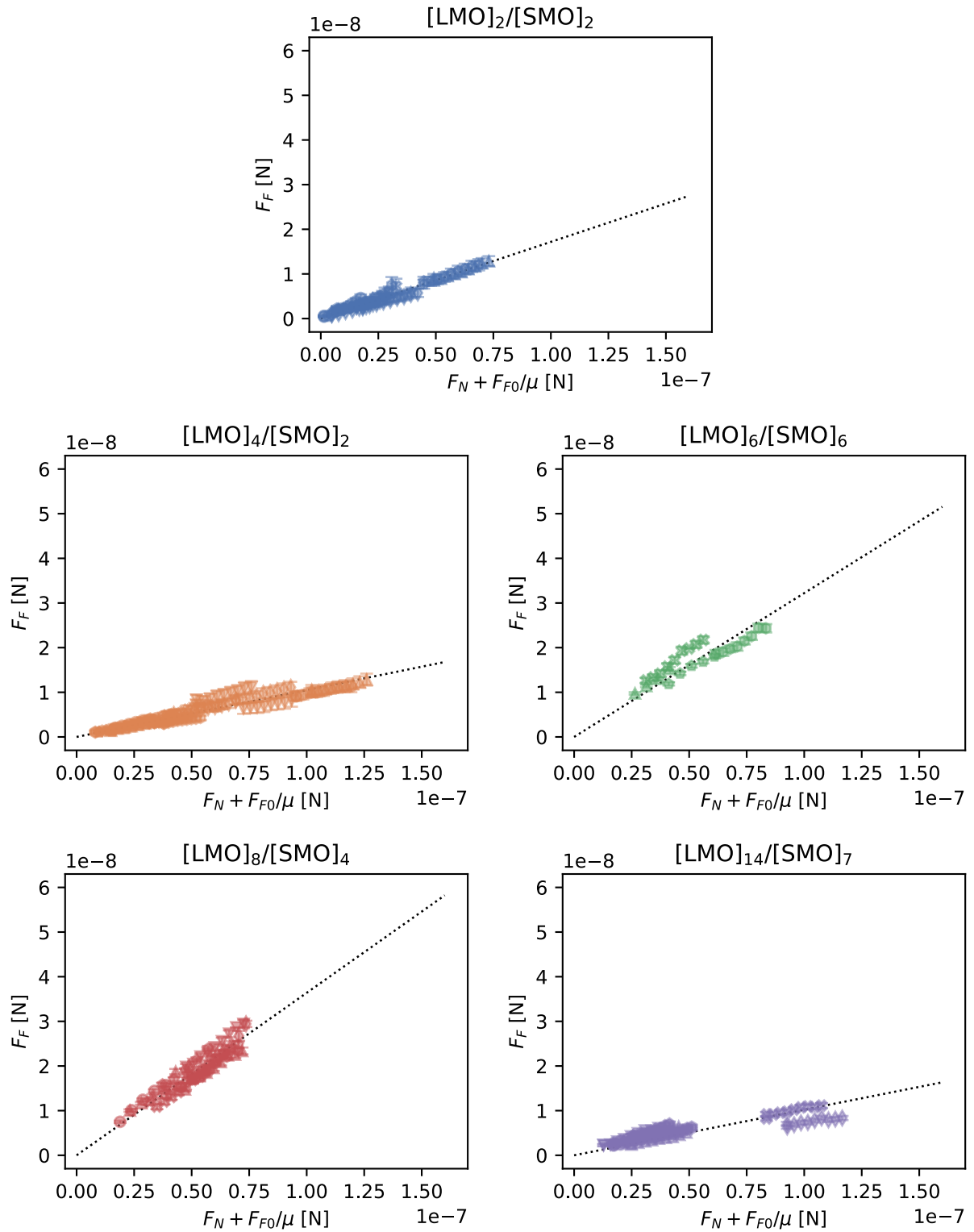
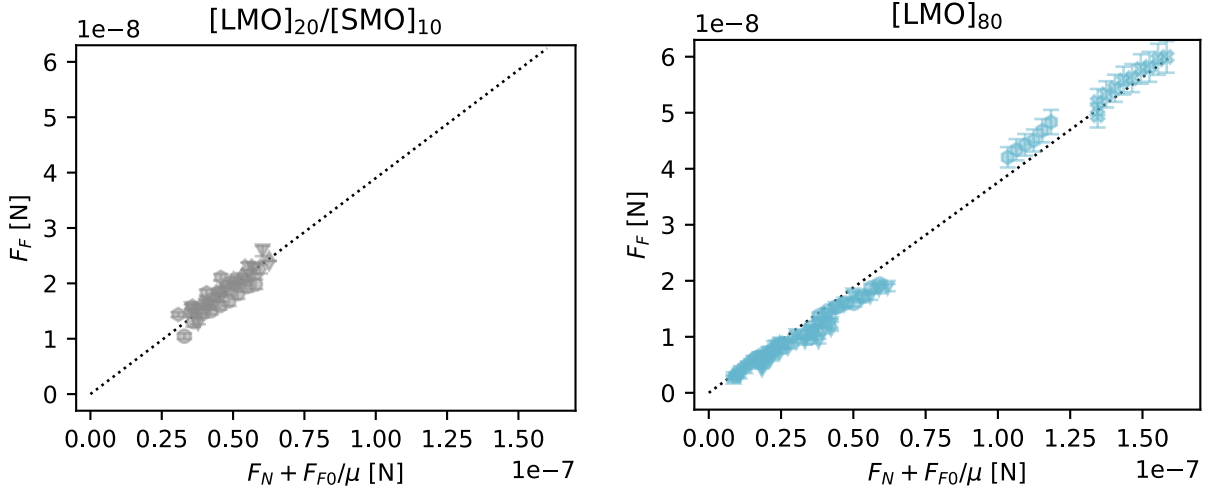
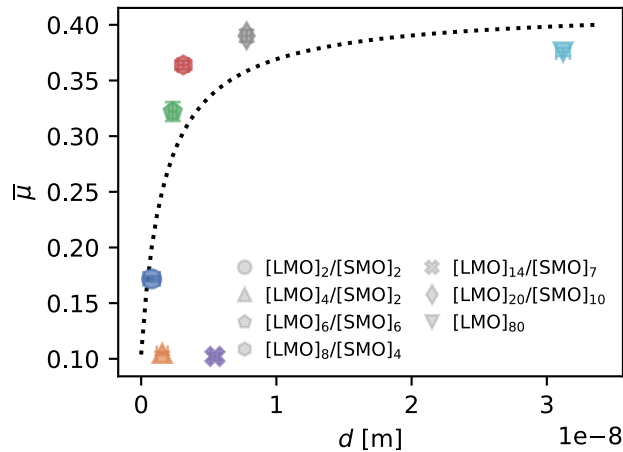


Figure A.14: Caption on next page.



**Figure A.14:** Friction forces, versus  $F_N + F_{F0}/\mu$ . Each dataset corresponds to the average of a single lateral force map ( $100 \text{ nm} \times 250 \text{ nm}$ ). The dashed line shows a linear fit. The slopes obtained from linear regressions ( $\bar{\mu}$ ) are depicted in fig. A.15.



**Figure A.15:** Slopes  $\bar{\mu}$  obtained from linear fitting of the data shown in fig. A.14 as a function of  $\text{LaMnO}_3$  top layer thickness. Friction coefficients initially increase with increasing top layer thickness and saturate after the film thickness exceeds 5–8 nm. The fluorine dope samples  $m=4$  and  $m=14$  show much smaller friction coefficients compared to sample with similar top layer thickness, that we attribute to an altered surface chemistry.

### A.3.4. Master Equation Top Layer Thickness Dependency

The functional form of  $g(d/a)$  used in eq. 5.8 of the manuscript was determined by looking for possible scaling between friction force and  $\text{LaMnO}_3$  top layer thickness. Plotting  $(F_F - F_{F0})/F_N$  versus  $d/a$  revealed that the measured friction forces collapse onto a single master curve

irrespective of the film. This master curve can be reasonably well approximated by a functional form  $g(d/a) = d/(d+a)$  an equation that also provides a good fit to the integrated stress fields under a spherical tip<sup>[30,40]</sup> (see appendix A.4). In addition, the functional form is in quantitative agreement with a viscoelastic model developed by Lee et al.<sup>[3]</sup>, which attributes top layer thickness dependent friction to viscous dissipation inside the evanescent waves set up in the top layer by a vibrating tip.

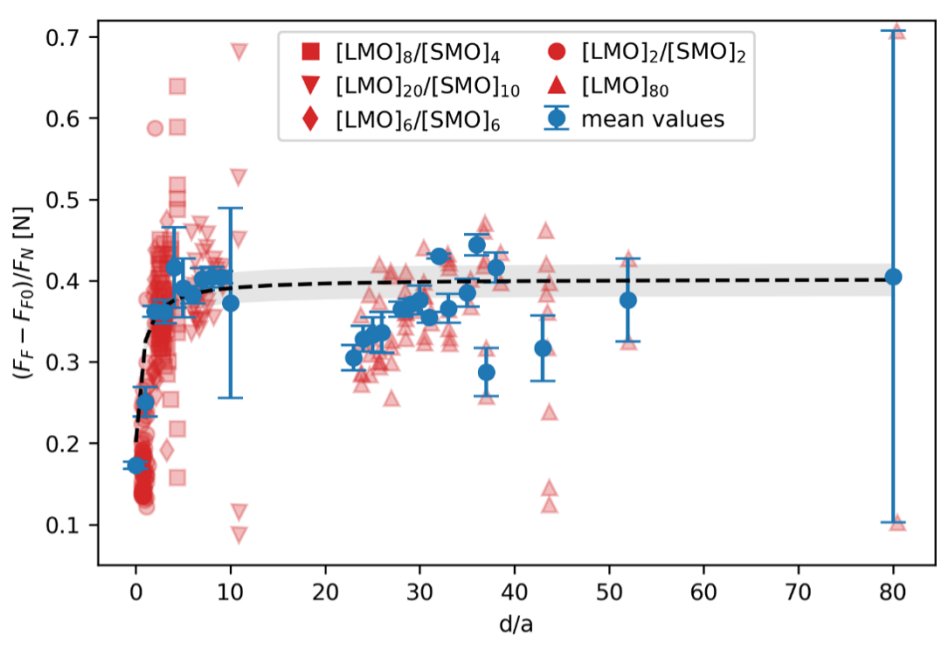


**Figure A.16:** Plotting  $(F_F - F_{F0})/F_N$  versus  $d/a$  revealed that the measured friction forces collapse onto a single master curve. This master curve can be reasonably well approximated by a functional form  $g(d/a) = d/(d+a)$ .

## A.4. SI - Elastically Strained Volume

An AFM tip in contact with a flat sample surface produces stress fields in the underlying material. Even for nano newton normal loads, the stresses under the tip can reach 100 GPa values. However, there is no evidence of plasticity or fracture so that the material is assumed to respond elastically. Assuming a spherical tip shape, the indentation depth  $d$  can be estimated by using the Hertz contact model:<sup>[30]</sup>

$$d = \frac{a^2}{R} = \left( \frac{9F_N^2}{16E^*R} \right)^{1/3}.$$

The indentation depth  $d$ , in case of elastic deformation of the surface, is proportional to  $a^2$  the interaction area,  $R$  the radius of the tip,  $E^*$  elastic properties of the materials in contact and the applied normal force  $F_N$ .

Due to this indentation, a heterogeneous stress field is generated in the underlying material. The exact shape of the stress field depends on the shape of the indenter, the applied normal force, and the elastic properties of the materials. If we again assume a simplified spherical shape of the tip, the stress field under the tip can be calculated using the equation<sup>[40]</sup>

$$\sigma_{zr} = 3 p_m (1 + \nu) \frac{z}{\sqrt{u}} \left[ \frac{\sqrt{u}}{a} \tan^{-1} \left( \frac{a}{\sqrt{u}} \right) - 1 \right]$$

here  $u = 1/2[(r^2 + z^2 - a^2) + ((r^2 + z^2 - a^2)^2 + 4a^2z^2)^{1/2}]$ ,  $p_m = F_N/\pi a^2$  the contact pressure and  $\nu$  the Poisson's ratio. The stress fields calculated in this way are long-range and decay radially and in depth only after a few nanometers (see fig. A.17).

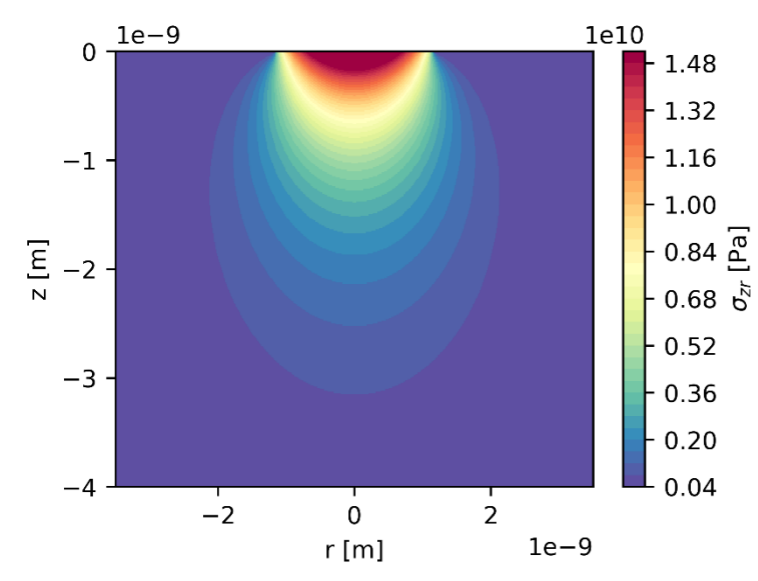


**Figure A.17:** Stress field generated below a spherical indenter. For the illustration, experimentally reasonable values of  $F_N = 20$  nN,  $R = 10$  nm,  $E^* = 95$  GPa and  $\nu = 0.35$  were used.

The integrated stress under the tip can be estimated by numerically integrating out to a radius where the stress falls below 10 GPa and then integrating along the  $z$  direction (see fig. A.10). The integrated stress under an AFM tip is well described by the function  $g(z) = b \cdot (z/(z + a_H))$ , where  $b$  corresponds to a scaling factor and  $a_H$  to an interaction radius that can be estimated from Hertz contact model.<sup>[30]</sup>

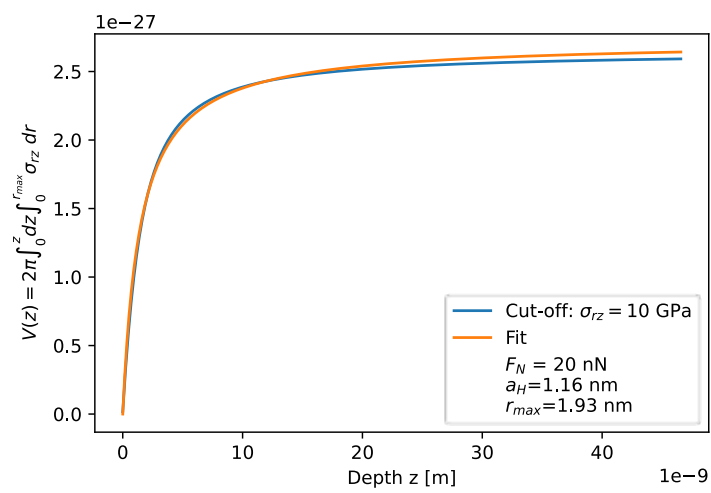


**Figure A.18:** Integrated stress under an AFM tip. Stresses were integrated out to a distance where the values fall below 10 GPa. The function  $g(z) = b \cdot (z/(z + a_H))$  fits the integrated stress reasonably well.



# Bibliography

- [1] H. Schmidt, J. O. Krisponeit, N. Weber, K. Samwer, and C. A. Volkert, [Physical Review Materials](#) **4**, 113610 (2020).
- [2] N. A. Weber, H. Schmidt, T. Sievert, C. Jooss, F. Güthoff, V. Moshneaga, K. Samwer, M. Krüger, and C. A. Volkert, [Advanced Science](#) **2003524** (2020), [10.1002/advs.202003524](#).
- [3] M. Lee, N. Weber, C. A. Volkert, and M. Krüger, [pre-print](#) (2022), [arXiv:2205.01151](#) .
- [4] N. A. Weber, M. Lee, F. Schönwald, L. Schüler, V. Moshnyaga, M. Krüger, and C. A. Volkert, [pre-print](#) (2022), [arXiv:2210.09677](#) .
- [5] N. Goren-Inbar, M. Freikman, Y. Garfinkel, N. A. Goring-Morris, and L. Grosman, [PLoS One](#) **7**, e42213 (2012).
- [6] P. E. Newberry, *The tomb of Tehuti-Hetep*, Vol. 1 (Egypt Exploration Society, 1893).
- [7] T. K. Cheyne and J. S. Black, *Encyclopaedia Biblica; a Critical Dictionary of the Literary, Political and Religious History, the Archaeology, Geography and Natural History of the Bible*, Vol. 2 (The Macmillan Company, 1901).
- [8] A. Fall, B. Weber, M. Pakpour, N. Lenoir, N. Shahidzadeh, J. Fiscina, C. Wagner, and D. Bonn, [Physical Review Letters](#) **112**, 175502 (2014).
- [9] E. Popova and V. L. Popov, [Friction](#) **3**, 183 (2015).
- [10] K. Holmberg and A. Erdemir, [Friction](#) **5**, 263 (2017).
- [11] H. Schmidt, *Nanotribologische Untersuchungen an Dünnschicht-Manganaten: Phononische Beiträge zur Reibung auf der Nanometerskala*, [Ph.D. thesis](#), Georg-August-Universität Göttingen (2018).

- [12] V. M. Pfahl, *Reibung kristalliner, amorpher und stark korrelierter Systeme unter aktiver Kontrolle*, Ph.D. thesis, Georg-August-Universität Göttingen (2018).
- [13] R. L. C. Vink, *Phys. Rev. B* **100**, 094305 (2019).
- [14] W. Wang, D. Dietzel, and A. Schirmeisen, *Science Advances* **6**, eaay0165 (2020).
- [15] Y. Qi, J. Y. Park, B. L. M. Hendriksen, D. F. Ogletree, and M. Salmeron, *Physical Review B* **77**, 184105 (2008).
- [16] I. Altfeder and J. Krim, *Journal of Applied Physics* **111**, 094916 (2012).
- [17] M. Kisiel, E. Gnecco, U. Gysin, L. Marot, S. Rast, and E. Meyer, *Nature Materials* **10**, 119 (2011).
- [18] T. A. L. Burgo, C. A. Silva, L. B. S. Balestrin, and F. Galembeck, *Scientific Reports* **3**, 2384 (2013).
- [19] B. Shi, X. Gan, C. Zhang, H. Lang, K. Zou, T. Bu, and Y. Peng, *Nano Energy* **91**, 106620 (2022).
- [20] A. Dayo, W. Alnasrallah, and J. Krim, *Physical Review Letters* **80**, 1690 (1998).
- [21] A. Liebsch, S. Gonçalves, and M. Kiwi, *Physical Review B* **60**, 5034 (1999).
- [22] B. Persson and A. Nitzan, *Surface Science* **367**, 261 (1996).
- [23] M. S. Tomassone, J. B. Sokoloff, A. Widom, and J. Krim, *Physical Review Letters* **79**, 4798 (1997).
- [24] J. Y. Park and M. Salmeron, *Chem. Rev.* **114**, 677 (2014).
- [25] F. P. Bowden and D. Tabor, *Proceedings of the Royal Society of London. Series A. Mathematical and Physical Sciences* **169**, 391 (1939).
- [26] B. Bhushan, *Springer Handbook of Nanotechnology*, edited by B. Bhushan (Springer Berlin Heidelberg, 2017) p. 1500.
- [27] W. Richtering, *Applied Rheology* **14**, 10 (2004).
- [28] J. N. Israelachvili and D. Tabor, *Proc. R. Soc. London. A. Math. Phys. Sci.* **331**, 19 (1972).

- 
- [29] J. N. Israelachvili and D. Tabor, *Nat. Phys. Sci.* 1973 241112 **241**, 148 (1973).
- [30] H. Hertz, *Journal fur die Reine und Angewandte Mathematik* **1882**, 156 (1882).
- [31] J. K. Langstreth, K. Kendall, and A. Roberts, *Proceedings of the Royal Society of London. A. Mathematical and Physical Sciences* **324**, 301 (1971).
- [32] B. Persson and E. Tosatti, *Physics of sliding friction*, edited by B. Persson and E. Tosatti, Vol. 311 (Springer Science & Business Media, 2013).
- [33] B. Derjaguin, V. Muller, and Y. Toporov, *Journal of Colloid and Interface Science* **53**, 314 (1975).
- [34] D. Maugis, *J. Colloid Interface Sci.* **150**, 243 (1992).
- [35] R. W. Carpick, D. Ogletree, and M. Salmeron, *J. Colloid Interface Sci.* **211**, 395 (1999).
- [36] U. Schwarz, *J. Colloid Interface Sci.* **261**, 99 (2003).
- [37] J. A. Greenwood and W. B. P., *Proc. R. Soc. London. Ser. A. Math. Phys. Sci.* **295**, 300 (1966).
- [38] B. Persson, *J. Chem. Phys.* **115**, 3840 (2001).
- [39] M. H. Müser, *Phys. Rev. Lett.* **100**, 055504 (2008).
- [40] A. C. Fischer-Cripps, *Introduction to Contact Mechanics*, 2nd ed., Mechanical Engineering Series (Springer US, Boston, MA, 2007).
- [41] G. Pitarresi and E. A. Patterson, *J. Strain Anal. Eng. Des.* **38**, 405 (2003).
- [42] B. M. Law and F. Rieutord, *Physical Review B* **66**, 035402 (2002).
- [43] S. Hudlet, M. S. Jean, C. Guthmann, and J. Berger, *The European Physical Journal B* **2**, 5 (1998).
- [44] B. Bhushan, *Nanotribology and Nanomechanics II: Nanotribology, Biomimetics, and Industrial Applications*, Vol. 1 (Springer Science & Business Media, 2011) p. 1017.
- [45] Q. J. Wang and Y.-W. Chung, *Encyclopedia of Tribology*, edited by Q. J. Wang and Y.-W. Chung (Springer US, Boston, MA, 2013).
- [46] H. Hamaker, *Physica* **4**, 1058 (1937).

- [47] F. J. Giessibl, *Rev. Mod. Phys.* **75**, 949 (2003), [arXiv:0305119 \[cond-mat\]](#) .
- [48] G. G. Adams, in *Encycl. Tribol.* (Springer US, Boston, MA, 2013) pp. 3560–3565.
- [49] U. D. Schwarz, O. Zwörner, P. Köster, and R. Wiesendanger, *Physical Review B* **56**, 6997 (1997).
- [50] T. Stifter, O. Marti, and B. Bhushan, *Phys. Rev. B* **62**, 13667 (2000).
- [51] L. Prandtl, *ZAMM - Zeitschrift für Angewandte Mathematik und Mechanik* **8**, 85 (1928).
- [52] G. Tomlinson, *The London, Edinburgh, and Dublin Philosophical Magazine and Journal of Science* **7**, 905 (1929).
- [53] E. Gnecco and E. Meyer, *Fundamentals of Friction and Wear on the Nanoscale*, edited by E. Gnecco and E. Meyer (Springer International Publishing, 2015) pp. 157–173.
- [54] A. Vanossi, N. Manini, M. Urbakh, S. Zapperi, and E. Tosatti, *Reviews of Modern Physics* **85**, 529 (2013).
- [55] Y. Dong, A. Vadakkepatt, and A. Martini, *Tribol. Lett.* **44**, 367 (2011).
- [56] A. Socoliuc, R. Bennewitz, E. Gnecco, and E. Meyer, *Physical review letters* **92**, 134301 (2004).
- [57] O. Ben-David, S. M. Rubinstein, and J. Fineberg, *Nature* **463**, 76 (2010).
- [58] S. Fujisawa, Y. Sugawara, S. Ito, S. Mishima, T. Okada, and S. Morita, *Nanotechnology* **4**, 138 (1993).
- [59] C. M. Mate, G. M. McClelland, R. Erlandsson, and S. Chiang, *Atomic-scale friction of a tungsten tip on a graphite surface*, Vol. 59 (Springer, 1987) pp. 226–229.
- [60] T. Baumberger and C. Caroli, *Advances in Physics* **55**, 279 (2006).
- [61] Y. Dong, Q. Li, and A. Martini, *Journal of Vacuum Science & Technology A: Vacuum, Surfaces, and Films* **31**, 030801 (2013).
- [62] X. Lu, N. Lapusta, and A. J. Rosakis, *Proc. Natl. Acad. Sci.* **104**, 18931 (2007).
- [63] S. N. Medyanik, W. K. Liu, I.-H. Sung, and R. W. Carpick, *Physical Review Letters* **97**, 136106 (2006).

- 
- [64] E. Gnecco, R. Bennewitz, T. Gyalog, C. Loppacher, M. Bammerlin, E. Meyer, and H.-J. Güntherodt, *Physical Review Letters* **84**, 1172 (2000).
- [65] Y. Sang, M. Dubé, and M. Grant, *Physical Review Letters* **87**, 174301 (2001).
- [66] O. Dudko, A. Filippov, J. Klafter, and M. Urbakh, *Chemical Physics Letters* **352**, 499 (2002).
- [67] E. Riedo, E. Gnecco, R. Bennewitz, E. Meyer, and H. Brune, *Physical Review Letters* **91**, 084502 (2003).
- [68] P. Reimann and M. Evstigneev, *Physical Review Letters* **93**, 230802 (2004).
- [69] S. Y. Krylov, K. B. Jinesh, H. Valk, M. Dienwiebel, and J. W. M. Frenken, *Physical Review E* **71**, 065101 (2005).
- [70] L. Jansen, H. Hölscher, H. Fuchs, and A. Schirmeisen, *Physical Review Letters* **104**, 256101 (2010).
- [71] A. Schirmeisen, L. Jansen, H. Hölscher, and H. Fuchs, *Applied Physics Letters* **88**, 123108 (2006).
- [72] Y. Dong, A. Vadakkepatt, and A. Martini, *Tribol. Lett.* **44**, 367 (2011).
- [73] Y. Gao, *Journal of the Mechanics and Physics of Solids* **58**, 2023 (2010).
- [74] O. M. Braun and Y. S. Kivshar, *The Frenkel-Kontorova Model* (Springer Berlin Heidelberg, 2004).
- [75] H. Risken and H. D. Vollmer, *Zeitschrift für Phys. B Condens. Matter Quanta* **33**, 297 (1979).
- [76] H. Risken, *The Fokker-Planck Equation*, Springer Series in Synergetics, Vol. 18 (Springer Berlin Heidelberg, Berlin, Heidelberg, 1989).
- [77] M. H. Müser, M. Urbakh, and M. O. Robbins, in *Adv. Chem. Phys.*, Vol. 126 (John Wiley & Sons, Ltd, 2003) pp. 187–272.
- [78] X. Zhao, S. R. Phillpot, W. G. Sawyer, S. B. Sinnott, and S. S. Perry, *Physical Review Letters* **102**, 186102 (2009).
- [79] I. Barel, M. Urbakh, L. Jansen, and A. Schirmeisen, *Tribology Letters* **39**, 311 (2010).

- [80] S. Y. Krylov and J. W. M. Frenken, *physica status solidi (b)* **251**, 711 (2014).
- [81] I. Barel, M. Urbakh, L. Jansen, and A. Schirmeisen, *Phys. Rev. Lett.* **104**, 066104 (2010).
- [82] J. Krim and R. Chiarello, *Journal of Vacuum Science & Technology A: Vacuum, Surfaces, and Films* **9**, 2566 (1991).
- [83] E. D. Smith, M. O. Robbins, and M. Cieplak, *Physical Review B* **54**, 8252 (1996).
- [84] B. Persson, *Surface Science Reports* **33**, 83 (1999).
- [85] J. H. Kim, D. Fu, S. Kwon, K. Liu, J. Wu, and J. Y. Park, *Advanced Materials Interfaces* **3**, 1500388 (2016).
- [86] F. Galembeck, T. A. L. Burgo, L. B. S. Balestrin, R. F. Gouveia, C. A. Silva, and A. A. Galembeck, *RSC Advances* **4**, 64280 (2014).
- [87] H. Zou, Y. Zhang, L. Guo, P. Wang, X. He, G. Dai, H. Zheng, C. Chen, A. C. Wang, C. Xu, and Z. L. Wang, *Nat. Commun.* **10**, 1427 (2019).
- [88] V. M. Goldschmidt, *Die Naturwissenschaften* **14**, 477 (1926).
- [89] Y. Tokura and Y. Tomioka, *Journal of Magnetism and Magnetic Materials* **200**, 1 (1999).
- [90] E. Dagotto, *Nanoscale Phase Separation and Colossal Magnetoresistance*, Vol. 136 (Springer Berlin Heidelberg, 2003).
- [91] H. Jahn and E. Teller, *Proceedings of the Royal Society of London. Series A - Mathematical and Physical Sciences* **161**, 220 (1937).
- [92] N. N. Kovaleva, A. M. Oleś, A. M. Balbashov, A. Maljuk, D. N. Argyriou, G. Khaliullin, and B. Keimer, *Physical Review B* **81**, 235130 (2010).
- [93] R. Gross and A. Marx, *Festkörperphysik*, 2nd ed. (De Gruyter Oldenbourg, 2014) p. 1006.
- [94] C. Zener, *Physical Review* **82**, 403 (1951).
- [95] P. W. Anderson and H. Hasegawa, *Physical Review* **100**, 675 (1955).

- 
- [96] P. G. de Gennes, *Physical Review* **118**, 141 (1960).
- [97] A. Bhattacharya and S. J. May, *Annual Review of Materials Research* **44**, 65 (2014).
- [98] J. M. D. Coey, *Magnetism and Magnetic Materials* (Cambridge University Press, 2001).
- [99] S. Majumdar and S. V. Dijken, *Journal of Physics D: Applied Physics* **47**, 034010 (2014).
- [100] J. B. Goodenough, *Physical Review* **100**, 564 (1955).
- [101] J. B. Goodenough, *Journal of Physics and Chemistry of Solids* **6**, 287 (1958).
- [102] T. Akimoto, Y. Maruyama, Y. Moritomo, A. Nakamura, K. Hirota, K. Ohoyama, and M. Ohashi, *Physical Review B* **57**, R5594 (1998).
- [103] J. Hemberger, A. Krimmel, T. Kurz, H.-A. Krug von Nidda, V. Y. Ivanov, A. A. Mukhin, A. M. Balbashov, and A. Loidl, *Phys. Rev. B* **66**, 094410 (2002).
- [104] A. J. Millis, P. B. Littlewood, and B. I. Shraiman, *Physical Review Letters* **74**, 5144 (1995).
- [105] J. Hill, C. Nelson, M. v. Zimmermann, Y.-J. Kim, D. Gibbs, D. Casa, B. Keimer, Y. Murakami, C. Venkataraman, T. Gog, Y. Tomioka, Y. Tokura, V. Kiryukhin, T. Koo, and S.-W. Cheong, *Applied Physics A: Materials Science & Processing* **73**, 723 (2001).
- [106] C. Hartinger, F. Mayr, J. Deisenhofer, A. Loidl, and T. Kopp, *Physical Review B* **69**, 100403 (2004).
- [107] C. Hartinger, F. Mayr, A. Loidl, and T. Kopp, *Physical Review B* **73**, 024408 (2006).
- [108] R. Kilian and G. Khaliullin, *Physical Review B* **60**, 13458 (1999).
- [109] Y. Murakami, J. P. Hill, D. Gibbs, M. Blume, I. Koyama, M. Tanaka, H. Kawata, T. Arima, Y. Tokura, K. Hirota, and Y. Endoh, *Physical Review Letters* **81**, 582 (1998).
- [110] R. D. Shannon, *Acta Crystallographica Section A* **32**, 751 (1976).
- [111] Y. Syono, S. ito Akimoto, and K. Kohn, *Journal of the Physical Society of Japan* **26**, 993 (1969).
- [112] T. Sievert, *Structure-Property Relations of Epitaxial  $La_{0.6}Sr_{0.4}MnO_3$  Thin Films*, Master's thesis, Georg-August-Universität Göttingen (2021).

- [113] V. Moshnyaga, I. Khoroshun, A. Sidorenko, P. Petrenko, A. Weidinger, M. Zeitler, B. Rauschenbach, R. Tidecks, and K. Samwer, *Applied physics letters* **74**, 2842 (1999).
- [114] F. Döring, C. Eberl, S. Schlenkrich, F. Schlenkrich, S. Hoffmann, T. Liese, H. U. Krebs, S. Pisana, T. Santos, H. Schuhmann, M. Seibt, M. Mansurova, H. Ulrichs, V. Zbarsky, and M. Münzenberg, *Appl. Phys. A Mater. Sci. Process.* **119**, 11 (2015).
- [115] F. Döring, A. Major, C. Eberl, and H. U. Krebs, *Appl. Phys. A Mater. Sci. Process.* **122**, 1 (2016).
- [116] K. R. Mangipudi, C. Jooss, and C. A. Volkert, *Phys. Status Solidi* **213**, 824 (2016).
- [117] D. Meyer, V. Roddatis, J. P. Bange, S. Lopatin, M. Keunecke, D. Metternich, U. Roß, I. V. Maznichenko, S. Ostanin, I. Mertig, V. Radisch, R. Egoavil, I. Lazić, V. Moshnyaga, and H. Ulrichs, *pre-print* (2020), [10.48550/arXiv.2009.14532](https://arxiv.org/abs/10.48550/arXiv.2009.14532).
- [118] G. Binnig, C. F. Quate, and C. Gerber, *Physical Review Letters* **56**, 930 (1986).
- [119] O. Marti, J. Colchero, and J. Mlynek, *Nanotechnology* **1**, 141 (1990).
- [120] “PPP-LFMR – NANOSENSORS™,” (2022).
- [121] M. Nonnenmacher, *Journal of Vacuum Science & Technology B: Microelectronics and Nanometer Structures* **9**, 1358 (1991).
- [122] E. Gnecco, R. Bennewitz, T. Gyalog, and E. Meyer, *Journal of Physics Condensed Matter* **13** (2001), [10.1088/0953-8984/13/31/202](https://doi.org/10.1088/0953-8984/13/31/202).
- [123] B. N. J. Persson, *Sliding Friction*, NanoScience and Technology (Springer Berlin Heidelberg, Berlin, Heidelberg, 2000).
- [124] R. W. Carpick and M. Salmeron, *Chemical reviews* **97**, 1163 (1997).
- [125] J. Krim, *Advances in Physics* **61**, 155 (2012).
- [126] J. Y. Park, D. F. Ogletree, P. A. Thiel, and M. Salmeron, *Science* **313**, 186 (2006).
- [127] F. P. Bowden and D. Tabor, *The Friction and Lubrication of Solids, Volume 1* (New York: Oxford Univ., 2001) p. 374.
- [128] T. D. Jacobs and A. Martini, *Appl. Mech. Rev.* **69** (2017), [10.1115/1.4038130/367044](https://doi.org/10.1115/1.4038130/367044).

- 
- [129] M. A. Lantz, S. J. O'Shea, M. E. Welland, and K. L. Johnson, *Physical Review B* **55**, 10776 (1997).
- [130] M. Enachescu, R. J. V. D. Oetelaar, R. W. Carpick, D. F. Ogletree, C. F. Flipse, and M. Salmeron, *Tribology Letters* **7**, 73 (1999).
- [131] J. F. Archard, *Journal of Applied Physics* **24**, 981 (1953).
- [132] J. Gao, W. D. Luedtke, D. Gourdon, M. Ruths, J. N. Israelachvili, and U. Landman, *The Journal of Physical Chemistry B* **108**, 3410 (2004).
- [133] A. P. Merkle and L. D. Marks, *Tribology Letters* **26**, 73 (2007).
- [134] S. V. Buldyrev, J. Ferrante, and F. R. Zypman, *Physical Review E* **74**, 066110 (2006).
- [135] Q. Li, Y. Dong, D. Perez, A. Martini, and R. W. Carpick, *Phys. Rev. Lett.* **106**, 126101 (2011).
- [136] M. H. Müser, *Physical Review B* **84**, 125419 (2011).
- [137] C. Fusco and A. Fasolino, *Physical Review B* **71**, 045413 (2005).
- [138] E. Gnecco, R. Roth, and A. Baratoff, *Physical Review B - Condensed Matter and Materials Physics* **86**, 1 (2012).
- [139] R. Hu, S. Y. Krylov, and J. W. M. Frenken, *Tribology Letters* **68**, 8 (2020).
- [140] B. Persson, E. Tosatti, D. Fuhrmann, G. Witte, and C. Wöll, *Physical Review B* **59**, 11777 (1999).
- [141] H. Kramers, *Physica* **7**, 284 (1940).
- [142] D. Singh, P. Mittal, N. N. Gosvami, and V. Balakrishnan, *Advanced Engineering Materials* **21**, 1900616 (2019).
- [143] J. Y. Park, Y. Qi, D. F. Ogletree, P. A. Thiel, and M. Salmeron, *Phys. Rev. B* **76**, 064108 (2007).
- [144] M. Lessel, P. Loskill, F. Hausen, N. N. Gosvami, R. Bennewitz, and K. Jacobs, *Physical Review Letters* **111**, 035502 (2013).
- [145] J. Krim, *Frontiers in Mechanical Engineering* **5** (2019), 10.3389/fmech.2019.00022.

- [146] A. J. Millis, B. I. Shraiman, and R. Mueller, *Physical Review Letters* **77**, 175 (1996).
- [147] G. J. Snyder, M. R. Beasley, T. H. Geballe, R. Hiskes, and S. DiCarolis, *Applied Physics Letters* **69**, 4254 (1996).
- [148] C. Kwon, M. Robson, K.-C. Kim, J. Gu, S. Lofland, S. Bhagat, Z. Trajanovic, M. Rajeswari, T. Venkatesan, A. Kratz, R. Gomez, and R. Ramesh, *Journal of Magnetism and Magnetic Materials* **172**, 229 (1997).
- [149] J. Scholz, M. Risch, G. Wartner, C. Luderer, V. Roddatis, and C. Jooss, *Catalysts* **7**, 139 (2017).
- [150] S. Merten, V. Bruchmann-Bamberg, B. Damaschke, K. Samwer, and V. Moshnyaga, *Physical Review Materials* **3**, 060401 (2019).
- [151] M. Jungbauer, S. Hühn, R. Egoavil, H. Tan, J. Verbeeck, G. V. Tendeloo, and V. Moshnyaga, *Applied Physics Letters* **105**, 251603 (2014).
- [152] Y. Kamimura, K. Edagawa, and S. Takeuchi, *Acta Materialia* **61**, 294 (2013).
- [153] V. Rajendran, S. M. Kumaran, V. Sivasubramanian, T. Jayakumar, and B. Raj, *Physica Status Solidi (A) Applied Research* **195**, 350 (2003).
- [154] A. Schirmeisen, L. Jansen, H. Hölscher, and H. Fuchs, *Appl. Phys. Lett.* **88**, 123108 (2006).
- [155] E. Riedo and H. Brune, *Applied Physics Letters* **83**, 1986 (2003).
- [156] Y. Mo, K. T. Turner, and I. Szlufarska, *Nature* **457**, 1116 (2009).
- [157] D. Perez, Y. Dong, A. Martini, and A. F. Voter, *Phys. Rev. B* **81**, 245415 (2010).
- [158] A. Sawa, *Materials Today* **11**, 28 (2008).
- [159] S. R. S. de Mello, M. E. H. M. da Costa, C. M. Menezes, C. D. Boeira, F. L. F. Jr, F. Alvarez, and C. A. Figueroa, *Scientific Reports* **7**, 3242 (2017).
- [160] R. J. Cannara, M. J. Brukman, K. Cimatú, A. V. Sumant, S. Baldelli, and R. W. Carpick, *Science* **318**, 780 (2007).
- [161] Y. Mo, M. H. Müser, and I. Szlufarska, *Physical Review B - Condensed Matter and Materials Physics* **80**, 1 (2009).

- [162] O. Braun, *Surf. Sci.* **213**, 336 (1989).
- [163] M. N. Iliev and M. V. Abrashev, *Journal of Raman Spectroscopy* **32**, 805 (2001).
- [164] J. L. Cohn, J. J. Neumeier, C. P. Popoviciu, K. J. McClellan, and T. Leventouri, *Phys. Rev. B* **56**, R8495 (1997).
- [165] P. Björnsson, M. Rübhausen, J. Bäckström, M. Käll, S. Eriksson, J. Eriksen, and L. Börjesson, *Physical Review B* **61**, 1193 (2000).
- [166] G. Po, Y. Cui, D. Rivera, D. Cereceda, T. D. Swinburne, J. Marian, and N. Ghoniem, *Acta Materialia* **119**, 123 (2016).
- [167] J. Lothe, *Journal of Applied Physics* **33**, 2116 (1962).
- [168] J. P. Hirth, J. Lothe, and T. Mura, *Journal of Applied Mechanics* **50**, 476 (1983).
- [169] A. A. Balandin, *MRS Bulletin* **39**, 817 (2014).
- [170] J. E. Sader, J. W. M. Chon, and P. Mulvaney, *Review of Scientific Instruments* **70**, 3967 (1999).
- [171] B. Bhushan, *Handbook of Micro/Nano Tribology*, 2nd ed. (CRC Press, 2020) p. 880.
- [172] C. K. Buenviaje, S.-R. Ge, M. H. Rafailovich, and R. M. Overney, *MRS Proceedings* **522**, 187 (1998).
- [173] K. Deng and W. H. Ko, *Journal of Micromechanics and Microengineering* **2**, 14 (1992).
- [174] O. Gordon, F. Junqueira, and P. Moriarty, "nOmicron: Python Control of Scienta Omicron Matrix," (2019).
- [175] Y. Dong, *J. Phys. D: Appl. Phys.* **47**, 055305 (2014).
- [176] C. Lee, Q. Li, W. Kalb, X.-Z. Liu, H. Berger, R. W. Carpick, and J. Hone, *Science* (80-. ). **328**, 76 (2010).
- [177] T. Filleter, J. L. McChesney, A. Bostwick, E. Rotenberg, K. V. Emtsev, T. Seyller, K. Horn, and R. Bennewitz, *Physical Review Letters* **102**, 086102 (2009).
- [178] M. Lee, R. L. Vink, C. A. Volkert, and M. Krüger, *Phys. Rev. B* **104**, 174309 (2021).
- [179] Q. Li, C. Lee, R. W. Carpick, and J. Hone, *Phys. status solidi* **247**, 2909 (2010).

- [180] S. Kwon, J.-H. Ko, K.-J. Jeon, Y.-H. Kim, and J. Y. Park, *Nano Lett.* **12**, 6043 (2012).
- [181] X. Zeng, Y. Peng, L. Liu, H. Lang, and X. Cao, *Nanoscale* **10**, 1855 (2018).
- [182] A. Smolyanitsky, J. P. Killgore, and V. K. Tewary, *Phys. Rev. B* **85**, 035412 (2012).
- [183] L. Xu, T.-B. Ma, Y.-Z. Hu, and H. Wang, *Nanotechnology* **22**, 285708 (2011).
- [184] S. Kajita, H. Washizu, and T. Ohmori, *EPL (Europhysics Letters)* **87**, 66002 (2009).
- [185] D. Andersson and A. S. de Wijn, *Nat. Commun.* **11**, 420 (2020).
- [186] Z. Ye, C. Tang, Y. Dong, and A. Martini, *J. Appl. Phys.* **112**, 116102 (2012).
- [187] M. Keunecke, F. Lyzwa, D. Schwarzbach, V. Roddatis, N. Gauquelin, K. Müller-Caspary, J. Verbeeck, S. J. Callori, F. Klose, M. Jungbauer, and V. Moshnyaga, *Adv. Funct. Mater.* **30**, 1808270 (2020).
- [188] H. Kiessig, *Annalen der Physik* **402**, 715 (1931).
- [189] S. Macke, A. Radi, J. E. Hamann-Borrero, A. Verna, M. Bluschke, S. Brück, E. Goering, R. Sutarto, F. He, G. Cristiani, M. Wu, E. Benckiser, H.-U. Habermeier, G. Logvenov, N. Gauquelin, G. A. Botton, A. P. Kajdos, S. Stemmer, G. A. Sawatzky, M. W. Haverkort, B. Keimer, and V. Hinkov, *Advanced Materials* **26**, 6554 (2014).
- [190] B. Bhushan, *Nanotribology and Nanomechanics I*, Vol. 3 (Springer Berlin Heidelberg, 2011) p. 633.
- [191] J. E. Sader, I. Larson, P. Mulvaney, and L. R. White, *Review of Scientific Instruments* **66**, 3789 (1998).
- [192] J. E. Sader, R. Borgani, C. T. Gibson, D. B. Haviland, M. J. Higgins, J. I. Kilpatrick, J. Lu, P. Mulvaney, C. J. Shearer, A. D. Slattery, P.-A. Thorén, J. Tran, H. Zhang, H. Zhang, and T. Zheng, *Review of Scientific Instruments* **87**, 093711 (2016).
- [193] B. Cappella and G. Dietler, *Surface Science Reports* **34**, 1 (1999).
- [194] D. R. Baer, M. H. Engelhard, G. E. Johnson, J. Laskin, J. Lai, K. Mueller, P. Munusamy, S. Thevuthasan, H. Wang, N. Washton, A. Elder, B. L. Baisch, A. Karakoti, S. V. N. T. Kuchibhatla, and D. Moon, *J. Vac. Sci. Technol. A Vacuum, Surfaces, Film.* **31**, 050820 (2013).

- [195] P. Aich, C. Meneghini, L. Tortora, V. Siruguri, S. D. Kaushik, D. Fu, and S. Ray, *J. Mater. Chem. C* **7**, 3560 (2019).
- [196] R. P. Vasquez, *J. Electron Spectros. Relat. Phenomena* **56**, 217 (1991).
- [197] J. F. Moulder, *Handbook of X-ray Photoelectron Spectroscopy*, edited by J. Chastain (Perkin-Elmer Corporation, Minnesota, 1992) p. 242.
- [198] J. Wang, Y. Shin, N. Gauquelin, Y. Yang, C. Lee, D. Jannis, J. Verbeeck, J. M. Rondinelli, and S. J. May, *J. Phys. Condens. Matter* **31** (2019), 10.1088/1361-648X/ab2414.
- [199] K. N. Mikhalev, S. A. Lekomtsev, A. P. Gerashchenko, A. Y. Yakubovskii, and A. R. Kaul', *J. Exp. Theor. Phys. Lett.* **77**, 401 (2003).
- [200] K. Xu, X.-Z. Lu, and H. Xiang, *npj Quantum Mater.* **2**, 1 (2017).
- [201] B. Bhushan, H. Fuchs, and S. Hosaka, *Applied Scanning Probe Methods*, NanoScience and Technology (Springer Berlin Heidelberg, Berlin, Heidelberg, 2004) pp. 9–25.
- [202] K. Persson, "Materials Data on LaMnO<sub>3</sub> (SG:221) by Materials Project," (2014).
- [203] K. Persson, "Materials Data on SrMnO<sub>3</sub> (SG:221) by Materials Project," (2017).
- [204] W. Lu, Y. Xie, G. Chen, and F. Tang, *Phys. B Condens. Matter* **406**, 1289 (2011).
- [205] F. P. Bowden, D. Tabor, and E. H. Freitag, *Reibung und Schmierung fester Körper* (Springer Berlin Heidelberg, 1959) p. 440.
- [206] G. He, M. H. Müser, and M. O. Robbins, *Science* **284**, 1650 (1999).
- [207] S. Hashimoto, *ECS Proc. Vol.* **1999-19**, 379 (1999).
- [208] C. Zener, *Phys. Rev.* **52**, 230 (1937).
- [209] C. Zener, *Phys. Rev.* **53**, 90 (1938).
- [210] N. A. Weber, *Temperaturabhängige Reibungsmessungen an LPCMO*, Master's thesis, Georg-August-Universität Göttingen (2019).
- [211] L. Chen, Z. Wang, G. Wang, H. Guo, M. Saghayezhian, Z. Liao, Y. Zhu, E. W. Plummer, and J. Zhang, *Phys. Rev. Mater.* **3**, 044407 (2019), arXiv:1904.05246 .

- [212] A. J. Millis, P. B. Littlewood, and B. I. Shraiman, *Physical Review Letters* **74**, 5144 (1995).
- [213] P. Lin, S. H. Chun, M. B. Salamon, Y. Tomioka, and Y. Tokura, *J. Appl. Phys.* **87**, 5825 (2000).
- [214] A. D. Souza and M. Daivajna, *J. Supercond. Nov. Magn.* **33**, 1781 (2020).
- [215] S. Kwon, J.-H. Ko, K.-J. Jeon, Y.-H. Kim, and J. Y. Park, *Nano Letters* **12**, 6043 (2012).
- [216] Q. Li, X.-Z. Liu, S.-P. Kim, V. B. Shenoy, P. E. Sheehan, J. T. Robinson, and R. W. Carpick, *Nano Letters* **14**, 5212 (2014).
- [217] L. M. Leidens, M. E. H. Maia da Costa, N. S. Figueroa, R. A. Barbieri, F. Alvarez, A. F. Michels, and C. A. Figueroa, *Physical Chemistry Chemical Physics* **23**, 2873 (2021).
- [218] M. Guggisberg, M. Bammerlin, C. Loppacher, O. Pfeiffer, A. Abdurixit, V. Barwich, R. Bennewitz, A. Baratoff, E. Meyer, and H.-J. Güntherodt, *Phys. Rev. B* **61**, 11151 (2000).
- [219] A. Schirmeisen, H. Hölscher, B. Anczykowski, D. Weiner, M. M. Schäfer, and H. Fuchs, *Nanotechnology* **16**, S13 (2005).
- [220] M. Björck and G. Andersson, *J. Appl. Crystallogr.* **40**, 1174 (2007).
- [221] S. Tougaard, "QUASES-IMFP-TPP2M - QUASES Ver.3.0," (2016).
- [222] S. Tanuma, C. J. Powell, and D. R. Penn, *Surf. Interface Anal.* **21**, 165 (1994).
- [223] Y. S. Hou, H. J. Xiang, and X. G. Gong, *Phys. Rev. B* **89**, 064415 (2014).
- [224] A. Bhattacharya, S. J. May, S. G. Te Velthuis, M. Warusawithana, X. Zhai, B. Jiang, J. M. Zuo, M. R. Fitzsimmons, S. D. Bader, and J. N. Eckstein, *Phys. Rev. Lett.* **100**, 257203 (2008).

# Acknowledgements

First and foremost, I would like to express my gratitude to my supervisor, Cynthia A. Volkert, for her guidance, the countless encouragements, and for many valuable discussions and the advice over the past three and a half years.

I would like to thank Matthias Krüger, not only agreeing to become the second examiner, but also for the fruitful discussions during our weekly A01-meetings, and his support, especially in the final phase of my thesis.

I thank Martin Wenderoth and Friedrich Güthoff for being part of the thesis committee and being available to discuss physical and organizational questions. Moreover, I am grateful for the many technical discussions on AFM-related topics I had with Friedrich. I thank him for his time and interest in automating the vacuum system with Python scripts. Without his help and persistence in realigning the fiber optics, this work would not have been possible.

Furthermore, I would like to thank all the remaining members of the examination board.

Many thanks to all the not yet mentioned members of project A01: Richard Vink, Kim Lambert and especially Miru Lee for the weekly meetings, and the fruitful collaboration.

Tim and Leonard are thanked for the preparation and characterization of the thin films studied.

I thank my fellow Nanos on the third floor for the wonderful working environment and help with various x-ray and SEM measurements: A special thanks goes to my office mate Florian, with whom I not only mastered the doctoral thesis, but also various sport boat licenses.

I am furthermore grateful for all those who have accompanied me during my university career and who joined me in several sporting challenges. Here a special thanks to Lotta, John and Felix for all the encouragement and support.

Finally, I would like to express my gratitude to parents Erika and Norbert, my siblings Juri and Frieda and especially my girlfriend Meike for their unconditional support!

